Waveguide Antenna Feed for the Square Kilometre Array

by

Karla Schoeman

Thesis presented in partial fulfilment of the requirements for the degree of
Master of Science in Engineering
at Stellenbosch University

Supervisors:

Prof P. Meyer Dr D.I.L De Villiers
Department Electrical and Electronic Engineering

March 2011

Declaration

By submitting this thesis electronically, I declare that the entirety of the work contained therein is my own, original work, that I am the sole author thereof (save to the extent explicitly otherwise stated), that reproduction and publication thereof by Stellenbosch University will not infringe any third party rights and that I have not previously in its entirety or in part submitted it for obtaining any qualification.

March 2011

Abstract

The aim of this thesis is to investigate the suitability of TEM (Transverse Electromagnetic) horn antennas for use as feed structures for the Square Kilometre Array (SKA) radio telescope, in particular with regard to the roundness of the radiation pattern. A literature study shows that existing TEM horn designs do not yield a round radiation pattern over a wide bandwidth and that an alternative is required. The Method of Moments (MoM) is a computational electromagnetic (CEM) technique typically used in the analysis of TEM horn antennas. An in-house MoM solver is successfully developed to analyse such antennas and is able to calculate the current density on the surface of a conductor, as well as the farfield patterns of an antenna. A modification to an exponential TEM horn antenna is proposed and simulations show the modification is successful in yielding a round radiation pattern over a wide bandwidth. The modified exponential TEM horn has a convex triangular arc at the end of each antenna plate and is constructed for measurement. Due to limited construction capabilities, the measurements deviate slightly from the simulated results but still indicate the potential of the structure to yield a round radiation pattern over a wide bandwidth.

Opsomming

Die doel van hierdie tesis is om die geskiktheid van transverse elektromagnetiese (TEM) horing antennas te ondersoek vir die gebruik as voerstrukture vir die Square Kilometre Array (SKA)-radioteleskoop, veral met betrekking tot die rondheid van die stralingspatroon. 'n Literatuurstudie toon dat bestaande TEM horing ontwerpe nie 'n ronde stralingspatroon oor 'n wye bandwydte lewer nie, en dat 'n alternatief nodig is. Die metode van momente is 'n rekenbare elektromagnetiese tegniek wat tipies gebruik word in die ontleding van TEM horing antennas. 'n In-huis metode van momente ontleder is suksesvol ontwikkel om sulke antennas te analiseer en is in staat om die stroomdigtheid op die oppervlak van 'n geleier, sowel as die vêrveld patrone van die antenna te bereken. 'n Wysiging van 'n eksponensiële TEM horing antenna word voorgestel en simulasies toon dat die veranderings suksesvol is om 'n ronde stralingspatroon oor 'n wye bandwydte te skep. Die verander eksponensiële TEM horing het 'n konvekse driehoekige boog aan die einde van elke antenna plaat en is gebou vir meting. Weens beperkte konstruksie vermoëns, toon die metings 'n afwyking van die gesimuleerde resultate, maar dui nogsteeds die potensiaal aan van die struktuur om 'n ronde stralingspatroon te lewer oor 'n wye bandwydte.

Acknowledgements

My sincerest gratitude to:

- Prof. P. Meyer for his support and guidance as study leader. I appreciate all the encouragement you gave me over the years.
- Dr. Dirk de Villiers for his patience, insight and knowledge of antennas.
- Prof. K. D. Palmer for his insight and interest. Thank you for always being willing to help.
- Wynand van Eeden and Wessel Croukamp for construction of the antenna.
- Martin Siebers for assisting with the antenna measurements.
- My father Jan Schoeman and brother Heinrich for their love, support and encouragement and for always being there for me.
- Gerrit Avenant for all his love, support and patience.
- Males Tomlinson and Lorita Christelis for their friendship and endless encouragement.
- Computer Simulation Technology (CST) for the use of their software for simulation purposes.
- EMSS for the use of their simulation software, FEKO.
- The SKA (South Africa) for their financial assistance during my Masters.

Contents

List of Figures

List of Tables

Chapter 1

Introduction

The Square Kilometre Array (SKA) is a €1.5 Billion international radio astronomy project which is focused on developing the world's largest radio telescope. The telescope will be able to receive cosmic radiation from the 'Dark Ages' which is the period 300 000 million to 1 billion years after the Big Bang [1]. This will provide astronomers with more information about the evolution of the universe, black holes, dark matter and many other astronomical events.

South Africa and Australia are competing for the bid to host the SKA telescope and a final decision about its location should be made by 2012 [1]. South Africa is in the process of developing technology for the SKA and we have demonstrated our excellent scientific and engineering skills by designing and commencing with the construction of the MeerKAT radio telescope, which will be a path finder for the SKA [1]. So far, 7 of the MeerKAT dishes have been built in the Karoo and are called the KAT-7. They have already produced some images from radio waves [1].

The most important factors which will decide the location of the SKA are:

- The radio quietness of the site - it needs to be free from the interference of radio signals such as from televisions, mobile phones and towers, radios and most other electrical or electronic equipment [1].

- The scientific and engineering capacity of the country with an ideal site [1].

In terms of a quiet location free from radio waves, the site in the Karoo chosen in South Africa is perfect. The sparse population of the area and the mountains blocking external radio waves make it an ideal location for the SKA. South Africa has demonstrated its excellent scientific and engineering capacity with the development of the KAT-7 and MeerKAT.

Further scientific research is continuously being conducted to develop improved technology that will meet SKA criteria. This project is focused on the development of a wideband antenna feed for the SKA and investigates the suitability of TEM horn antennas for this purpose. The functional specifications required for an SKA feed antenna are listed in Table 1.1.

Waveguide Antenna Feed	
Operating frequency range	1-10 [GHz]
Bandwidth	10 [GHz]
Angular width of radiation pattern in H-plane	60 [^{o}]
Angular width of radiation pattern in E-plane	60 [^{o}]
Radiation pattern	Round
Maximum directivity	10 [dBi] minimum
Side lobe level	-13 [dB] and below
Polarisation	Dual

Table 1.1: SKA feed antenna specifications

The feed antenna is positioned on the radio telescope dish as shown in Figure 1.1. To capture all signal information, radio astronomy requires the feed to have vertical and horizontal polarization [2]. The radiation pattern of the feed must be perfectly circular (as indicated by the red pattern in Figure 1.1 (b)) to avoid signal information loss. If the pattern is slightly elliptical (blue pattern), information is lost and radiated onto the ground [2]. This also causes noise generation which will make it difficult to identify the incoming signals.

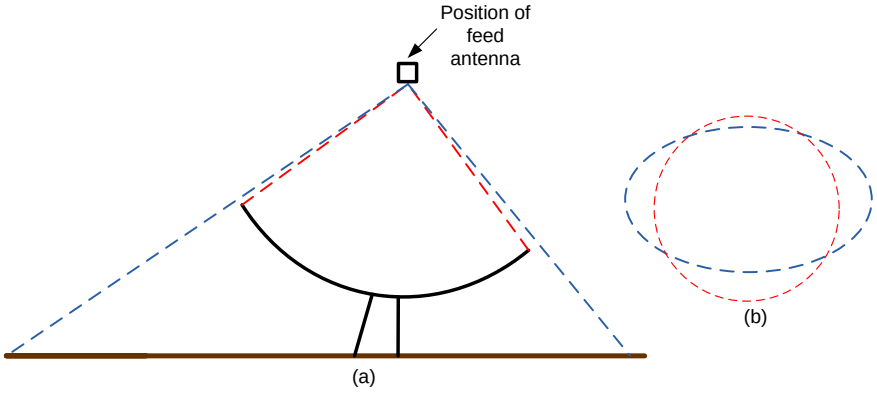

Figure 1.1: Radio telescope and feed antenna set up. Adapted from [2]

At a frequency f_o, the antenna must perfectly illuminate the **round** telescope dish, so that there is no spill over of energy which adds noise to the system and to ensure that the entire surface area of the dish is utilised efficiently. For this to occur the radiation pattern must be round (as defined below) and the angular width or half power beam width (HPBW) must be exactly 60°(depending on the dish specification) in both the H- and E-planes.

The aim of this thesis is to achieve a round radiation pattern over a wide bandwidth for single polarisation. When referring to the radiation pattern, the farfield directivity is implied. The definition of a round radiation pattern used for the purposes of this project, as well as relevant parameters

used to determine if a pattern is round are given below:

- The radiation pattern (directivity) is considered round if it is seen to be so looking directly at it from the front towards the antenna's aperture.
- If the E- and H-plane directivity patterns are equal, it is a good indication that the radiation pattern is round when viewed from the front.
- For the purposes of this investigation, the E- and H-plane patterns are considered equal if the difference between them is less than or equal to 1 [dB].
- The radiation pattern is considered round if the E- and H-plane patterns are equal (within 1 [dB]) for at least -3 [dB] below the main beam maximum (for the HPBW), but should ideally be equal for up to -10 [dB] below the main beam maximum.
- The angular range over which the E- and H-plane radiation patterns are equal (within 1 [dB]) is the range over which the radiation pattern is considered round. To avoid confusing it with the HPBW, it is usually referred to as the one-sided range: $-\theta_{1dB}$ [^{o}] $\leq \theta \leq 0$ [^{o}] or $-\theta_{1dB}$.
- The *Equal Level* (EL) is defined as the number of [dB] below the main beam maximum (using the E-plane directivity pattern as reference) for which the E- and H-plane patterns are within 1 [dB] of each other.

Although TEM horns offer only single-polarisation, this must be achieved successfully before considering dual-polarisation. This project is focused on achieving the SKA specifications for single polarisation in terms of a round radiation pattern. If it is required, further study can be conducted based on the results achieved in this thesis to determine if the antenna can be modified to achieve dual-polarisation.

A detailed project description is provided in the next chapter.

Chapter 2

Project Description

The aim of this project is to investigate the suitability of TEM horn antennas for use as an SKA feed, specifically with regard to the roundness of the radiation pattern. The project is also focused on achieving an understanding of the Method of Moments, which is a CEM (Computational Electromagnetic) technique typically used in the analysis of such antennas.

The investigation commences with the analysis of some pre-existing TEM horn antenna designs after which an in-house MoM solver is develop to calculate the farfield patterns of TEM horns. The final stage of the project discusses a proposed modification to an exponential TEM horn, which is successful in yielding a round radiation pattern over a wide bandwidth. The rest of this chapter provides a brief description of each stage of the project.

2.1 TEM Horn Antennas

Chapter 3 investigates the performance of two previously existing types of TEM horn antennas. The first antenna is a standard linearly tapered TEM horn shown in Figure 3.4, whereas the second is an elliptically tapered TEM horn with a Hecken impedance taper shown in Figure 3.15. The linear horn is chosen for analysis since it is the most basic type of TEM horn antenna. The elliptical/Hecken horn is presented in [3] and is a relatively new type of TEM horn, designed to have an optimum impedance taper to yield very low reflections over a very wide bandwidth. It is decided to take a closer look at the radiation characteristics of such an optimally tapered design and compare it to the linear TEM horn in terms of the criteria for an SKA feed antenna.

Linear TEM Horn A linearly tapered TEM horn antenna such as the one in Figure 3.1 is the most basic type of TEM horn. The electric farfield radiation characteristics of the antenna are investigated in Section 3.1 for various values of the plate separation angle β. The angular width α is adjusted as β varies to keep the characteristic impedance of the antenna constant when determining the influence of the plate separation angle on the E- and H-plane directivity patterns.

It is found that the E- and H- plane patterns behave in an opposite manner in terms of producing a split main beam as β is increased or decreased. The correlation between the E and H-plane patterns is not good and there is a lot of break up of the main beam, in either the E- or H-plane or both.

The frequency behavior of a linear TEM horn is also investigated and compared to that of an elliptical TEM horn with a Hecken impedance taper shown in Figure 3.15. For the frequency analysis the total length, as well as the aperture height of the linear horn are adjusted to be the same as the elliptical horn. The E- and H-plane patterns are calculated at 1, 4 and 7 [GHz] for the frequency analysis. The main lobes exhibit break up at all the sample frequencies and the correlation between the E- and H-planes is poor.

Overall, the antenna does not perform well according to SKA specifications and it would be difficult to achieve a round radiation patterns using this antenna.

Elliptical TEM Horn The radiation characteristics of an elliptical TEM horn with a Hecken impedance profile [3] are discussed in Section 3.2. The E- and H-plane patterns are calculated at 1, 4 and 7 [GHz]. As with the linear horn, the main beams exhibit break up, either in the E- or H-plane or in both. The correlation between the E- and H-plane patterns is poor and the antenna does not yield a round radiation pattern. In terms of roundness, it does not perform better than the linear TEM horn and is considerably more difficult to construct.

2.2 Method of Moments

The Method of Moments (MoM) is a very efficient numerical technique for the analysis of TEM horns. Chapter 4 serves as an introduction to the Method of Moments (MoM) by discussing and implementing the principle for the case of thin wires. The MoM is used to solve for the current density in the Electric Field Integral Equation (EFIE) defined by Equation 4.7. The thin wire case serves as a stepping stone for the development of an in-house MoM solver in Chapter 5, which makes use of the triangular patch MoM to calculate the surface current density on the surfaces of conductors such as TEM horns antennas.

Pocklington's Integral Equation Section 4.2 discusses Pocklington's Integral Equation, which simplifies the calculations required to solve the EFIE using approximations that are applicable to thin wires ($r << \lambda$, where r is the wire radius and λ is the wavelength). The equation is derived by replacing the z-directed surface current flowing on a thin wire with radius a (such as in Figure 4.1 (a)), by a z-directed line current which lies on the $z - axis$. However, to avoid integrating singularities in the Green's function, the boundary condition that the tangential electric field is equal to zero on the surface of a conductor is still enforced at $r = a$. The details of the derivation

are provided in Section 4.2. The MoM solves Pocklington's Integral Equation for the current density distribution on a thin wire.

MoM - Approximating the Current The MoM makes use of N or $N-1$ basis functions (depending on the type of basis function) to approximate the current density on a thin wire which has been broken into N segments. The total current density distribution anywhere on the wire is approximated as the weighted sum of basis functions as shown by Equation 5.3. Each basis function f_n is associated with a constant current coefficient or weighting coefficient I_n for which the MoM solves.

MoM code is developed in MATLAB to calculate the current density distribution on a thin wire dipole antenna for each of the following types of basis functions:

- Constant/Pulse
- Triangular
- Sinusoidal

The results achieved with the various types of basis functions are compared to one another as well as to the results produced with the simulation software, FEKO. The influence of the number of segments/basis functions is also discussed.

Results The results of the in-house MoM code for thin wires compare well to those calculated by FEKO. Sinusoidal basis functions yielded the most accurate current density distribution. In general, the larger the number of segments (i.e. basis functions), the more accurate the results.

2.3 Method of Moments Formulation for Tapered Waveguides

Chapter 5 discusses the development of an in-house MoM solver which makes use of the triangular patch MoM [4] to calculate the current density on the surface of a conductor. The surface current density is then used to calculate the electric farfield pattern of the antenna. A mesher is also developed to triangulate surfaces as required by the MoM solver. The in-house code is developed in MATLAB and makes use of symmetry, specific to our application, to simplify the number of calculations required.

Triangular Patch Method of Moments Section 5.1.1 discusses the triangular patch MoM. The method introduced by Rao et al [4] requires that the surface of a conductor be discretized into triangles in terms of appropriate faces and vertices and non-boundary edges. The surface current density is approximated in Equation 5.3 as the weighted sum of Rao-Wilton-Glisson (RWG) basis

functions. Each basis function $\mathbf{f}_n$ is defined by Equation 5.37 and is associated with a non-boundary edge n and current density coefficient I_n. The basis function is zero everywhere on the triangulated surface, except in the two triangles that share edge n. The Method of Moments is used to solve for the weighting coefficients I_n in Equation 5.3.

Numerical Integration Numerical integration is used to simplify the integral calculations required to solve the EFIE. Since the RWG basis functions are defined in terms of the vertices and points inside a triangular domain, it is convenient to use simplex coordinates to define the sample points for numerical integration.

- Simplex Coordinates are also known as Area Coordinates. Using simplex coordinates to define the numerical integration sample points allows the definition of 1 set of sample coordinates, which is the same for all triangles. This will make the points symmetric in all triangles and avoids variations caused by element vertex reordering [5]. The sample points are easily converted back to Cartesian coordinates as discussed in Section 5.1.2.

- Quadrature integration is the numerical technique used to approximate the integrals required to solve the EFIE. The method approximates an integral as a summation of integrand samples which are multiplied by a set of weighting coefficients [5]. Thee sample points are chosen in each triangle and defined in simplex coordinates as discussed in [6]. The sample points (source points) do not coincide with the centroid of the triangle (observation point), thereby avoiding the singularities that occur when the source triangle is equal to the observation triangle.

Simplex coordinates and quadrature integration are discussed in detail in Section 5.1.2.

Symmetry The electrical symmetry of TEM horn antennas is used to reduce the number of calculations required to solve for the unknown current density coefficients on the top and bottom plates of such antennas. As discussed in Section 5.1.3, the current density coefficients on the bottom plate of a TEM horn can be described in terms of the current density coefficients on the top plate using symmetry. This halves the number of unknowns and reduces the number of calculations which fall inside the nested for-loop used by the in-house solver to solve the matrix EFIE. If there are a total of $K = 2N$ non-boundary edges for the top and bottom plates together, there are $K^2 = 4N^2$ repetitions of the calculations inside the for-loops to solve for the K current coefficients. Using electrical symmetry will reduce the repetition of the calculations to N^2 and significantly reduces simulation time of the in-house solver.

Farfield Approximations The electric farfield can be calculated either from the near-fields at the aperture of an antenna, or directly from the surface current densities and the EFIE by using

approximations applicable to the farfield or Fraunhofer region [7]. The second method is used in the in-house solver and the analytical details are discussed in Section 5.1.4.

Mesher A mesher is developed to triangulate the surfaces of typical TEM horn geometries in terms of appropriate non-boundary edges, faces and vertices. The data from the mesher is stored and used in the in-house MoM solver as required by the triangular patch MoM. Section 5.2.1 discusses development of the mesher and shows examples of surfaces that are successfully triangulated using the code.

Success of In-house MoM Code The successful implementation of an in-house MoM solver is illustrated in Section 5.3 using various examples. The current density and/or farfield of some basic, as well as more complex antennas is calculated using the in-house solver and compared to the results produced by FEKO. The following antennas are analysed to test the code:

- Single Flat Plate - compare the current densities
- Parallel Plates - compare current densities and 3D electric farfield patterns
- Ribbon Horn - compare 3D and 2D ($\phi = 0, 45, 90\ [^o]$) electric farfield patterns
- Linear TEM Horn - compare 3D and 2D ($\phi = 0, 45, 90\ [^o]$) electric farfield

2.4 Modified Exponentially Tapered TEM Horns

Chapter 6 discusses the achievement of a round radiation pattern over a wide bandwidth with a proposed modification to an exponential TEM horn. It is proposed to modify the width profile of the horns close to the aperture so that the H-plane directivity will diverge less from the E-plane directivity as seen with the linear TEM horn.

An article [8] by Mallahzadeh *et al* discusses the effect of a **concave** arc at the mouth of an exponential TEM horn, on the E- and H-plane directivity. Their focus is on the break-up of the main lobes of the E- and H-plane directivity at higher frequencies. However, the results are only stated for one antenna with fixed dimensions and it is shown in Chapter 6 that the main beams of the standard exponential TEM horn do not exhibit significant break up either.

In Chapter 6 it is proposed that the influence of **convex** arcs at the mouth of the exponential TEM horns is also investigated and it is found that this type of arc offers considerable potential to achieve a round radiation pattern.

Standard Exponential Horn The analytical procedure used to design the standard exponential TEM horn is discussed in Section 6.1, and forms the basis for the design of the modified horns discussed in Chapter 6.

Concave vs Convex Parabolic Arc Section 6.2.1 explains how the standard exponential horn is modified to obtain an exponential horn with a **concave** parabolic arc as well as an exponential horn with a **convex** parabolic arc. The E- and H-plane characteristics of the two modified horns (with an arc depth of $L/20$ as shown in Figure 6.4) are compared to those of the standard exponential horn at frequencies of 1, 4 and 7 [GHz]. It is concluded that the horn with the **convex** arc shows the most potential to achieve a round radiation pattern, especially at the lower frequencies. Therefore, the influence of arc depth on the roundness of the radiation pattern is further investigated for the antenna with the convex parabolic arc, with the expectation that the improvement in the roundness seen in Figure 6.7 (c) can be extended to the higher frequencies if the arc depth is increased.

Influence of Arc Depth on Roundness of Radiation Pattern The influence of arc depth on the roundness of the radiation pattern is investigated for two types of **convex** arcs:

- **Convex Parabolic Arc** - Section 6.2.2 illustrates that the arc depth can be optimised to decrease the difference between the E- and H-plane patterns below 1 [dB] over a wider angular range (yielding lower **Equal Levels**) at more than one frequency in the bandwidth. It is found that the smaller arcs offer an improvement in the roundness mostly at the lower frequencies, whereas the larger arcs offer an improvement at the higher frequencies or both. The antenna with an arc depth of $L/6$ offered the best overall improvement as discussed in Section 6.2.2.

- **Convex Triangular Arc** - The investigation of the influence of the arc depth is repeated for an exponential TEM horn with a convex triangular arc. The improvements seen with the triangular arc are very similar to those seen with the parabolic arc in terms of the frequency behaviour with regard to lower Equal levels and increased 1 [dB] angular range. As before, an arc depth of $L/6$ offers the best overall improvement at the largest number of frequencies in the bandwidth. It also offers an even greater improvement than the antenna with the $L/6$ convex parabolic arc and is therefore chosen for construction and measurements.

Wideband Feed A wideband feed which uses a standard 50 [Ω] SMA connector is required as an excitation source for the constructed antenna. The reflections of the feed are considered sufficiently low, so as not to decrease the performance of the antenna, if $|s_{11}| \leq -15$ [dB] over the bandwidth. Section 6.3 explains why a simple parallel plate configuration with a flat short circuit end and SMA connector mounted as shown in Figure 6.18 will not yield a wideband feed.

An alternate wideband feed configuration is shown in Figure 6.19 and is taken from [8]. The dimensions of the feed are optimised as discussed in Section 6.3 so as to achieve a value of $|s_{11}| \leq -15$ [dB] from 0.8-6 [GHz].

Final Antenna and Feed Simulation Results Section 6.3.1 discusses the simulation results of the final system; the exponential TEM horn with an $L/6$ triangular arc together with its wideband feed as shown in Figure 6.28. A coaxial waveguide port is used to excite the SMA connector in CST. Figure 6.29 shows that $|s_{11}|$ is below -10 [dB] from 1-6 [GHz] and below -15 [dB] from about 1.5-6 [GHz]. A value of -10 [dB] is deemed sufficient for the purposes of this project and the bandwidth is taken to be from 1-6 [GHz].

The E- and H-plane directivity of the antenna is plotted at 1 [GHz] intervals from 1-6 [GHz]. The **Equal Levels** of the antenna are well below the -3 [dB] half-power value from 1-4 [GHz], with a notable -10.4 [dB] achieved at 3 [GHz]. Although the patten is not considered round at 5 and 6 [GHz], the E- and H-plane patterns are still relatively similar. From the results in Chapter 6 it is concluded that modifying an exponential TEM horn to have a convex triangular arc yields a round radiation pattern over a wide bandwidth.

Construction and Measurement The final antenna system consists of the exponential TEM horn with an $L/6$ triangular arc and its wideband feed. The E- and H-plane farfield patterns, as well as s_{11} are measured for comparison with simulation results. Due to construction problems, the antenna does not remain symmetrical during the measurements. The E-plane is the most significantly affected. Although there are notable differences between the simulation and measurement results, the maximum directivity, as well as the general pattern shape compare well if the asymmetry is accounted for. The simulation software has a very good reputation for producing accurate results. Since the measurements are similar to the simulation results and the deviations are understood and accounted for, it is concluded that the modification is successful in yielding a round radiation pattern over a wide bandwidth.

2.5 Conclusion and Recommendations

An overall conclusion of the nature of the work done in this thesis is provided in Chapter 7. Some general recommendations are made.

Chapter 3

TEM Horn Antennas

The investigation into the suitability of TEM horns for an SKA feed commences with the analysis of some pre-existing designs. A linear tapered TEM horn [9], as well as an elliptical TEM horn with a Hecken impedance profile [3] are discussed.

The linear horn is chosen for analysis as it is the most basic and well known type of TEM horn antenna. The elliptical horn is a relatively new design, developed by Malherbe in [3] and [10] with the purpose of achieving a VSWR (voltage standing wave ratio) of less than 2 (or $|s_{11}| \leq -9.5$) [dB] over a wide bandwidth. This is achieved successfully over a frequency range of 70:1 in [10].

Since this project is focused on the radiation characteristics of TEM horn antennas, it is decided to compare the radiation characteristics of the novel elliptical TEM horn to those of the linear TEM horn, specifically in terms of achieving a round radiation pattern as discussed in Chapter 1.

3.1 Linear Tapered TEM Horn

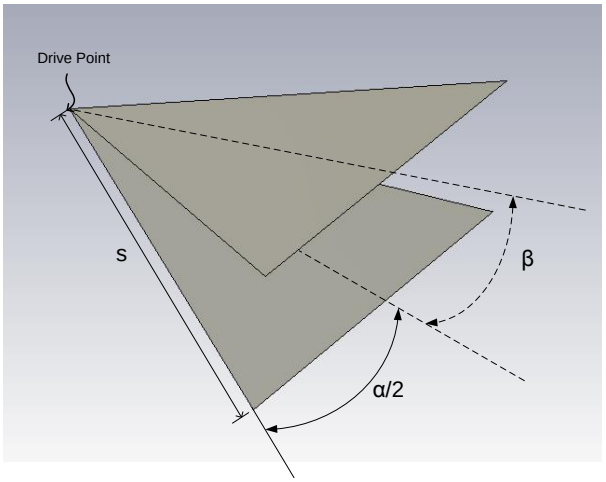

Figure 3.1: Basic linear TEM horn antenna. Adapted from [9]

A linear TEM horn is shown in Figure 3.1. It consists of two triangular plates which meet at a drive point as shown in Figure 3.1. The geometry of the linear horn can be described entirely in terms of the plate length, s, angular width, α and angular separation angle, β [9].

If the antenna becomes infinitely long, ($s \rightarrow \infty$) it can be described solely in terms of the angles α and β and is said to be frequency independent [7]. In this case (and for antennas that are relatively long), the characteristic impedance Z_c can be defined as a function of α and β only [9]. A linear TEM horn is regarded as relatively long if $s \geq 3\lambda$ and its characteristic impedance Z_c a function of α and β as shown Figure 3.2 [9].

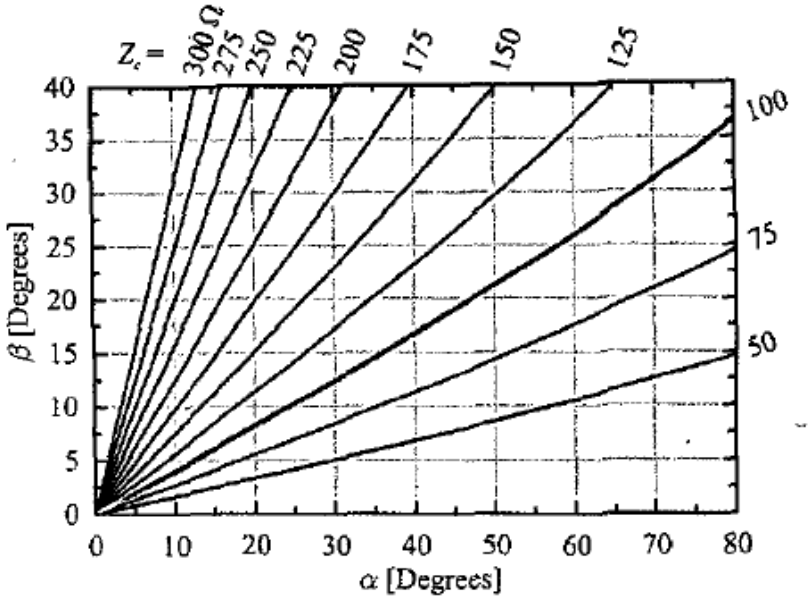

Figure 3.2: The characteristic impedance, Z_c of a linear TEM horn ($s \geq 3\lambda$) as a function of α and β [9].

The input impedance of an antenna with finite length, which is longer than 3λ, will approach the characteristic impedance of the structure [9]. Figure 3.3 illustrates that the magnitude of the real part (R) of the input impedance of a linear TEM horn as well as the imaginary part (X) are a function of the plate length s. The input impedance is defined as,

$$Z_{in} = R + jX \tag{3.1}$$

where

$$R = Z_c + A_R \tag{3.2}$$

and

$$X = 0 + A_X \tag{3.3}$$

where A_R is the deviation of R from the value of Z_c and A_X is the deviation of X from the value of 0.

According to [9], the magnitudes of A_R and A_X can be considered negligibly small when $s \geq 3\lambda$. Therefore, $R \approx Z_c$ and $X \approx 0$ so that the input impedance is said to approach Z_c for antennas that are relatively long ($s \geq 3\lambda$) [9]. For a characteristic impedance of 100 [Ω] , the values of A_x and A_R are less than 10 [Ω] for horns with $s > 3\lambda$ [9].

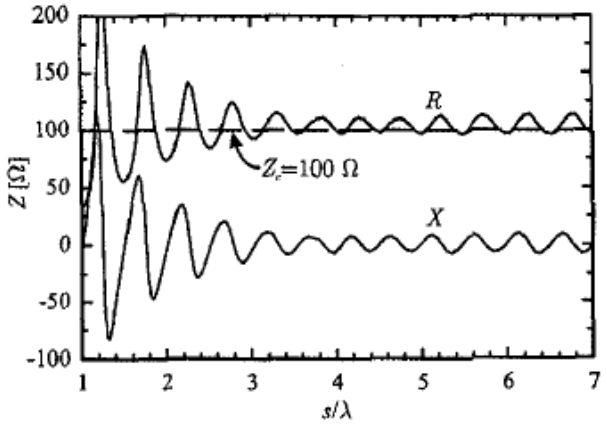

Figure 3.3: a

nd $\beta = 20$ [^{o}], and $Z_c = 100$ [Ω]]The input impedance, $Z = R + jX$, versus the electrical length of the TEM horn. For this specific antenna, $\alpha = 47.30$ [^{o}] and $\beta = 20$ [^{o}], and $Z_c = 100$ [Ω] [9].

The most general feed structure used for TEM horns is a parallel plate waveguide which is attached to the flared section as shown in Figure 3.4. A waveguide port is created at the back of the parallel plate section for excitation in CST simulations.

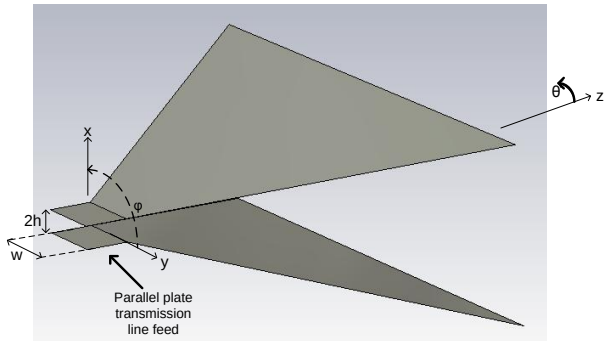

Figure 3.4: A TEM horn antenna with a parallel-plate waveguide feed

3.1.1 Influence of Flare Angle on Radiation Characteristics

This section discusses the behaviour of the directivity of a linear TEM horn for various values of the plate separation angle (or flare angle) β and the angular width α which are chosen from Figure 3.2 to keep the characteristic impedance of the antenna constant at $Z_c = 100$ [Ω]. The configuration in Figure 3.4 is used for the analysis.

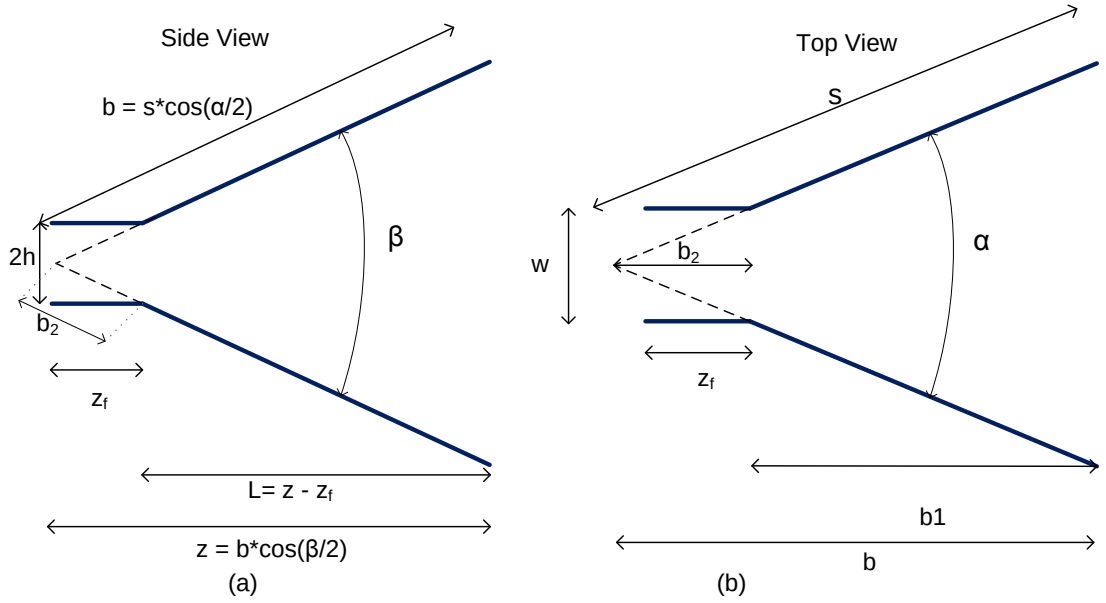

Figure 3.5: (a) Side and (b) Flattened-out top views of the linear tapered TEM horn with a parallel plate feed structure

The side and flattened-out top views of the horn are shown in Figure 3.5. It consists of the flared antenna section and a parallel plate feed section. The dimensions indicated in Figure 3.5 are discussed below:

- s - the length of the plates as for the basic TEM horn
- α - the angular width of the flared plates
- β - the angular separation between the flared plates
- z_f - length of the parallel plate feed section
- L - total **antenna** length
- w - the width of the parallel plate feed section
- h - half of the separation between the parallel feed plates

- b - the length of the flattened-out triangular plates, where $b = b_1 + b_2$
- z - the total length of the horn **and** feed section

The nominal set of parameter values for the linear TEM horn are indicated in Table 3.1. α and β are chosen from Figure 3.3 so that Z_c is equal to 100 [Ω]. The plate length, s is equal to 3 wavelengths at a frequency of 1 [GHz] so that the antenna can be regarded as relatively long ($Z_{in} \approx Z_c$).

Parameter	s [mm]	β [^{o}]	α [^{o}]	z_f [mm]
Value	900	20	47.5	15

Table 3.1: The set of nominal parameter values chosen for the linear tapered TEM horn

To determine the influence of plate separation on the radiation pattern, β is varied from 10 [^{o}] to 30 [^{o}] and the value of α is adjusted simultaneously to keep $Z_c = 100$ [Ω]. The H- and E-plane directivity of the linear TEM horn, for the various values of β, are shown in Figure 3.6 and Figure 3.7, respectively. Note that the values of α are obtained from Figure 3.2 for $Z_c = 100$ [Ω].

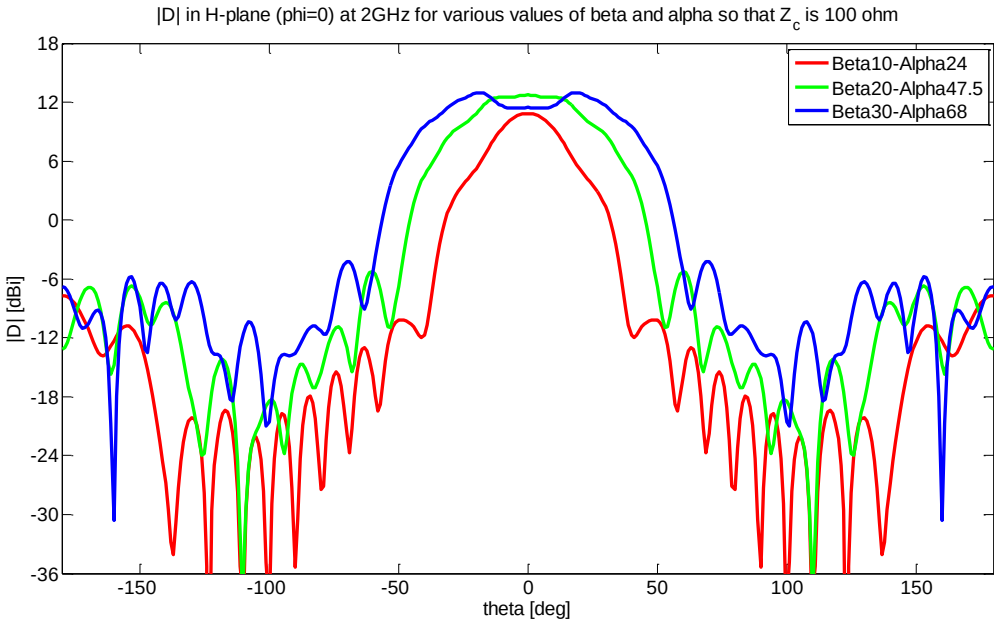

Figure 3.6: $|D|$ in the H-plane for various values of β and α which according to Figure 3.2 give $Z_c = 100$ [Ω]

Since the main lobes of the radiation patterns exhibit some break up in both the E- and H-planes, it is difficult to make a comparison using maximum directivity, HPBW and side lobe levels.

As discussed in [9], better insight into the effect of a larger plate separation angle can be obtained by looking at the directivity in linear scale in the $\phi = 0/180$ [^{o}] and $\phi = 90/270$ [^{o}]

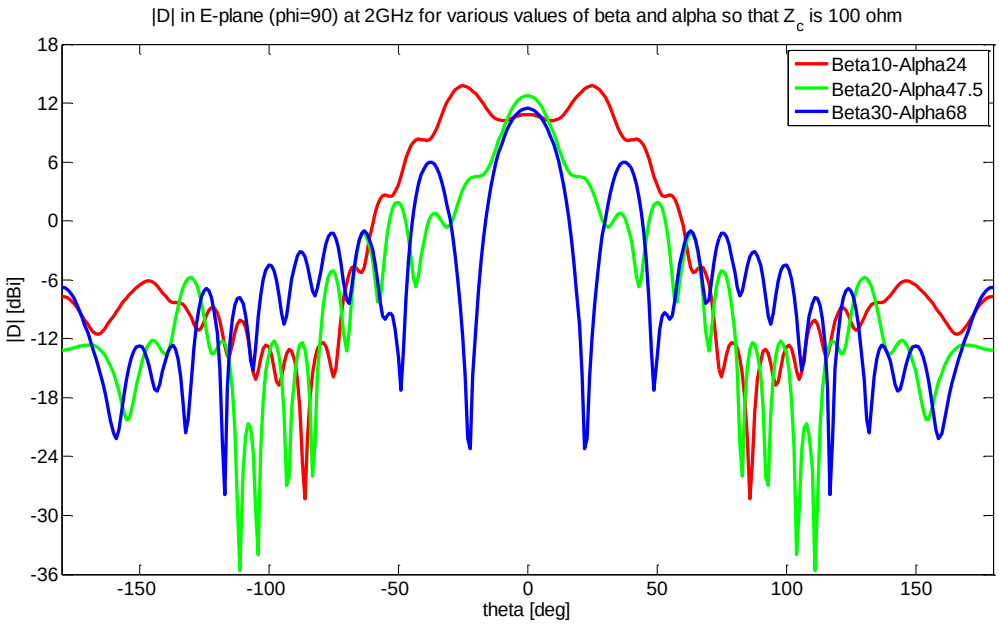

Figure 3.7: $|D|$ [dB] in the E-plane for various values of β and α chosen from Figure 3.2 to give $Z_c = 100$ [Ω]

planes. Figures 3.9 and 3.8 show the total linear directivity in the horizontal plane (H-plane) and the vertical plane (E-plane), respectively.

The pattern behaviour in both the E- and H-planes for is identical to those in [9] for the various values of β. Figure 3.10 is obtained from [9] and is used to explain the change in the E-plane pattern as β is increased, by discussing the effect for a simple Vee dipole antenna. Each arm of the Vee dipole antenna produces a symmetric pair of lobes with the directions of the radiated fields indicated as shown [9]. When β is small, the lobes A and A' (as well as B and B') partially overlap and their fields are subtracted. This results in a split beam as shown in Figure 3.8 (a). If β is increased, the lobes B and A' start to overlap and their fields add. This results in a directive main beam on the axis shown in Figures 3.8 (b) and (c).

Figure 3.9 shows how the H-plane directivity is influenced by increasing β. The behaviour is almost opposite to that of the E-plane behaviour and gives the indication that a round radiation pattern cannot be achieved using a linear TEM horn. The H-plane pattern behaviour is due to quadratic phase variation of the electric fields over the width of the aperture [9]. As β increases (and therefore α), so does the width at the aperture and thus the phase variation across the aperture. Therefore, the main beam in the H-plane will start to break up into a split beam as shown in Figure 3.9.

The E- and H-plane patterns are plotted on the same axes in Figure 3.11, for each set of β and α. The results clearly show that the E- and H-plane patterns are not equal and it can be concluded that the linear TEM horn is not is not a good candidate to achieve a round radiation pattern.

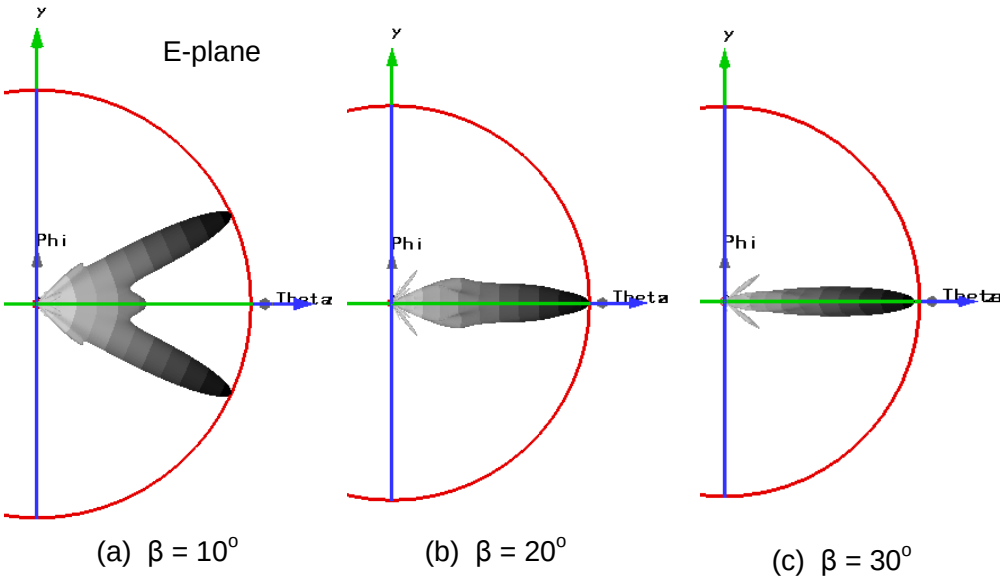

Figure 3.8: $|D|$ in the vertical plane for various values of β and α

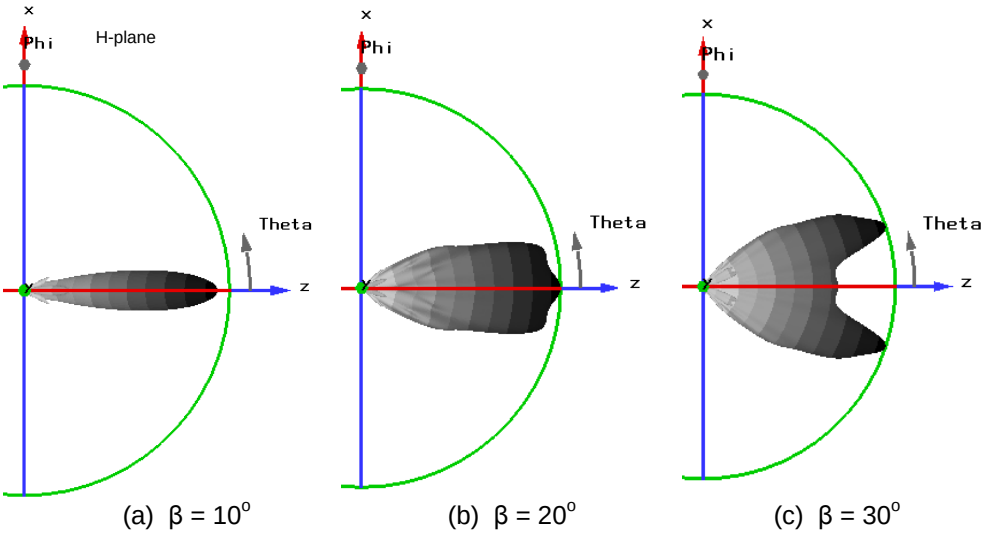

Figure 3.9: $|D|$ in the horizontal plane for various values of β and α

3.1.2 Frequency Variation of Radiation Characteristics

In order to compare the frequency variation of the radiation characteristics of the linear TEM horn to those of the elliptical/Hecken TEM horn [3] discussed in Section 3.2, some changes are made to the dimensions of the antenna.

Figure 3.12 shows the dimensions of the linear TEM horn relevant to the frequency analysis. To compare the performance of the two antennas, it is required that they have the same horizontal projected antenna length, the same aperture height as well as the same feed length. As the design of the elliptical horn is fixed, the values of the linear horn are adjusted.

The horizontal length of the antenna (L) must be equal to 480 [mm] from the end of the parallel

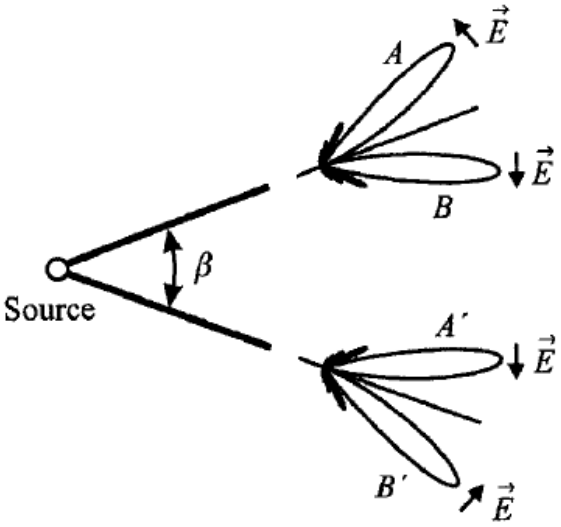

Figure 3.10: Linear horn approximated as a Vee dipole antenna to explain behaviour of directivity as β increases. [9]

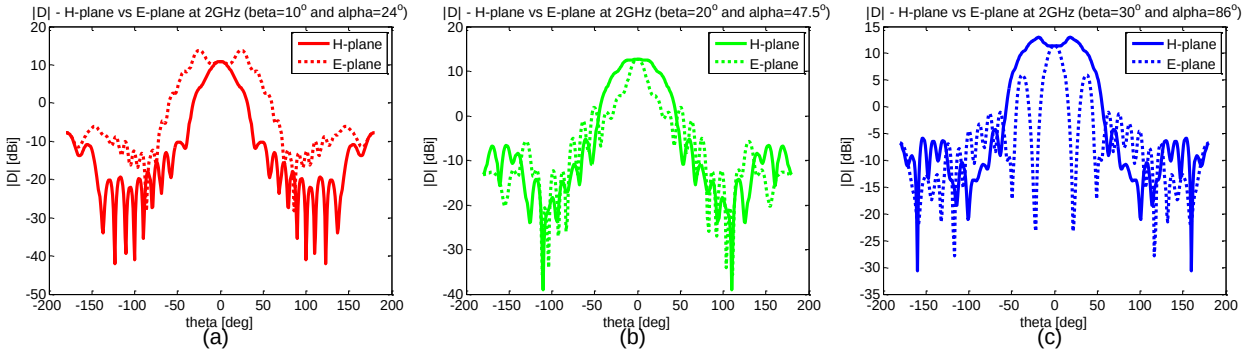

Figure 3.11: E- vs H-plane $|D|$ for various values of β and α which according to Figure 3.2 give $Z_c = 100$ [Ω]

plate section to the aperture. The initial feed length of 15 [mm] is used to determine the height and width of the parallel plate feed. This makes z in Figure 3.12 equal to 495 [mm]. For the comparison with the elliptical horn, the aperture height must also be equal to 733.5 [mm]. After these adjustments, the feed section is extended to be 100 [mm] in length as for the elliptical horn.

The fixed ration between z and h_{apt} gives an angle of 73.07 [^{o}] for β. A shorter plate length of $s = 800$ [mm] is chosen since the previous value of 900 [mm] will result in α exceeding 90 [^{o}]. Although s is slightly less than 3λ, the antenna is still regarded as relatively long.

Figure 3.13 (a) and (b) shows the H- and E-plane directivity of the linear TEM horn at 1, 4 and 7 [GHz]. Since both β and α are very large, the main lobes break up in both planes at most of the frequencies.

When comparing the E- and H-plane patterns on the same axes for each sample frequency in

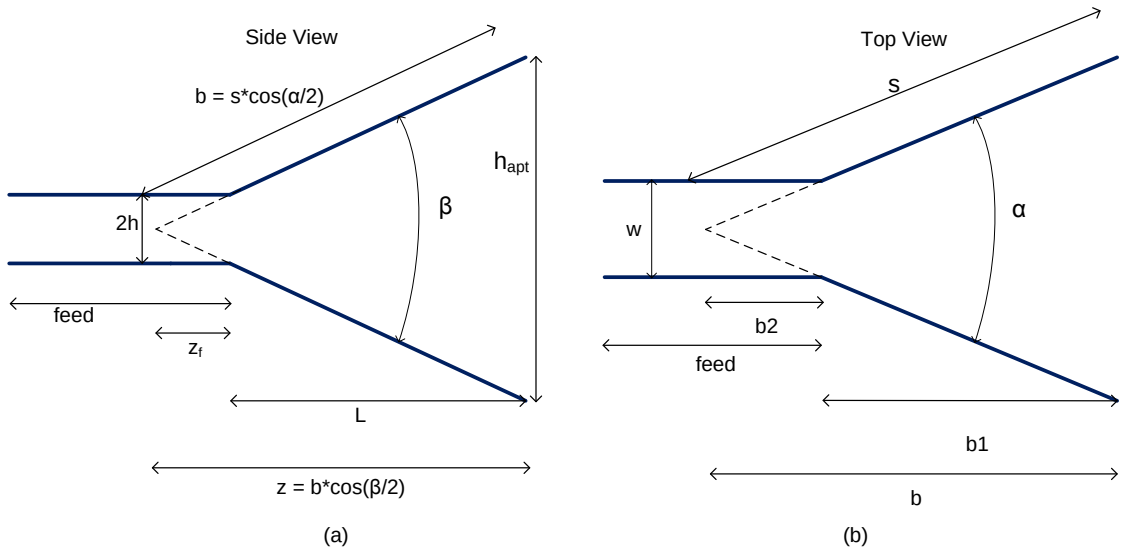

Figure 3.12: Linear tapered horn with added feed length for comparison with an elliptical TEM horn

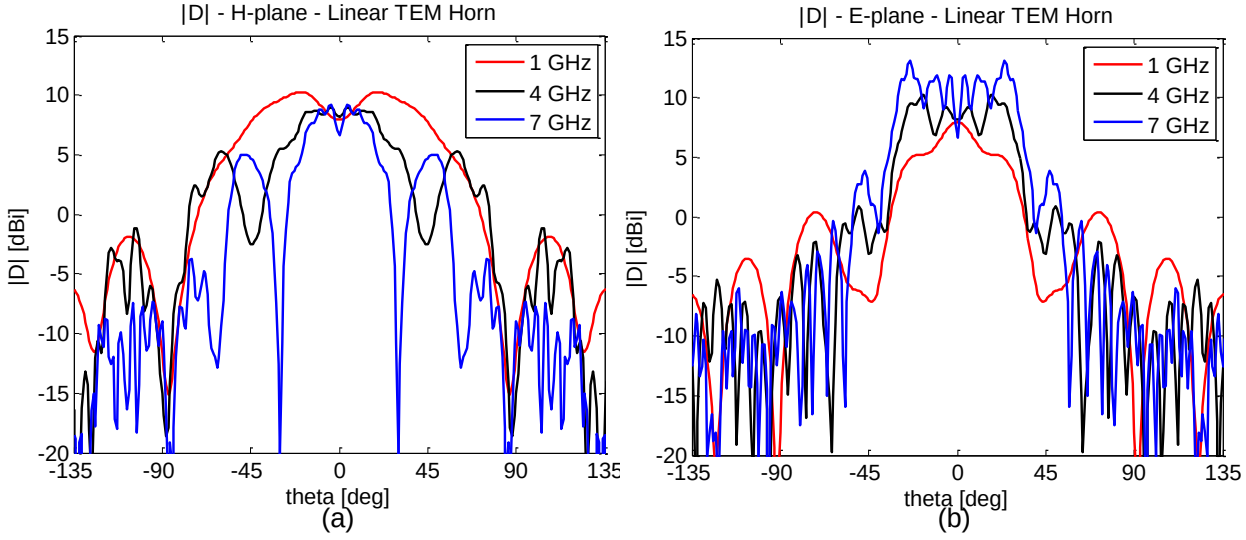

Figure 3.13: $|D|$ for the linear TEM horn: (a) H-plane (b) E-plane

Figure 3.14, it is clear that a round pattern is not achieved. Although the E- and H-plane patterns correspond better at 4 [GHz] than at the other sample frequencies, the break up of the main beams is not desirable. The antenna cannot be said to perform better at one frequency than another. It is concluded that a linear TEM horn will not yield a round radiation pattern over a wide bandwidth.

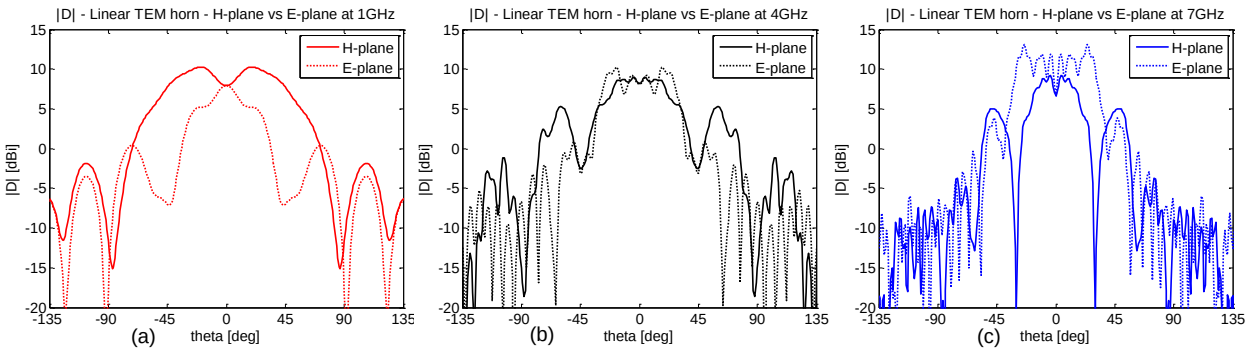

Figure 3.14: E- vs H-plane $|D|$ for the linear TEM horn: (a) 1 [GHz] (b) 4 [GHz] (c) 7 [GHz]

3.2 Elliptically Tapered TEM Horn with a Hecken Impedance Taper

This section discusses the radiation characteristics of an elliptical TEM horn with a Hecken impedance profile, shown in Figure 3.15. The antenna is presented in [3] and is designed with the focus on achieving the lowest possible reflections ($s_{11} \leq -9.5$ [dB]) using an optimum impedance taper to transform the feed impedance of $Z_o = 50$ [Ω], to the characteristic impedance of free space $\eta_o = 377$ [Ω]. This is achieved successfully in [10] for a bandwidth of 70:1. This section will, however, focus on the farfield radiation characteristics of the antenna so as to determine whether it offers an improvement on the linear TEM horn, in terms of the SKA criteria of a round radiation pattern.

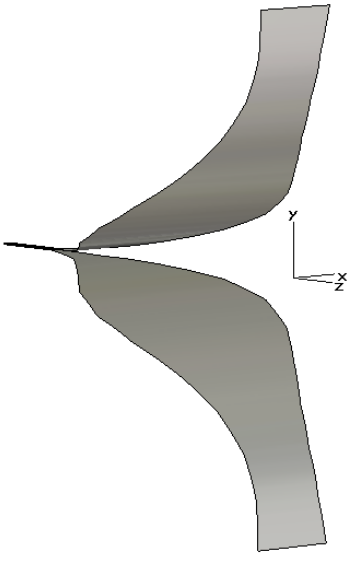

Figure 3.15: Elliptical TEM horn with a Hecken impedance profile

3.2.1 Theory

Figure 3.16 shows the side and flattened top views of the horn. It has an elliptical profile when viewed from the side and the width profile, obtained from [3], makes use of Hecken impedance function to transform the feed impedance of 50 [Ω] to 377 [Ω] at the mouth of the horn.

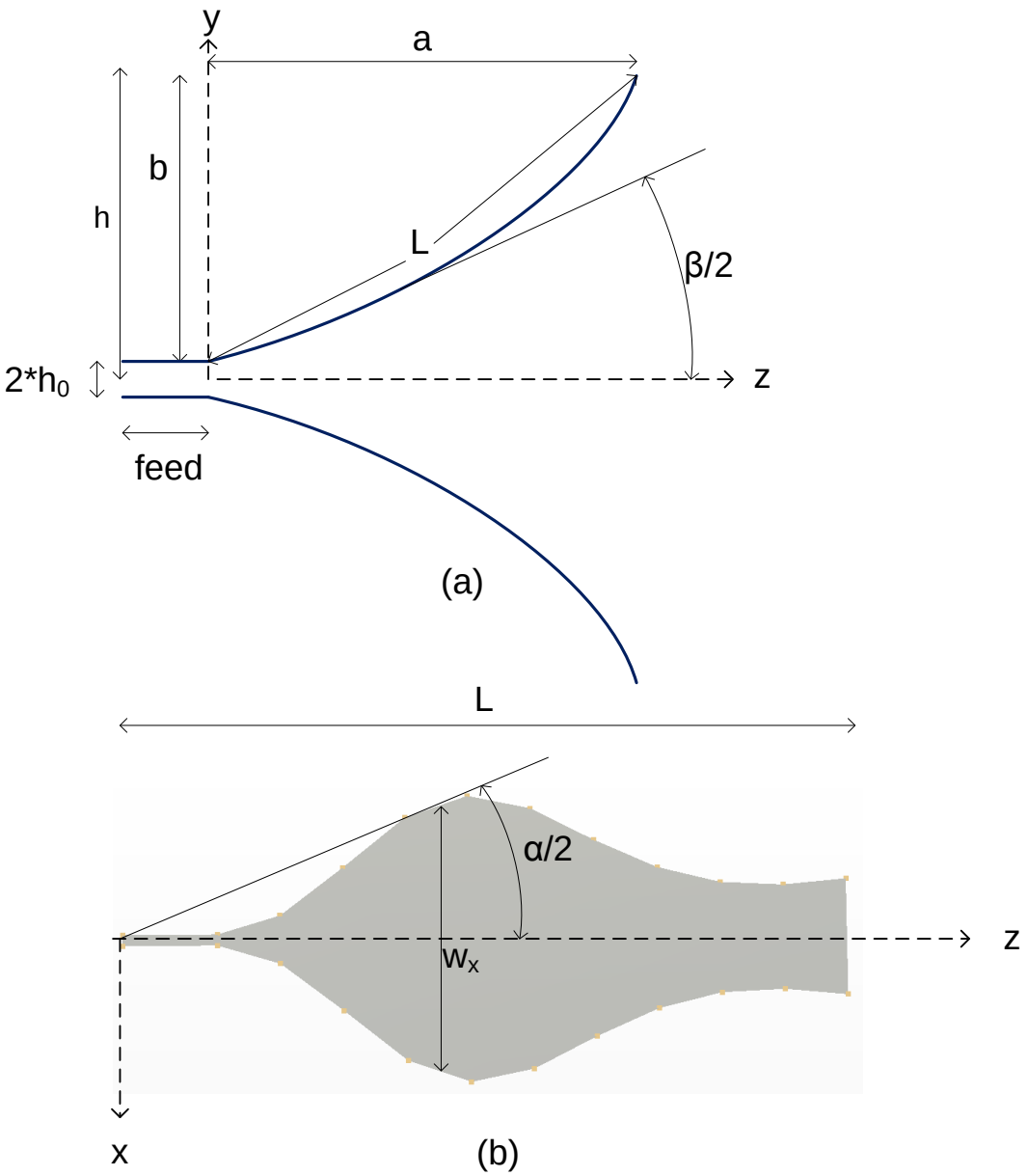

Figure 3.16: (a) Side profile of the elliptical horn and (b) a flattened top view of the horn

In contrast to the linear horn, the angles α and β are now functions of z but still define the characteristic impedance at any point on the structure [3].

The elliptical surface is described by,

$$\frac{z^2}{a^2} + \frac{(y-h)^2}{b^2} = 1 \tag{3.4}$$

and the parameter m can be defined as,

$$m = e^2 = 1 - \frac{b^2}{a^2} \tag{3.5}$$

where e is the eccentricity of the ellipse. The arc length L is given by the complete elliptical integral of the second kind,

$$L = a \times E(m) = a \int_0^{\pi/2} \sqrt{1 - m \sin^2 \theta} d\theta \tag{3.6}$$

The curved length, L will determine the lowest frequency at which the horn will function [3]. In [3], the elliptical radii are chosen with values of $a = 480$ [mm] and $b = 366$ [mm] which gives $E(m) = 1.3860625$ so that the arc length of the ellipse, L is approximately equal to 665.30 [mm].

Table 3.2 shows the set of points used to draw the flattened top view profile of the horn and were obtained by adapting the procedure described in [3]. These points are indicated by the small yellow dots in Figure 3.16 (b) and are joined with straight line segments.

z	0	66.53	133.06	199.59	266.12	332.65	399.18	465.71	532.24	598.77	665.3
$w(x)$	12.1	52.9	156.8	266.2	313.4	285.3	215.4	154.6	121.0	114.4	127.2

Table 3.2: The set of points used to draw the flattened top profile of the elliptical/Hecken TEM horn

The profile described by Table 3.2 is bent towards the elliptical curve which is plotted using the points in Table 3.3.

z	0	66.5	132.2	196.6	258.2	316.1	368.7	413.7	449.3	472.0	480.0
y	0	3.53	14.16	32.11	57.46	90.57	131.65	180.39	237.21	299.46	366

Table 3.3: The set of points used to define the elliptical side profile

The two antenna plates are shifted apart by $d_o = 1.53[mm]$, so that $Z_o = 50$ [Ω]. A theoretical value of $d_o = 1.6$ [mm] is calculated using Equation 6.1 [11] and the value is optimised in CST to give a 50 [Ω] port impedance.

$$Z_0 = \frac{\eta d}{w} \tag{3.7}$$

A parallel plate feed section of length 100 [mm] is added to the back of the antenna as for the linear TEM horn.

3.2.2 Influence of Frequency Variation on Radiation Characteristics

This section discusses the influence of frequency variation on the radiation characteristics of the elliptical/Hecken TEM horn. Due to the complexity of the design, the influence of the dimensions of the antenna are not investigated.

Figure 3.17 (a) shows the H-plane directivity of the elliptical TEM horn at 1, 4 and 7 [GHz], whereas Figure 3.17 (b) shows the E-plane directivity at these frequencies. The E- and H-plane patterns are also plotted on top of one another at each sample frequency, as shown in Figure 3.18.

The elliptical horn performs poorly at 1 [GHz], with the main lobe splitting into three large lobes in the H-plane. The E-plane performance is not much better at this frequency. Although less pronounced at 4 and 7 [GHz], the pattern break-up is considered significant as the main beams contain ripples greater than 1 [dB].

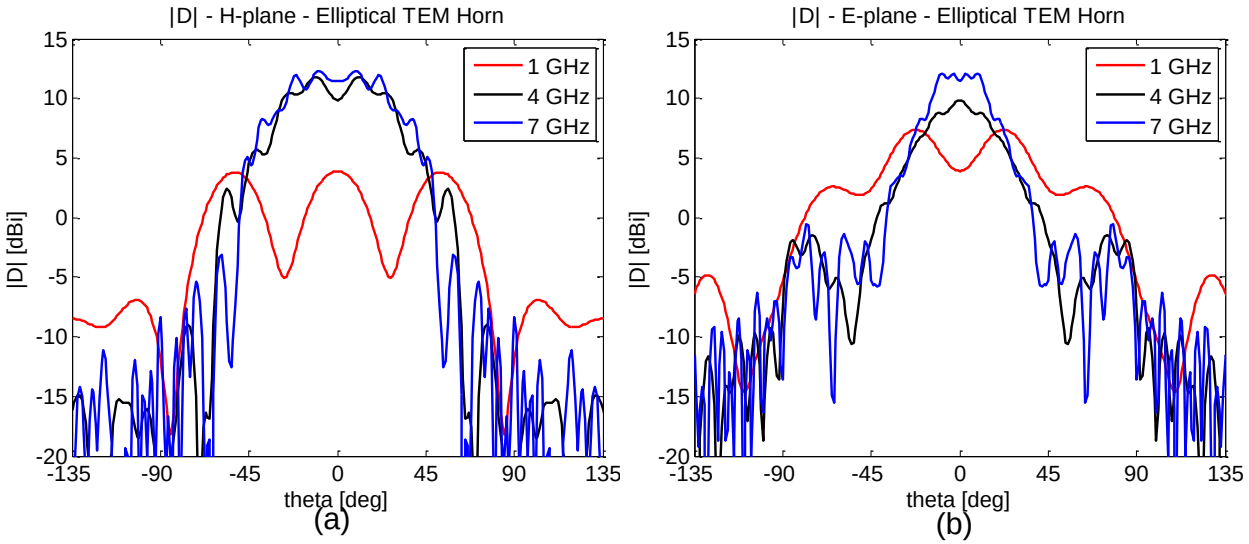

Figure 3.17: $|D|$ for the elliptical TEM horn: (a) H-plane (b) E-plane

Figure 3.18 shows that the antenna does not perform well in terms of yielding a round radiation pattern over a wide bandwidth.

3.3 Conclusion

The results of this chapter indicate that neither the linear TEM horn, nor the elliptical TEM horn yield a round radiation pattern over a wide bandwidth. It is difficult to say which one of the linear or elliptical TEM horns is better than the other in terms of radiation characteristics. The main beam of the directivity in both the E- and H-planes showed significant break up at the sample frequencies for both antennas. This made it difficult to compare the two antennas in terms of maximum directivity, angular width and side lobe levels. With the focus on achieving a round radiation pattern over a

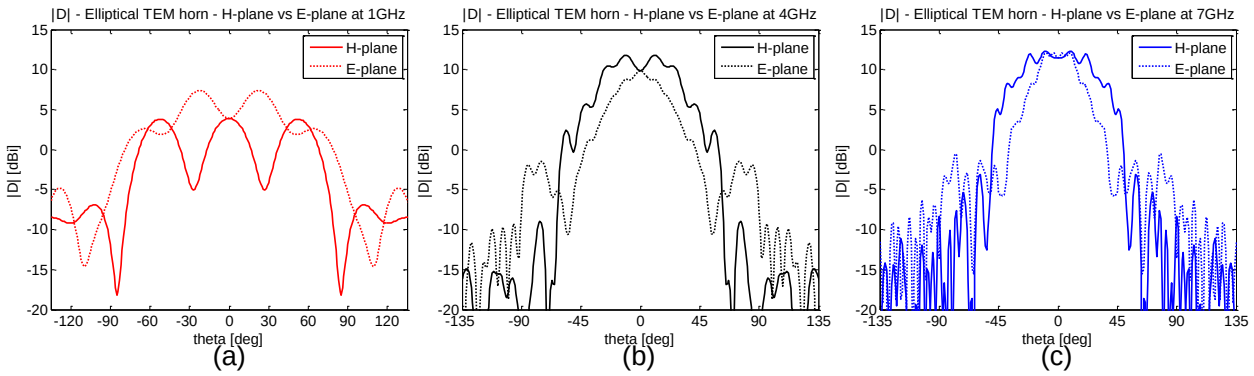

Figure 3.18: E- vs H-plane $|D|$ for the elliptical TEM horn

wide bandwidth, neither the linear TEM horn nor the elliptical/Hecken TEM horn perform well in this regard and an improved design is required.

Although the TEM horns discussed in this chapter do not meet the criteria for the purposes of this project, TEM horns are widely used for their ultra-wideband characteristics, relatively good gain and low side-lobe levels. Novel designs such as the elliptical TEM horn are able to achieve very low reflections ($VSWR \leq 2$ or $s_{11} \leq -9.5$ [dB]) over a wide bandwidth, with the elliptical TEM horn [3] achieving this over an impressive frequency range of 70:1 [10].

A modification to an exponential TEM horn antenna is prosed in Chapter 6, which is successful at achieving a round radiation pattern over a wide bandwidth.

Chapter 4

Method of Moments

The Method of Moments (MoM) is a numerical method used in Computational Electromagnetics (CEM) to reduce integrodifferential equations, such as the Electric Field Integral Equation, to a set of simultaneous linear algebraic equations [12]. This chapter serves as an introduction to the MoM by using it to solve for the current distribution on a straight, thin wire dipole antenna.

4.1 Electric Field Integral Equation (EFIE)

The total (tangential) electric field (E^{tan}) on the surface of a conductor is defined in Equation 4.1 as the sum of the incident and scattered electric fields [12].

$$\mathbf{E}^{tan} = \mathbf{E}^{i} + \mathbf{E}^{S} \tag{4.1}$$

Since $\mathbf{E}^{tan} = 0$ on the surface of a perfect electrical conductor (PEC), the sum of the incident and scattered fields is forced to zero by the boundary condition,

$$\hat{\mathbf{n}} \times (\mathbf{E}^{i} + \mathbf{E}^{S}) = 0 \tag{4.2}$$

so that,

$$\mathbf{E}^{i} = -\mathbf{E}^{S} \tag{4.3}$$

The scattered electric field $\mathbf{E}^{s}$ can be calculated by,

$$\mathbf{E}^{S} = -j\omega\mathbf{A} - \nabla\Phi \tag{4.4}$$

where $\mathbf{A}$ and $\mathbf{\Phi}$ are the magnetic vector potential and electric scalar potential, respectively. $\mathbf{A}$ is defined in terms of the surface current density $\mathbf{J}$ as,

$$\mathbf{A}(\mathbf{r}) = \frac{\mu}{4\pi}\int_{S} \mathbf{J}\frac{e^{-jkR}}{R}dS' \tag{4.5}$$

,where $R = |\mathbf{r} - \mathbf{r}'|$ with $\mathbf{r}$ the location of the observation point where the electric field is calculated and $\mathbf{r}'$ being the coordinates of the source generating the electric field [12].

Φ is defined in Equation 4.6 in terms of the surface charge density σ_S [12].

$$\mathbf{\Phi}(\mathbf{r}) = \frac{1}{4\pi\epsilon}\int_S \sigma\frac{e^{-jkR}}{R}dS' \tag{4.6}$$

Equations 4.3-4.6 are the constituents of the **EFIE** which is defined as,

$$-\mathbf{E}^i = -j\omega\mathbf{A} - \nabla\Phi \tag{4.7}$$

The purpose of the Method of Moments is to reduce Equation 4.7 to a set of simultaneous linear algebraic equations.

4.2 Pocklington's Integral Equation

Pocklington's integral equation is an approximation of the EFIE, for the case of straight wire conductors that are sufficiently thin. A wire is considered sufficiently thin if,

$$r << \lambda \tag{4.8}$$

,where r is the wire radius and λ is the wavelength at the (lowest) design frequency.

This section provides the derivation of Pocklington's integral equation, as discussed in [7] and [12], for a thin wire such as in Figure 4.1 (a). The wire has a radius of $r = a$ and a z-directed surface current density $J(\phi, z)$, which is dependent on its position along the length of the wire (z) as well as its position on the circumference (ϕ).

Approximations, which simplify the calculation of the current density, can be used if the radius of the wire is sufficiently thin. Before discussing the assumptions upon which the approximations are based, the EFIE is expressed in terms of only the magnetic vector potential.

The Lorentz gauge is often used to express Φ in terms of A_z [12],

$$\nabla \cdot \mathbf{A} = -j\omega\mu\epsilon\Phi \tag{4.9}$$

and since we are solving for the z-directed surface current, Equation 4.9 can be reduced to,

$$\frac{\partial A_z}{\partial z} = -j\omega\mu\epsilon\Phi \tag{4.10}$$

Therefore, the EFIE can be rewritten as,

$$-E_z^i(\mathbf{r}) = \frac{1}{j\omega\mu\epsilon}\left(k^2 A_z + \frac{\partial^2 A_z}{\partial z^2}\right) \tag{4.11}$$

where $k = \sqrt{\mu\epsilon} = 2\pi/\lambda$ and

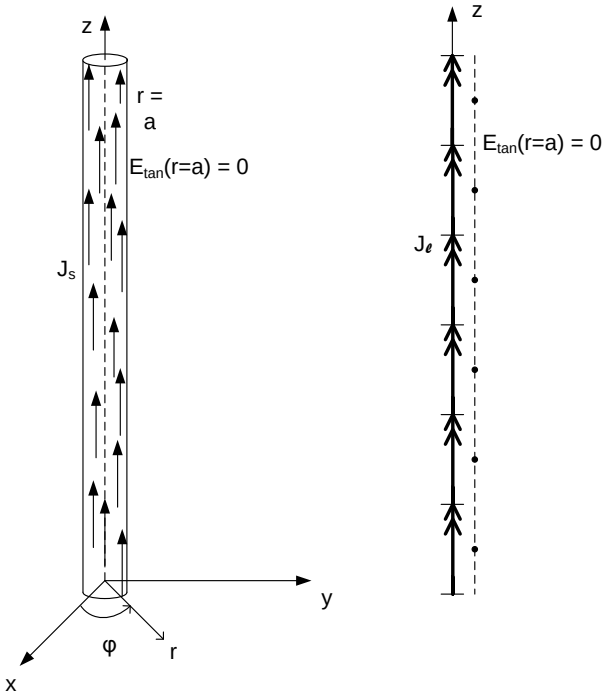

Figure 4.1: Thin wire: (a) z directed surface current (b) z directed line current

$$A_z = \frac{\mu}{4\pi}\int_0^l\int_0^{2\pi} J_z(\phi',z')\frac{e^{-jk|\mathbf{r}-\mathbf{r}'|}}{|\mathbf{r}-\mathbf{r}'|}ad\phi' dz' \tag{4.12}$$

Substituting Equation 4.12 into Equation 4.11 yields,

$$E_z^s(\mathbf{r}) = \frac{1}{j\omega\epsilon}\int_0^{2\pi}\int_0^l J_z(\phi',z')\Big(\frac{\partial^2\psi(z,z')}{\partial z^2} + k^2\psi(z,z')\Big)adz'd\phi' \tag{4.13}$$

where $\psi(z,z') = \frac{e^{-jk|\mathbf{r}-\mathbf{r}'|}}{4\pi|\mathbf{r}-\mathbf{r}'|}$ is the free space Green's Function [12]. The differentiation may be taken into the integral since integration is with respect to the source points (z',ϕ'), whereas differentiation is with respect to the observation points (z,a).

The complexity of Equation 4.13 can be significantly reduced by making use of the following assumptions and approximations for a sufficiently thin wire ($r = a << \lambda$):

- The surface current can be replaced with a z-directed line current. Therefore, it can be assumed that the axial current density $J(z')$ does not vary circumferentially (independent of ϕ') [12] and $\mathbf{r}' = z'\hat{z}$.

- The boundary condition, $\mathbf{E}^{tan} = 0$ is still enforced at $r = a$ so that $\mathbf{r} = a\hat{r} + z\hat{z}$. This is done to avoid the singularity present in the Green's Function at $z = z'$ [12].

Figure 4.1 shows how the z-directed surface current density distribution on the thin wire is equivalent to a line current density distribution ($\mathbf{J} = \mathbf{J_l}$) on the z-axis, whilst still enforcing the

boundary condition at $r = a$. The properties assumed for a thin wire reduce Equation 4.13 to Pocklington's integral equation [7]:

$$E_z^s(\mathbf{r}) = \frac{1}{j\omega\epsilon}\int_0^l J_z(z')\left(\frac{\partial^2\psi(z,z')}{\partial z^2} + k^2\psi(z,z')\right)adz' \tag{4.14}$$

After differentiating A_z and combining the terms, Pocklington's equation is reduced to,

$$E_z^i(z = z, r = a) = -\frac{1}{j\omega\epsilon}\int_0^l J_z(z')\frac{e^{-jkR}}{4\pi R}\Big[(1 + jkR)(2R^2 - 3a^2) + (kaR^2)\Big]dz' \tag{4.15}$$

where $R = |\mathbf{r} - \mathbf{r}'| = \sqrt{(z - z')^2 + a^2}$. The term, $\frac{e^{-jkR}}{4\pi R}\Big[(1 + jkR)(2R^2 - 3a^2) + (kaR^2)\Big]$ will be written as $P(z, z')$ throughout the rest of the text.

4.3 Approximating the Current

The MoM requires the wire in Figure 4.1 to be broken up into a finite number of segments N. The current density distribution on the wire is approximated as the weighted sum of a set of basis functions. Each basis function $h_n(z')$ is associated with an unknown constant weighting coefficient I_n and depending on the type of basis function, represents part of or all of the current on segment N (or segment N and segment (N+1)). The total current density anywhere on the wire is expressed as,

$$J_z(z') \cong \sum_{n=1}^{N} I_n h_n(z') \tag{4.16}$$

The length of each segment is equal to $\Delta = L/N$, starts at position $z_n = (n - 1)\Delta$ and ends at position $z_{n+1} = n\Delta$. Depending on the type of basis function used, there will be $M = N$ or $M = N - 1$ observation/test points at which the EFIE will be evaluated. These will be located at positions $\mathbf{r} = z_m\hat{i}_z + a\hat{i}_\rho$. Using Equation 4.16, the incident electric field at a point $(z = z, r = a)$ on the thin wire in Figure 4.1 is expressed as,

$$E_z^i(z = z_m, r = a) = -\frac{1}{j\omega\epsilon}\int_0^l \sum_{n=1}^{N} I_n h_n(z')P(z, z')dz' \tag{4.17}$$

and the MoM is used to solve for the unknown current density coefficients I_n.

4.3.1 Basis Functions

There are many types of basis function which can be used to represent the current on a wire segment. The three different types implemented for comparison are:

- Constant/Pulse Basis Functions

- Triangular Basis Functions
- Sinusoidal Basis Functions

The differences between their formulations are discussed below and the results of their implementations are compared in Section 4.4.

Constant/Pulse Basis Functions The constant or pulse basis function is the most basic type of basis function used to represent the current on a thin wire. Each basis function h_n is defined as [7],

$$h_n(z') = \begin{cases} 1, & \text{for } (n-1)\Delta \leq z' \leq n\Delta \\ 0, & \text{elsewhere} \end{cases} \tag{4.18}$$

The current on each segment n is then approximated as a pulse basis function multiplied by a constant current coefficient I_n. The current coefficients are the unknowns for which the MoM solves.

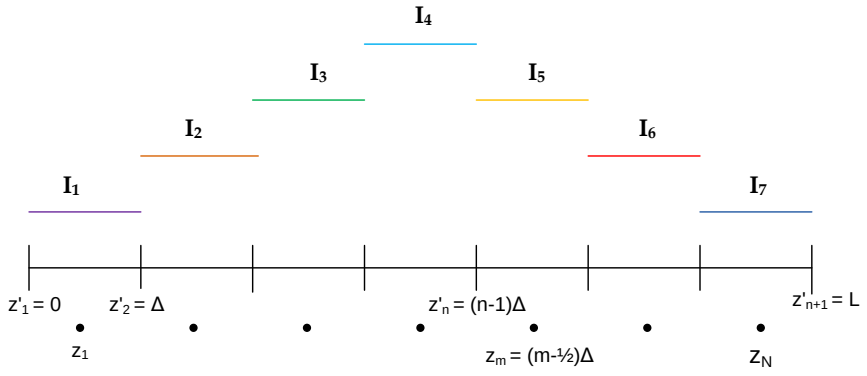

Figure 4.2: Example of constant basis functions and their respective current coefficients I_n used to approximate the current on a thin wire

Figure 4.2 shows an example of the basis functions multiplied by their corresponding amplitudes I_n for a wire broken into $N = 7$ segments. The current distribution shown in Figure 4.2 is typical for a half wavelength dipole, which is used in Section 4.4 to test the implementation of the MoM for thin wires using the various basis functions. There are $M = N$ test points (indicated by the black dots), at which the field will be calculated to form N simultaneous equations to solve for the N coefficients I_n. At a point z_m, the EFIE becomes,

$$\begin{aligned} E^i_z(z = z_m, \rho = a) = (-\frac{1}{j\omega\epsilon}\int_0^l \sum_{n=1}^{N} I_n h_n(z')P(z_m, z')dz') = (-\frac{1}{j\omega\epsilon}\int_0^{\Delta} I_1 h_1(z')P(z_m, z')dz') + \\ (-\frac{1}{j\omega\epsilon}\int_{\Delta}^{2\Delta} I_2 h_2(z')P(z_m, z')dz') + \cdots + \\ (-\frac{1}{j\omega\epsilon}\int_{L-\Delta}^{L} I_N h_N(z')P(z_m, z')dz') \end{aligned} \tag{4.19}$$

E^i will be equal to zero at all test points on the PEC *except* at the point which corresponds to the source. In this case, the thin wire is a dipole antenna which is fed at its centre by a voltage source. The purpose of the procedure is to solve for the unknown coefficients I_n and since $E^i(z = L/2) \neq 0$, a set of simultaneous equations with a unique solution is formed. The set of simultaneous equations can be represented by the matrix equation $E = [Z]I$, where E is the column vector representing the electric field at the M test points, Z is an $m \times n$ matrix and I is the column vector containing the coefficients I_n. The individual elements in the matrix equation are:

$$\begin{aligned} E_m = &\quad E^i(z_m, a) \\ I_n = &\quad I_n \\ Z_{mn} = &\quad -\tfrac{1}{j\omega\epsilon}\int_{(n-1)\Delta}^{n\Delta} h_n(z^{'})P(z_m, z^{'})dz^{'} \end{aligned} \tag{4.20}$$

It is important to note that an *odd* number of segments must be chosen when using constant basis functions so that the $(\frac{N+1}{2}^{th})$ test point corresponds to the location of the source. Although the pulse basis function is the most simple and computationally efficient for MoM calculations, greater accuracy can be achieved by using more complex basis functions such as the triangular basis function or the piecewise sinusoid.

Triangular Basis Functions Figure 4.3 shows triangular or piecewise linear basis functions multiplied by unknown amplitudes I_n. The maximum height of the triangular pulse is also normalised to 1 unit so that the current on the wire is equal to $\sum_{n=1}^{N-1} I_n h_n(z^{'})$. The basis functions are defined as [7],

$$\mathbf{h}_n(z^{'}) = \begin{cases} \frac{z^{'}-z_n^{'}}{z_{n+1}^{'}-z_n^{'}}, & \text{if } z_n^{'} \leq z^{'} \leq z_{n+1}^{'} \\ \frac{z_{n+2}-z_n}{z_{n+2}^{'}-z_{n+1}^{'}} & \text{if } z_{n+1}^{'} \leq z^{'} \leq z_{n+2}^{'} \\ 0 & \text{otherwise} \end{cases} \tag{4.21}$$

Each triangular basis function (which consists of two intersecting straight lines) spans *two* segments and can be considered as consisting of a positive and a negative half basis function. In Figure 4.3 the positive half functions would be the straight line segments which have positive gradients and are defined by the first case of Equation 4.21. Similarly, the negative half basis functions correspond to the straight lines with negative gradients and are defined by the second case in Equation 4.21.

With this type of basis function, $(N - 1)$ basis functions are required to represent the current over N segments. The EFIE is evaluated at $(N - 1)$ test points indicated by the black dots, where N is an *even* number to ensure that the source corresponds to a middle test point. The the matrix equation used to solve for the current coefficients is set up in a similar manner as for the pulse basis functions.

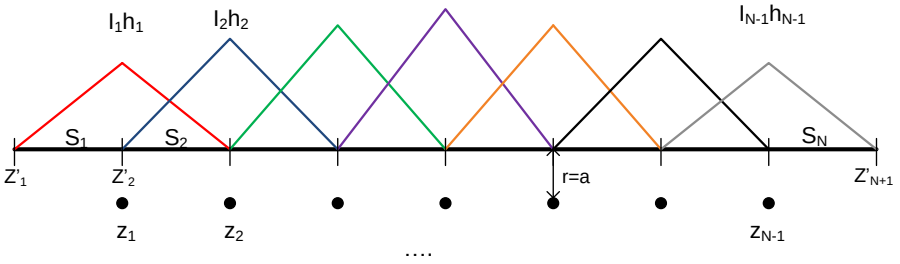

Figure 4.3: Triangular basis functions and their corresponding current coefficients

The triangular basis functions should result in a smoother and more accurate representation of the current than the pulse basis functions for equal N. This is expected since the steps of the pulse basis function are discontinuous whereas the straight line segments add up so that there is a continuous transition from one basis function to the next. The only disadvantage is that it takes slightly longer to implement the code, which must also do more calculations at the same speed.

Sinusoidal Basis Functions Sinusoidal basis functions generally offer an even more accurate result than triangular basis functions and are defined by Equation 4.22 [7].

$$\mathbf{h}_n(z') = \begin{cases} \frac{sin[k(z'-z'_n)]}{sin[k(z'_{n+1}-z'_n)]} & \text{if } z'_n \leq z' \leq z'_{n+1} \\ \frac{sin[k(z'_{n+2}-z'_n)]}{z'_{n+2}-z'_{n+1}} & \text{if } z'_{n+1} \leq z' \leq z'_{n+2} \\ 0 & \text{otherwise} \end{cases} . \tag{4.22}$$

$k = \frac{2\pi}{\lambda}$ is the wavenumber, where λ is the wavelength defined in terms of the operating frequency. Therefore, the length of each segment ($\Delta = L/N$) is generally much less than the period of the sinusoid [13]. Figure 4.4 shows three sinusoidal basis functions multiplied by their current coefficients for a wire broken up into $N = 4$ segments. The current density distribution obtained by adding the basis functions is indicated by the dotted line.

As $\Delta << \frac{2\pi}{\lambda}$, the basis functions in Figure 4.4 may appear triangular. However, each basis function consists of two intersecting sinusoids which are restricted by the domains specified in Equation 4.22. Each basis function spans two segments and consists of a positive half basis function which is defined by the first case in Equation 4.22, as well as a negative half basis function defined by the second case in Equation 4.22. When using sinusoidal basis functions, the number of segments N must also be *even* and the test points are chosen in the same way as for the triangular basis functions. The procedure to set up the matrix equation is the same as for the other types of basis functions.

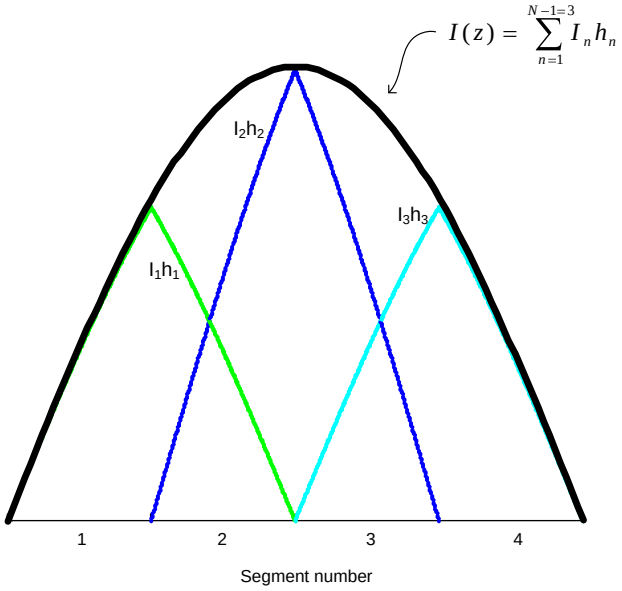

Figure 4.4: Sinusoidal basis functions and their corresponding current coefficients which add to give the current distribution on the thin wire

4.4 Implementation and Results

MATLAB code is developed to solve for the current density distribution on a thin wire dipole antenna by using the three different types of basis functions. This section discusses and compares the results achieved with the different basis functions. The simulation software, FEKO, which makes use of the MoM, is used to determine the accuracy of the results produced with the in-house code.

The dipole antenna which is analysed is a thin wire such as the one in Figure 4.1, fed at its center with a voltage source. It is analysed at a frequency of 1 [GHz] and is half a wavelength long so that $L = \lambda/2$. The wire radius is chosen $r = \lambda/100$ and the dipole is fed at its centre by a gap voltage source which generates an electric field:

$$E_s = V_s/d \tag{4.23}$$

where d is assumed equal to the length of a segment.

V_s is chosen equal to 1 [V] in FEKO and it is assumed that it will generate an electric field defined by Equation 4.23. This value is then used in the in-house code as the excitation source. The fields at the test points (elements of $[E_m]$) are equal to zero everywhere, except for the observation point at $z = L/2$ which coincides with the excitation source. This value is set equal to E_s, which is the field generated by the voltage source.

Figure 4.5 shows the magnitude of the current distribution calculated with the simulation software, FEKO for $N = 12$ segments and $N = 22$ segments.

It is important to note that the magnitude of the current density makes a slight dip around the

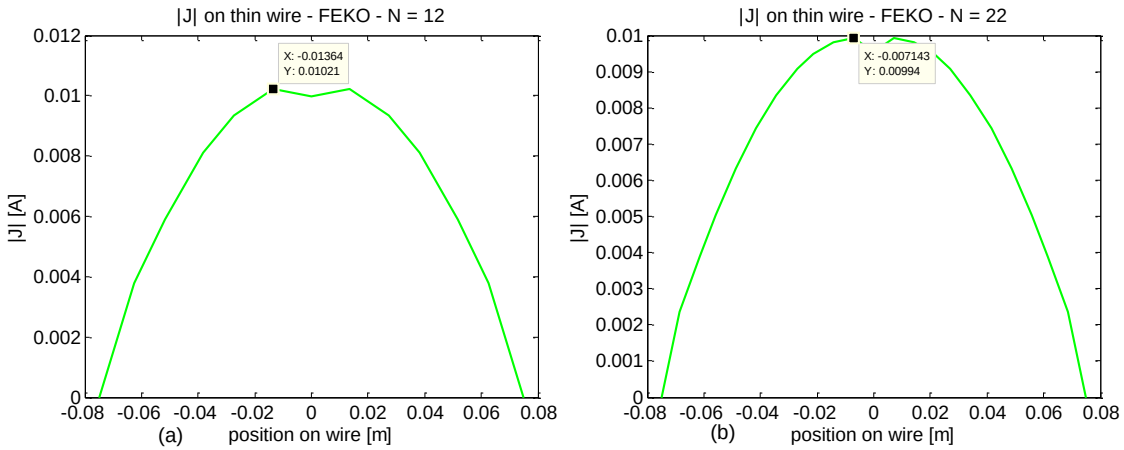

Figure 4.5: Current on a $\lambda/2$ thin wire dipole antenna calculated by FEKO: f = 1 [GHz] $N = 12$ and $N = 22$ segments

middle of the wire, and is not a maximum at this position as would be expected. This is because a half-wavelength dipole antenna resonates at a length that is slightly less than 0.5λ, which is usually 0.47λ or 0.48λ [7]. The thinner the wire becomes, the closer the resonating length is to 0.48λ.

The results obtained with the code implemented in MATLAB will be compared to the FEKO results.

4.4.1 Constant Basis Functions

Figure 4.6 (a) and (b) show the magnitude of the current density distribution on the $\lambda/2$ dipole, calculated in MATLAB using constant basis functions for $N = 11$ and $N = 21$ segments. The stair step graphs are the actual current distribution represented by the basis functions. Linear interpolation is performed using the midpoints of the basis functions so that the half-wave sinusoidal distribution is clear.

The maximum value of $|J|$ achieved with $N = 11$ is 31.8% lower than the value calculated by FEKO for $N = 12$ segments. This is because FEKO makes use of more complex basis functions and optimization techniques which give a more accurate answer for the same number of segments. An even number of segments are used for the FEKO calculations, assuming that there would be $N - 1$ basis functions such as for the triangular and sinusoidal basis functions.

Figure 4.6 (b) shows how the result becomes more accurate for a larger number of segments. A larger number of stair step pulses make the distribution look more sinusoidal. The maximum value of 9.723 [mA] achieved with $N = 21$ is also only 2.2% below the value calculated by FEKO using $N = 22$ segments. This is much better than the 31.8% difference with $N = 12$.

The next section compares the current distributions obtained for the $\lambda/2$ dipole antenna using triangular basis functions.

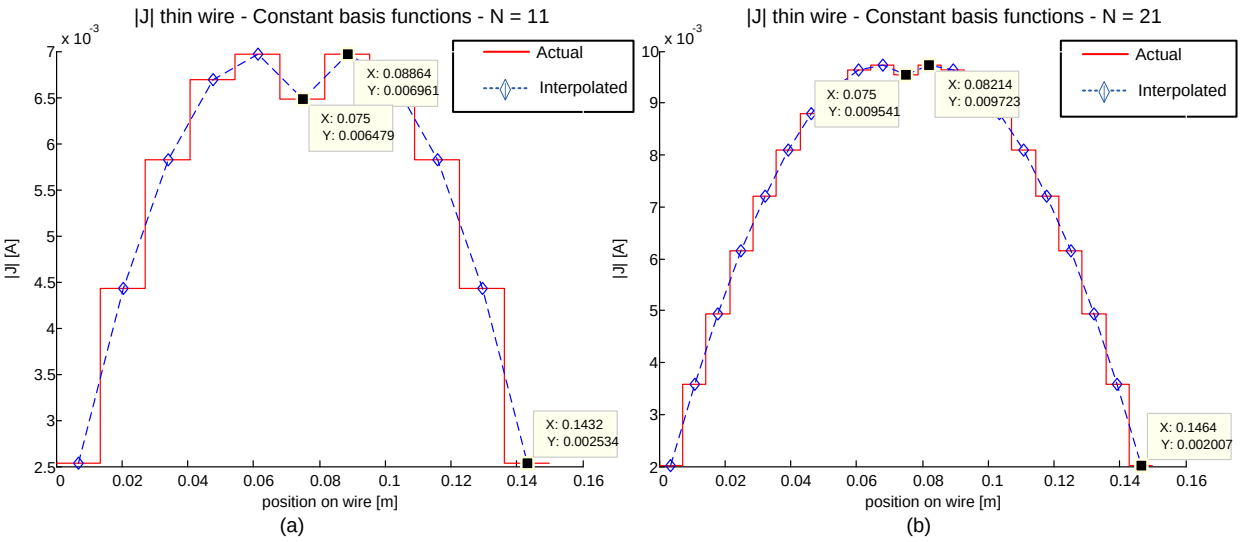

Figure 4.6: Current on a $\lambda/2$ thin wire dipole antenna calculated with the Method of Moments using constant basis functions: f = 1 [GHz] (a) $N = 11$ (b) $N = 21$

4.4.2 Triangular Basis Functions

The magnitude of the current density distribution for the thin wire dipole antenna calculated using triangular basis functions is shown in Figure 4.7. Values of $N = 12$ and $N = 22$ are used since there will then be $N - 1 = 11$ and $N - 1 = 21$ basis functions to represent the current density as for the constant basis functions. The basis functions which have been multiplied by their respective current coefficients are plotted in color. The lines which join the peaks of consecutive basis functions are the sum of the half basis functions which represent the current density on the specific segment, and is not linear interpolation as in Figure 4.6.

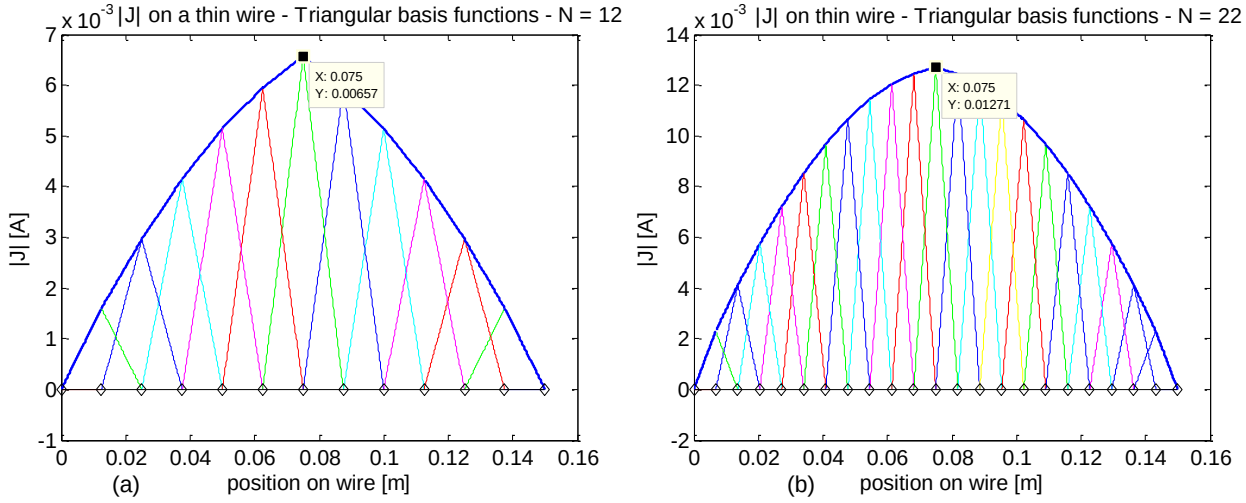

Figure 4.7: Current on a $\lambda/2$ thin wire dipole antenna calculated with the Method of Moments using triangular basis functions: f = 1 [GHz] (a) $N = 12$ (b) $N = 22$

The current density distributions in Figure 4.7 have a closer resemblance to the theoretically predicted half-wave sinusoid than the results obtained with the stair step basis functions, with the accuracy increasing as N is increased.

A maximum value of 6.57 [mA] is obtained with $N = 12$ segments and the curve appears more like a sinusoid than the stair step current distribution represented by the constant basis functions. However, the dip which occurs after the peak in the FEKO results in Figure 4.5 is not seen. As before, greater accuracy is achieved with more segments, indicated by the current density distribution in Figure 4.7 (b) for $N = 22$. However, the deviation between the maximum values is still 27.9% for $N = 22$ and is only slightly better than the 33.9% with $N = 12$ segments.

4.4.3 Sinusoidal Basis Functions

Sinusoidal basis functions result in good accuracy, even for low values of N. Figures 4.6, 4.7 and 4.8 clearly show that the results obtained with the sinusoidal basis functions compare well to those of FEKO. The current density distribution appears more sinusoidal than with the other basis functions. There is only a 7% deviation from the maximum value of the FEKO for $N = 22$ segments.

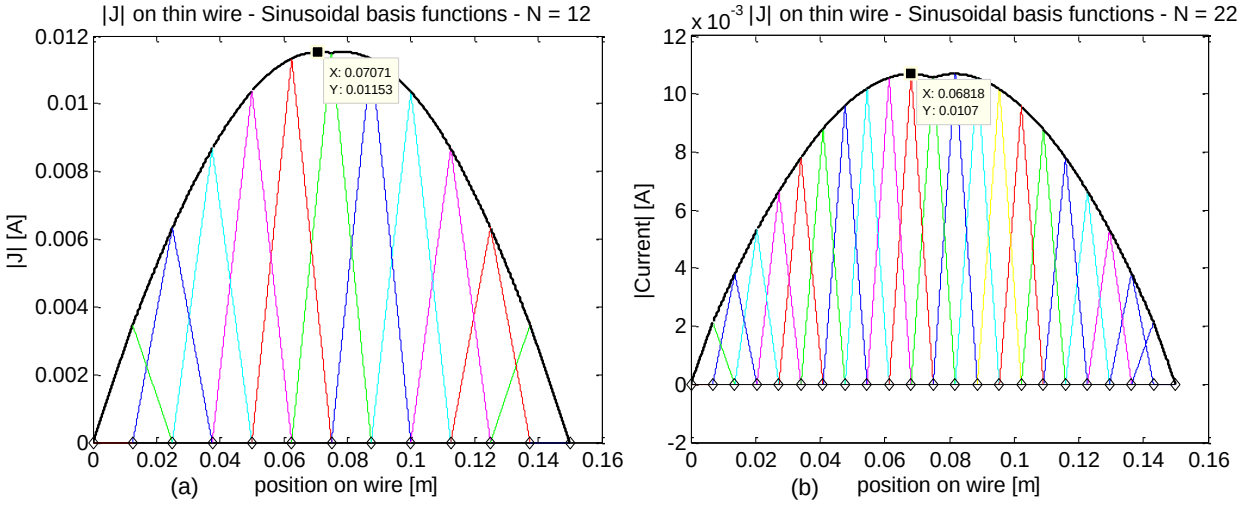

Figure 4.8: Current on a $\lambda/2$ thin wire dipole antenna calculated with the method of moments using sinusoidal basis functions: f = 1 [GHz] (a) $N = 12$ (b) $N = 22$

4.4.4 Conclusion

The accuracy achieved with the various basis functions can be compared in more detail by plotting the difference between the FEKO current distributions and the distributions calculated using the various basis functions. However, the results are sufficient for the purpose of illustrating the

concept of the MoM. The principles discussed in this chapter are extended in Chapter 5 to solve for the current density distributions on triangulated surfaces.

Chapter 5

Method of Moments Formulation for Tapered Waveguides

This chapter discusses the triangular patch MoM, which is used to calculate the current density on the surface of a conductor by reducing the Electric Field Integral Equation (EFIE) to a set of linear simultaneous equations. An in-house MoM solver is developed in MATLAB to calculate the surface current density and electric farfields of typical TEM horn antennas, such as those in Chapter 3. Although the MoM algorithm is general, the in-house code assumes symmetry which is specific to TEM horn antennas. A Mesher, which calculates the geometrical data required for the MoM, is also developed to triangulate surfaces with properties typical of TEM horns.

5.1 Theory

The theory used to implement the triangular patch MoM is provided in the following subsections. As for the case of a simple thin wire, the current on the surface of a conductor will be approximated as the sum of a number of basis functions multiplied with their respective weighting coefficients.

5.1.1 Triangular Patch Method of Moments

The Method of Moments assumes that a conductor can be replaced by a number of equivalent surface current densities [12]. The method introduced by Rao et al [4] requires the surface of a conductor to be discretized into triangular patches, and makes use of special RWG (Rao-Wilton-Glisson) basis functions to approximate the current density in each triangle. Once the surface of a conductor has been triangulated in terms of appropriate faces, vertices, non-boundary edges and boundary edges such as those shown in Figure 5.1, the basis functions which will approximate the current can be defined [4].

Every non-boundary edge n on a surface S is associated with a basis function $\mathbf{f}_n$ which is zero

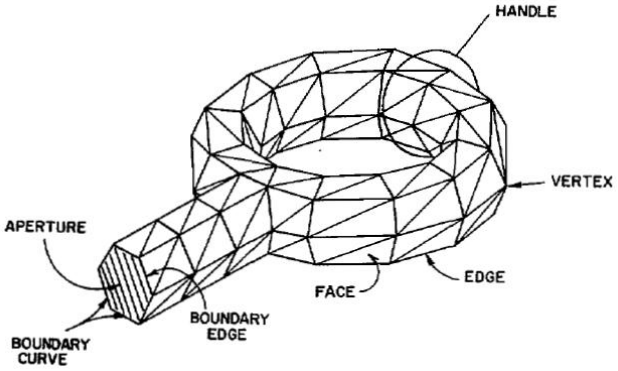

Figure 5.1: An arbitrary surface modelled by triangular patches [4].

everywhere on S, except in the two triangles sharing edge n [4]. Figure 5.2 shows triangles T_n^+ and T_n^- which are associated with the n^{th} non-boundary edge. The + and − superscripts refer to the reference direction of positive current flow from T_n^+ to T_n^- for the n^{th} edge. Any point inside triangle T_n^+ can be described either in terms of the position vector $\mathbf{r}$, defined with respect to global reference point O, or in terms of $\boldsymbol{\rho}_n^+$, which is defined with respect to the free vertex of T_n^+ [4].

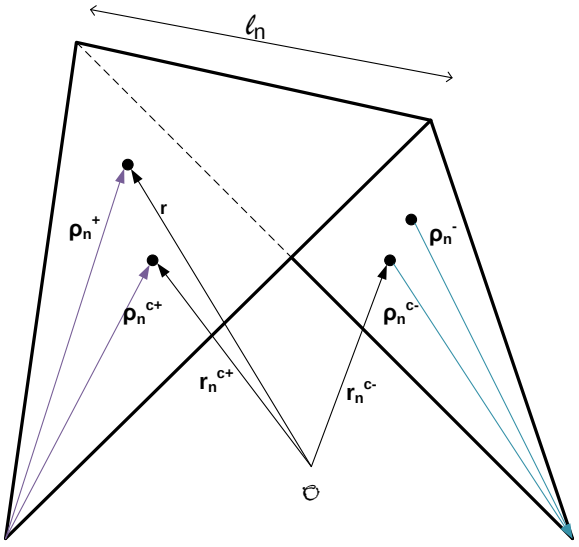

Figure 5.2: Triangle pair associated with interior edge n

The vector basis function associated with the n^{th} edge is defined as [4],

$$\mathbf{f}_n(\mathbf{r}) = \begin{cases} \frac{l_n}{2A_n^+}\boldsymbol{\rho}_n^+ & \text{if } \mathbf{r} \text{ in } T_n^+ \\ \frac{l_n}{2A_n^-}\rho_n^- & \text{if } \mathbf{r} \text{ in } T_n^- \\ 0 & \text{otherwise} \end{cases} \tag{5.1}$$

where l_n is the length of edge n and $A_n^\pm$ is the area of triangle $T_n^\pm$. This type of basis function was introduced by Rao et al in [4] and has the following properties which make it suitable to

approximately represent the surface current:

1. The current has no component normal to any boundary of the surface formed by the triangle pair, except at the common edge. Therefore, no line charge exists at along this boundary. [4]

2. The component of current normal to the n^{th} edge is constant and continuous across the edge. $A_n^{\pm}/l_n$ is the height of triangle $T_n^{\pm}$ and normalises $\mathbf{f_n}(\mathbf{r})$ so that the flux density normal to edge n is unity. This ensures continuity of the current normal to the edge. Together, properties 1 and 2 imply that all edges of $T_n^{\pm}$ are free of line charges [4].

3. The surface divergence of $\mathbf{f}_n$ is defined as,

$$\nabla_{\mathbf{s}} \cdot \mathbf{f}_n = \begin{cases} \frac{l_n}{A_n^+} & \mathbf{r} \text{ in } T_n^+ \\ \frac{-l_n}{A_n^-} & \mathbf{r} \text{ in } T_n^- \\ 0 & \text{otherwise} \end{cases} \tag{5.2}$$

   and is proportional to the surface charge density associated with the basis function. Therefore, the charge density in each triangle is constant and the total charge associated with the triangle pair T_n^+ and T_n^- is equal to zero. The basis functions for the charge have the form of pulse doublets [4].

The current on surface S is approximated in [4] as,

$$\mathbf{J} = \sum_{n=1}^{N} I_n \mathbf{f}_n(\mathbf{r}) \tag{5.3}$$

where N is the number of non-boundary edges. The coefficients I_n are scalar quantities and the basis functions $\mathbf{f}_n$ are vectors representing current direction. Since a basis function $\mathbf{f}_n$ is associated with each non-boundary edge n, the current density has the following properties [4]:

- A maximum of three basis functions will have non-zero values within each triangle on S.
- Only $\mathbf{f}_n$ will have a current component normal to edge n since all other currents in adjacent faces are parallel to the edge.
- Since the normal component of $\mathbf{f}_n$ at edge n is equal to 1, the coefficient I_n may be taken as the normal component of current density flowing past edge n.
- The basis functions in each triangle are independent since the normal component of current across edge n (I_n) is an independent quantity.
- Contributions from surface boundary edges are not defined or included for Equation 5.3 because the normal components of currents on opposite sides of the surface cancel due to current continuity.

Testing Procedure Galerkin's method of weighted residuals [12] is used as a testing procedure to obtain the matrix equation necessary to solve for the coefficients I_n. For an equation such as,

$$g = \int f dS \tag{5.4}$$

where $f = \sum_{n=1}^{N} a_n h_n$, the $N \times N$ linear system can be obtained by applying point-matching at N test points. However, by defining the residual as $R = \sum_{n=1}^{N} a_n h_n - g$, (or the difference between the actual solution and the approximate solution) the average value of R over the domain of the solution can be calculated and set to zero instead of forcing the equation to zero at N points. This can be achieved by multiplying the residual by a weighting function $w = \sum_{m=1}^{M} w_m$ and integrating over the domain, as shown in Equation 5.5.

$$\int R \sum_{m=1}^{M} w_m dS = \int \sum_{m=1}^{M} w_m \int \sum_{n=1}^{N} a_n h_n - \int \sum_{m=1}^{M} w_m g = 0 \tag{5.5}$$

This can be expressed as the inner product,

$$< w_m, \int a_n h_n >=< w_m, g > \tag{5.6}$$

and results in a matrix equation,

$$\{V\} = [Z]\{I\} \tag{5.7}$$

where $Z_{mn} =< w_m, \int h_n >$, $V_m =< w_m, g >$ and $I_n = a_n$.

In the Galerkin formulation, the weighting functions have the same form as the basis functions [12] and testing the EFIE with basis functions $\mathbf{f}_m$ yields,

$$< \mathbf{E}_i, \mathbf{f_m} >= j\omega < \mathbf{A}, \mathbf{f}_m > + < \nabla\Phi, \mathbf{f}_m > \tag{5.8}$$

By using vector identities, the last term in Equation 5.8 can be rewritten as,

$$< \nabla\Phi, \mathbf{f}_m >= -\int_S \Phi \nabla_s \cdot \mathbf{f}_m dS \tag{5.9}$$

and by using Equation 5.2 it can be written an approximated as

$$\int_S \Phi \nabla_s \cdot \mathbf{f}_m dS = l_m \left(\frac{1}{A_m^+} \int_{T_m^+} \Phi dS - \frac{1}{A_m^-} \int_{T_m^-} \Phi dS \right) \cong l_m [\Phi(\mathbf{r}_m^{c+}) - \Phi(r_m^{c-})] \tag{5.10}$$

Equation 5.10 approximates the average of Φ over each triangle as the value of Φ at the triangle centroid. If similar approximations are made for the vector potential and incident electric field, Equation 5.8 becomes,

$$\begin{aligned} & l_m \left[\mathbf{E}^i(\mathbf{r}_m^{c+}) \cdot \tfrac{\rho_m^{c+}}{2} + \mathbf{E}^i(\mathbf{r}_m^{c-}) \cdot \tfrac{\rho_m^{c-}}{2} \right] \\ & = j\omega l_m \left[\mathbf{A}(\mathbf{r}_m^{c+}) \cdot \tfrac{\rho_m^{c+}}{2} + \mathbf{A}(\mathbf{r}_m^{c-}) \cdot \tfrac{\rho_m^{c-}}{2} \right] + l_m \left[\mathbf{\Phi}(\mathbf{r}_m^{c-}) - \mathbf{\Phi}(\mathbf{r}_m^{c+}) \right] \end{aligned} \tag{5.11}$$

and is the equation enforced at each triangle edge, $m = 1, 2, ...N$ [4].

Matrix Equation An $N \times N$ system of linear equations is obtained if Equation 5.3 is substituted into Equation 5.11. The resulting system can be written in the matrix form,

$$[Z][I] = [V] \tag{5.12}$$

where $[Z] = [Z_{mn}]$ is an $N \times N$ matrix and $I = [I_n]$ and $[V] = [V_m]$ are column vectors with N entries. The elements of $[Z]$ and $[V]$ are given by,

$$Z_{mn} = j\omega l_m \left[\mathbf{A}(\mathbf{r}_m^{c+}) \cdot \frac{\rho_m^{c+}}{2} + \mathbf{A}(\mathbf{r}_m^{c-}) \cdot \frac{\rho_m^{c-}}{2} \right] + l_m \left[\mathbf{\Phi}(\mathbf{r}_m^{c-}) - \mathbf{\Phi}(\mathbf{r}_m^{c+}) \right] \tag{5.13}$$

and

$$V_m = l_m \left(\mathbf{E}_m^{+} \cdot \frac{\rho_m^{c+}}{2} + \mathbf{E}_m^{-} \cdot \frac{\rho_m^{c-}}{2} \right) \tag{5.14}$$

where,

$$\mathbf{A}_{mn}^{\pm} = \frac{\mu}{4\pi} \int_S \mathbf{f}_n(\mathbf{r}') \frac{e^{-jkR_m^{\pm}}}{R_m^{\pm}} dS', \tag{5.15}$$

$$\mathbf{\Phi}_{mn}^{\pm} = \frac{-1}{4\pi j\omega\epsilon} \int_S \nabla_S' \cdot \mathbf{f}_n(\mathbf{r}') \frac{e^{-jkR_m^{\pm}}}{R_m^{\pm}} dS', \tag{5.16}$$

$$R_m^{\pm} = |\mathbf{r}_m^{c\pm} - \mathbf{r}'| \tag{5.17}$$

and

$$\mathbf{E}_m^{\pm} = \mathbf{E}^i(\mathbf{r}_m^{c\pm}). \tag{5.18}$$

It is important to clarify that m refers to the *observation* edge and triangle pair $T_m^{\pm}$ and n refers to the *source* edge and triangle pair $T_n^{\pm}$. The indices $\pm$ refer to the positive or negative face of the triangle pair. Figure 5.3 shows such an arbitrary source and observation triangle pair.

To illustrate the concept clearly, the expression for A_{mn}^{+} is given as an example:

$$A_{mn}^{+} = \frac{\mu}{4\pi} \int_{T_n^{+}} \mathbf{f}_n^{+}(\mathbf{r}'^{+}) \frac{e^{-jkR^{pp}}}{R^{pp}} dS' + \frac{\mu}{4\pi} \int_{T_n^{-}} \mathbf{f}_n^{-}(\mathbf{r}'^{-}) \frac{e^{-jkR^{pn}}}{R^{pn}} dS' \tag{5.19}$$

The rest of the terms required for Z_{mn} can be calculated in a similar manner and the matrix equation can be solved for the values I_n.

Since analytical integration is difficult and time consuming, numerical integration is used to approximate the integrals in Equations 5.15 and 5.16. The next section provides the necessary information regarding numerical integration.

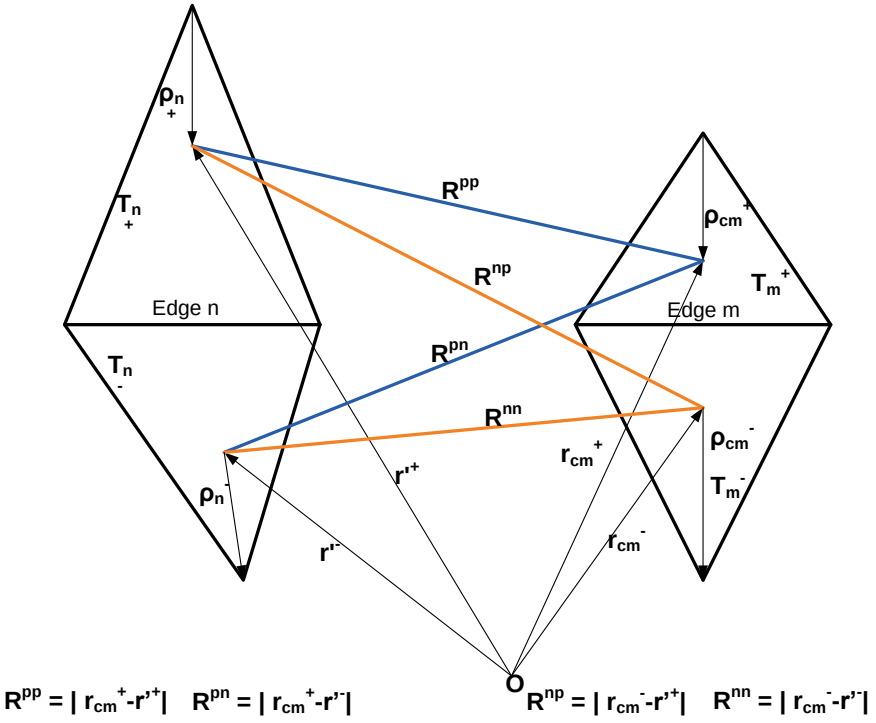

Figure 5.3: Arbitrary source (n) and observation triangle (m) pairs

5.1.2 Numerical Integration

Numerical integration is used to approximate the integrals in Equations 5.15 and 5.16 as their analytical solutions are very complex and time consuming. Simplex coordinates are convenient for defining one set of sample points for numerical integration over triangles.

Simplex Coordinates Simplex coordinates are also known as Area or Barycentric coordinates. The triangle shown in Figure 5.4 is an equilateral triangle with side lengths equal to 1 unit. The lines drawn from each vertex to any point $\mathbf{r}$ inside the triangle divides the total area A_T into three areas. Areas A_1, A_2 and A_3 each account for a fraction of the total triangle area. These fractions are defined as the simplex coordinates of a triangle,

$$\lambda_1 = \frac{A_1}{A_T} \qquad \lambda_2 = \frac{A_2}{A_T} \qquad \lambda_3 = \frac{A_3}{A_T} \tag{5.20}$$

where,

$$\lambda_1 + \lambda_2 + \lambda_3 = 1 \tag{5.21}$$

The three vertices of the triangle can be described in terms of either Cartesian or Simplex coordinates,

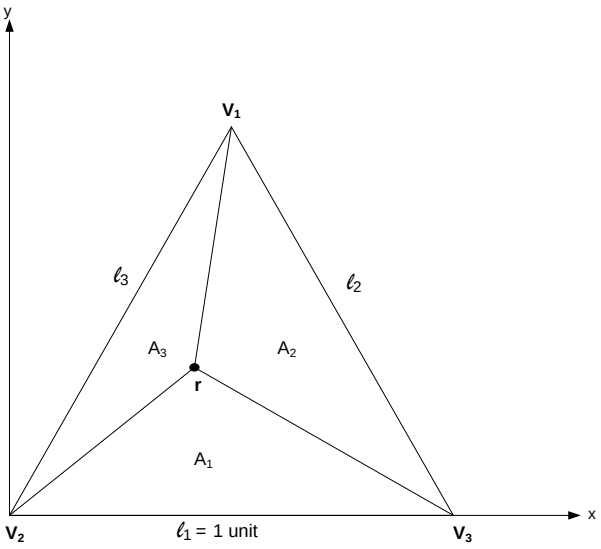

Figure 5.4: Equilateral triangle and relevant parameters used to define the Simplex coordinate system

$$\begin{aligned} \mathbf{v}_1(x,y) &= (0.5,\ \sqrt{3}/2) & \mathbf{v}_1(\lambda_1,\lambda_2,\lambda_3) &= (1,0,0) \\ \mathbf{v}_2(x,y) &= (0,0) & \mathbf{v}_2(\lambda_1,\lambda_2,\lambda_3) &= (0,1,0) \\ \mathbf{v}_3(x,y) &= (1,0) & \mathbf{v}_3(\lambda_1,\lambda_2,\lambda_3) &= (0,0,1) \end{aligned}$$

Any point $\mathbf{r}$ inside the triangle can be expressed in terms of the three vertices [4]:

$$\mathbf{r} = \lambda_1\mathbf{v}_1 + \lambda_2\mathbf{v}_2 + \lambda_3\mathbf{v}_3 \tag{5.22}$$

For example, the centroid of triangle T divides it into three equal areas so that $\mathbf{r}_c = (\frac{1}{3}, \frac{1}{3}, \frac{1}{3})$ in simplex coordinates. Equation 5.22 is used to convert $\mathbf{r}$ to Cartesian coordinates,

$$\mathbf{r}_c = \frac{1}{3}(0.5,\ \sqrt{3}/2) + \frac{1}{3}(0,0) + \frac{1}{3}(1,0) = (0.5,\ \sqrt{3}/6) \tag{5.23}$$

Quadrature Integration Quadrature integration is a numerical integration technique which approximates an integral by a summation of integrand samples which are multiplied with a set of weighting coefficients [5]. Since Equations 5.15 and 5.16 involve integrations over sets of triangles on a surface S, it is more convenient to choose the sample points in terms of a local coordinate system and convert back to Cartesian coordinates. This is done so that one set of sample points can be defined in simplex coordinates for all triangles. This will make the sample points in all triangle symmetric and avoids variations caused by element vertex reordering [5].

Integration over a triangular domain takes the form,

$$\int\int f(\lambda_1,\lambda_2,\lambda_3)dA = A\sum_{i=1}^{N} w_i f(\lambda_{1i},\lambda_{2i},\lambda_{3i}) \tag{5.24}$$

where A is the area of the triangle and N is the total number of sample or integrand points [5]. The method relies on the assumption that the function being integrated can be approximated as a polynomial of degree p and can be evaluated at $N = P + 1$ sample points. To solve the tested EFIE using quadrature integration the integrands in Equations 5.15 and 5.16 are approximated as polynomials of degree 2 under the assumption that $\mathbf{r}_c^m >> \mathbf{r}'$

[5] and [6] describe the procedure used to determine the following set of the sample points and the corresponding weights:

$$\{(\lambda_1, \lambda_2, \lambda_3)\} = \{(\eta, \zeta, \zeta), (\zeta, \eta, \zeta), (\zeta, \zeta, \eta)\} \tag{5.25}$$

Values of $\eta = \frac{2}{3}$, $\zeta = \frac{1}{6}$ are determined in [5] as well as $w_i = \frac{1}{3}$ for all three points. Using this set of simplex coordinates, the integrals in Equations 5.15 and 5.16 can be simplified to weighted sums of the integrands evaluated at the chosen sample points.

The MoM can now be applied using all the information provided in this section. The rest of this chapter discusses the implementation of a meshing algorithm and code which divides a surface into appropriate triangles, edges and vertices as well as the development of code to solve for the current distribution on PEC surface using the triangular patch method of moments.

5.1.3 Symmetry

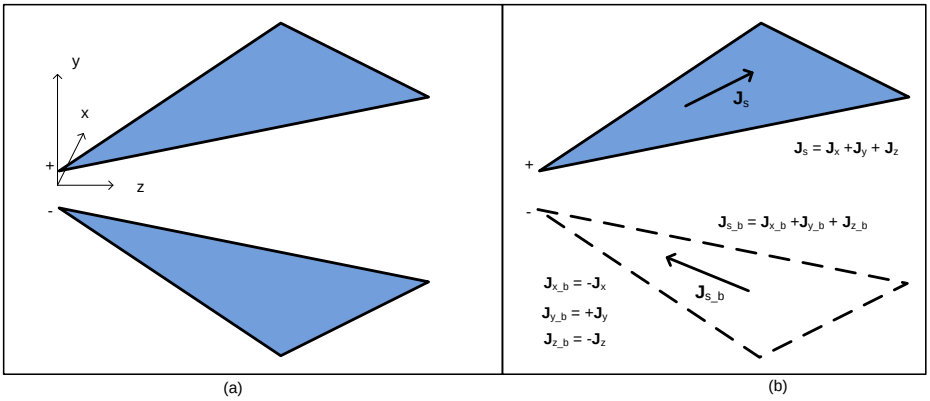

Figure 5.5: (a) Basic 2 plate TEM horn (b) Surface current densities on top and bottom plate

The electric symmetry of TEM horn antennas is used to reduce the number of calculations required to solve for the unknown current coefficients with the in-house MoM solver. Figure 5.5 (a) shows a basic TEM horn with a differential feed. The current density (and thus current coefficients) on the top and bottom plates are related as shown in Figure 5.5 (b) or as follows:

- $J_{x-b} = -J_x$
- $J_{y-b} = +J_y$

- $J_{z-b} = -J_z$

Therefore, if there are a total of N non-boundary edges (current coefficients) for two plates, there are only $N/2$ unknowns which need to be solved for. Thus, only the $N/2$ observation triangle pairs on the top plate are required and $[V_m]$ in Equation 5.12 is an $(\frac{N}{2} \times 1)$ matrix. The N source triangle pairs are accounted for using symmetry. Each element of the $[Z_{mn}]$ matrix is calculated to include the effect of a source on the top plate as well as its symmetrical counterpart on the bottom plate and the matrix size is reduced to $(\frac{N}{2} \times \frac{N}{2})$.

Reducing the size of the matrix elements reduces the simulation time of the in-house solver as it makes use of a nested for-loop with the outer and inner loop having a size equal to the number of unknowns. The code is implemented in MATLAB which is more suited to vector operations and does not handle for loops efficiently. Therefore, reducing the size of the loops is important in reducing the simulation time, especially for a large number of unknowns.

5.1.4 Calculating the Farfield

The farfields of an antenna can be calculated from the near-fields at the antenna aperture, or directly from the surface current density. It is very difficult and time consuming to calculate the near-field analytically. Therefore, the farfield is calculated directly from the surface current using approximations which are discussed in the following paragraphs.

The electric field is calculated using Equation 4.7 which is shown below in terms of the magnetic vector potential $\mathbf{A}$.

$$E(\mathbf{r}) = \frac{-1}{j\omega\mu\epsilon}\Big(k^2\mathbf{A}(\mathbf{r}) + \nabla^2\mathbf{A}(\mathbf{r})\Big) \tag{5.26}$$

Once the current coefficients I_n are known, the magnetic vector potential is easily calculated from the surface current density $\mathbf{J}$,

$$\mathbf{A}(\mathbf{r}) = \frac{\mu}{4\pi}\int_S \mathbf{J}\frac{e^{-jk|\mathbf{r}-\mathbf{r}'|}}{|\mathbf{r}-\mathbf{r}'|}ds' \tag{5.27}$$

Since the fields radiated by antennas of finite dimensions are spherical waves [7], the magnetic vector potential is expressed as,

$$\mathbf{A} = \hat{i}_r A_r(r,\theta,\phi) + \hat{i}_\theta A_\theta(r,\theta,\phi) + \hat{i}_\phi A_\phi(r,\theta,\phi) \tag{5.28}$$

The presence of the second derivative in Equation 5.26 results in complex calculations which can be eliminated by using the following farfield approximations [7]:

1. The observation point is assumed to be in the farfield (or Fraunhofer) region so that $|\mathbf{r} - \mathbf{r}'|$ is very large [7]. The second order derivative of $\mathbf{A}$ in Equation 5.26 will cause the denominator of resulting terms to become so large that their contribution to the electric field can

be completely ignored. The second derivative of **A** also conveniently cancels out the radial component produced by the first term in Equation 5.26. Therefore, the magnitude of E_r is negligible compared to that of E_θ and E_ϕ. So, in the farfield,

$$E_r \approxeq 0 \tag{5.29}$$

$$E_\theta \approxeq -j\omega A_\theta \tag{5.30}$$

$$E_\phi \approxeq -j\omega A_\phi \tag{5.31}$$

2. Furthermore, since $r \gg r'$ the effect of $\mathbf{r}'$ can be ignored in the magnitude term ($\frac{1}{|\mathbf{r}-\mathbf{r}'|}$) of the Green's function [7]. In other words, $|\mathbf{r} - \mathbf{r}'| \approxeq |\mathbf{r}| = r$. The denominator is now independent of the integration variables and can be taken out of the integral so that we are left with,

$$\mathbf{A} \approxeq \frac{\mu}{4\pi r}\int_S \mathbf{J}_s e^{-jk|\mathbf{r}-\mathbf{r}'|}ds' \tag{5.32}$$

3. A further simplification can be made for phase variations by approximating R as,

$$|\mathbf{r} - \mathbf{r}'| \approxeq r - r'\cos(\psi) \tag{5.33}$$

The derivation of this approximation is done in [7] and is not repeated here. The angle ψ is defined as the angle between the vectors $\mathbf{r}$ and $\mathbf{r}'$.

Finally, the magnetic vector potential in the farfield is approximated as,

$$\mathbf{A} \approxeq \frac{\mu e^{-jkr}}{4\pi r}\mathbf{N} \tag{5.34}$$

where,

$$\mathbf{N} = \int_S \mathbf{J}_s e^{jkr'\cos(\psi)}ds' \tag{5.35}$$

Typical farfield plots show the field calculated using **N** instead of **A**, as it is clear that the magnitude of the field will decrease linearly as r increases and that the e^{-jkr} subtracts a linear phase. If necessary, the exact values of the fields can be calculated for some distance $r = r_0$ from the antenna aperture by multiplying the answer by the constants in front of **N** in Equation 5.34.

5.1.5 Differential Feed Method

A differential feed is used to excite all electrically symmetric antennas analysed with the in-house code. The method described in this section is adapted from [14]. Figure 5.6 shows a simple flat plate (represents a parallel plate waveguide) which has been discretized into triangles. As symmetry is used to account for the sources on the bottom plate, only one plate is shown and the port (source V_s and impedance Z_g) is connected to ground.

The edges a and b are boundary edges and to ensure current continuity, special half-basis functions must be defined to account for the current density flowing across these edges. The half-basis functions are the same as those for the N_1 non-boundary edges, except that they are non-zero in only one triangle instead of two. Depending on the convention of current flow and triangle definitions specified by the developer, this will be either in T_n^+ or T_n^- and the respective half-basis function is chosen from Equation 5.37. Therefore, the half basis functions will be either,

$$\mathbf{f}_n(\mathbf{r}) = \begin{cases} \frac{l_n}{2A_n^+}\boldsymbol{\rho}_n^+ & \text{if } \mathbf{r} \text{ in } T_n^+ \\ 0 & \text{otherwise} \end{cases} \tag{5.36}$$

or,

$$\mathbf{f}_n(\mathbf{r}) = \begin{cases} \frac{l_n}{2A_n^-}\rho_n^- & \text{if } \mathbf{r} \text{ in } T_n^- \\ 0 & \text{otherwise} \end{cases} \tag{5.37}$$

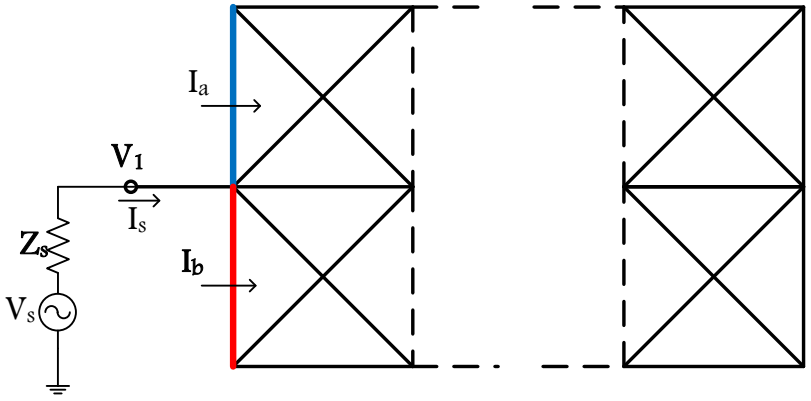

Figure 5.6: Differential feed excitation port

In general there will now be $N_1 + N_p$ current coefficients to solve for using the matrix equation, where N_p is the number of port edges. The effect of the half basis functions is accounted for in exactly the same way as the others and contribute to the elements of $[Z_{mn}]$. However, the effect of the source voltage and port impedance need to be taken into account.

To clarify, I_a and I_b are the current density coefficients so that the total current across those edges are the coefficients multiplied by the edge length. Therefore,

$$I_s = I_a l_a + I_b l_b \tag{5.38}$$

Assuming a delta gap source model [14] and testing the EFIE as described above, it can be shown that

$$E_m =< \mathbf{E}_i, \mathbf{f_m} >= V_m l_m \tag{5.39}$$

where E_i is a voltage gap source with a magnitude of $V_m = V_1$ and,

$$V_1 = V_s - Z_s I_s \tag{5.40}$$

Therefore,

$$E_a = V_1 l_a = (V_s - Z_s(I_a l_a + I_b l_b))l_a \tag{5.41}$$

and

$$E_b = V_1 l_b = (V_s - Z_s(I_a l_a + I_b l_b))l_b \tag{5.42}$$

If the matrix equation is $[Z_{mn}][I_n] = [E_m]$, with E_m given by Equations 5.41 and 5.42 at edges a and b respectively and zero elsewhere, we can write a new matrix equation in terms of $[I_n]$ as,

$$\left([Z_{mn}] + \begin{pmatrix} 0 & 0 & \dots & 0 & 0 \\ 0 & 0 & \dots & 0 & 0 \\ \vdots & \vdots & \ddots & 0 & 0 \\ 0 & 0 & \dots & 0 & 0 \\ 0 & \dots & 0 & l_a l_a Z_s & l_a l_b Z_s \\ 0 & \dots & 0 & l_b l_a Z_s & l_b l_b Z_s \end{pmatrix} \right) \begin{pmatrix} I_1 \\ I_2 \\ \vdots \\ I_{N1} \\ I_a \\ I_b \end{pmatrix} = \begin{pmatrix} 0 \\ 0 \\ \vdots \\ 0 \\ l_a V_s \\ l_b V_s \end{pmatrix}$$

5.2 Design and Implementation

The code for the in-house MoM solver was developed in MATLAB in the following stages:

1. A *mesher* is developed to triangulate the surfaces of conductors as required by the triangular patch MoM. The mesher stores data such as vertices which define triangles, non-boundary edges and triangle centroids etc. and passes it to the MoM solver with a function call.

2. The Method of Moments algorithm is implemented and uses the data received from the mesher to solve for the surface current density coefficients.

3. Finally, code is developed to calculate the farfield of an antenna from the surface current density as calculated with the in-house MoM solver. The final output of the in-house solver is a 3D plot of the magnitude of the electric field (using **N**) as well as its θ and ϕ components.

Since the Method of Moments and the numerical techniques related to its implementation are discussed in detail in the previous sections, the development of the code is not discussed. However, the algorithm used in the mesher is self-designed and is discussed below.

5.2.1 Mesher

This section provides a brief description of the meshing algorithm and illustrates the concept using a simple example. The purpose of the discussion is to provide insight to the reader without delving into too much detail.

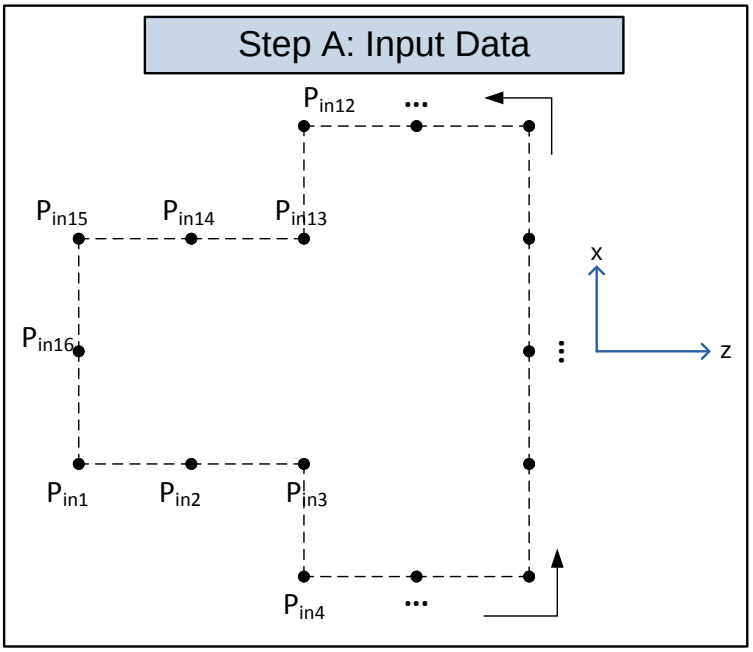

Figure 5.7: Example of a surface defined by input points P_{in_i} entered by the user in a consecutive manner

Step A: Input Data The user inputs a set of (x,y,z) coordinates that define the outline or boundary of the surface which is to be discretized. The data is entered in the form of a matrix,

$$\left([P_{in}] = \begin{pmatrix} x_1 & y_1 & z_1 \\ x_2 & y_2 & z_2 \\ \vdots & \vdots & \vdots \\ x_{I-1} & y_{I-1} & z_{I-1} \\ x_I & y_I & z_I \end{pmatrix} \right)$$

where I is the total number of input points.

The input points must be entered in a consecutive manner, from one end of the structure to the other and back again as shown for the example surface in Figure 5.7. This is required so that consecutive points, which will be joined with straight line segments, are known.

Step B: Mesh Refinement After entering the input data, the user may choose to specify the value of the mesh refinement factor $\alpha \geq 0$. The default value of the mesh refinement factor is 0. If $\alpha = k$, where $k > 0$ is a constant, the mesher creates k additional points between every two consecutive input points. These points are equally spaced and calculated using the difference between two consecutive points.

The data is rearranged into a new matrix $[P]$ which includes the original input points as well as the additional data points, again in a consecutive manner similar to that shown in Figure 5.7.

Figure 5.8 shows how 1 additional boundary point is created between every two consecutive input points defined in Figure 5.7 for $\alpha = 1$.

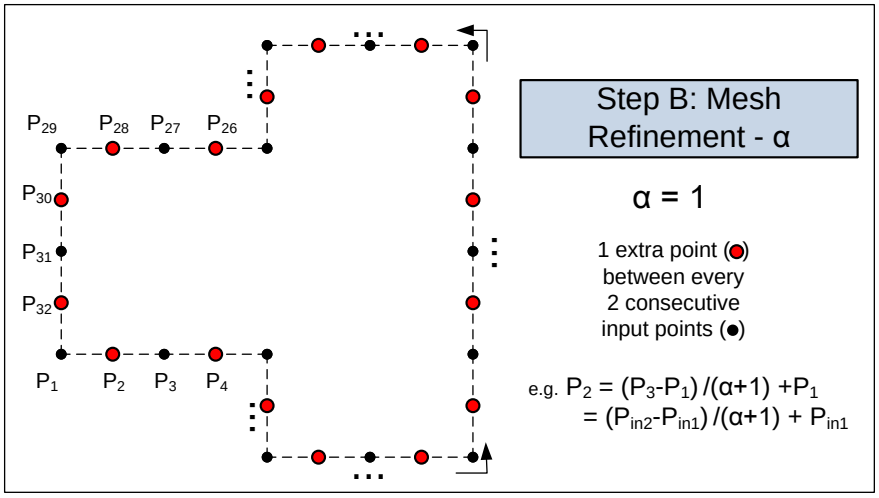

Figure 5.8: Calculate $\alpha = 1$ additional points (red points) between every two consecutive input points and define a new matrix [**P**] that defines the outline of the surface in terms of old and new data points

Step C: Filling in the Grid After completing Step B, the mesher fills in points inside the boundaries of the structure as shown in Figure 5.9. These points are positioned at the intersections of the indicated grid-lines (including boundary grid-lines) which are defined using the coordinates in matrix $[P]$.

Step D: Rectangle Midpoints One additional point is defined at the center of each rectangle (defined by four grid points) as shown in Figure 5.9. Diagonal grid lines are used to indicate the triangle definitions.

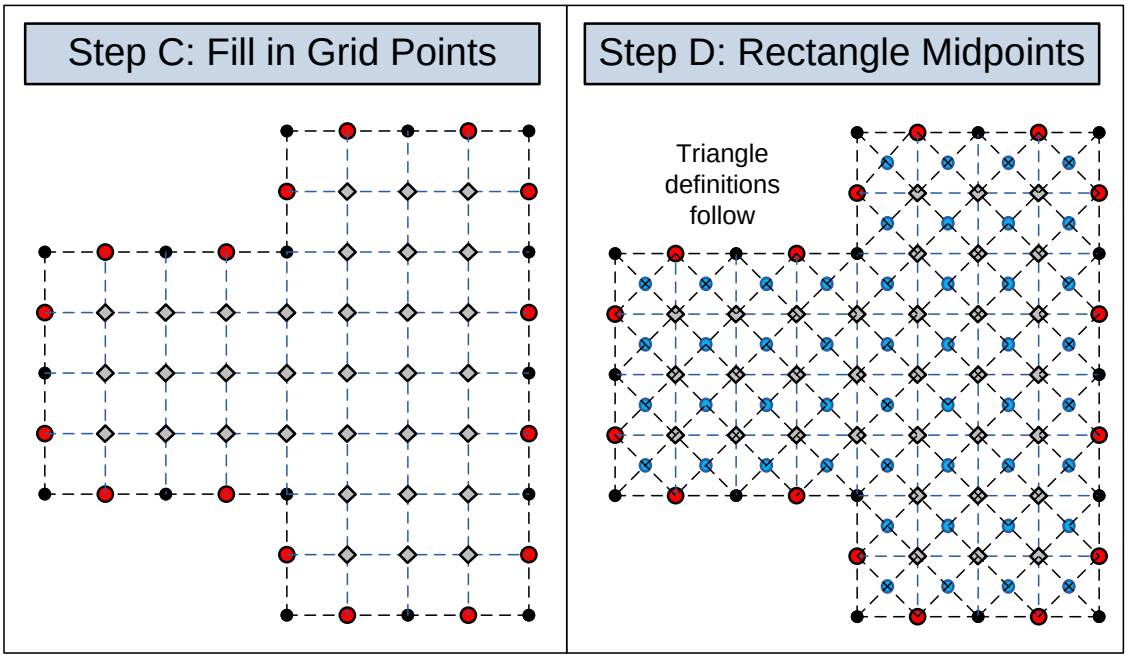

Figure 5.9: Mesher: Steps D and E

Step E: Data Storage After filling in all grid points and storing the data in a matrix, it is reorganised as follows:

- A matrix $[\mathbf{T}] = [\mathbf{v}_1 \quad \mathbf{v}_2 \quad \mathbf{v}_3]$ stores the (x,y,z) coordinates of the three vertices v_i $(i = 1, 2, 3)$ of each triangle so that,

$$[v_i] = \begin{pmatrix} x_{T(1)v(i)} & y_{T(1)v(i)} & z_{T(1)v(i)} \\ x_{T(2)v(i)} & y_{T(2)v(i)} & z_{T(2)v(i)} \\ \vdots & \vdots & \vdots \\ x_{T(t-1)v(i)} & y_{T(t-1)v(i)} & z_{T(t-1)v(i)} \\ x_{T(t)v(i)} & y_{T(t)v(i)} & z_{T(t)v(i)} \end{pmatrix}$$

  For example , $x_{T(1)v(i)}$ refers to the **x-coordinate** of the **i$^{\text{th}}$ vertex** of **triangle 1**, where t is the total number of triangles. The first row of the matrix [**T**] would define the vertices of the first triangle for example.

- N Non-boundary edges (defined by two triangle vertices) and the indices of their respective triangle pairs are stored in a similar manner as [**T**], so that [**Edges**] = $[\mathbf{v}_a \quad \mathbf{v}_b \quad \mathbf{T}^+ \quad \mathbf{T}^-]$. The first row refers to the first non-boundary edge, whereas the n^th row refers to non-boundary edge n.

- The mesher also calculates and stores the coordinates of the triangle centroids, as well as the area of each triangle.

The triangles and edges are numbered so that the direction of positive current flow is known. Various testing procedures and algorithms used to check and calculate the output data are not discussed. The mesher is also able to discretize surfaces that have more complex tapers with varying height. Although there are additional algorithm steps for such surfaces, the algorithm described above forms the foundation of the code.

As a final output, the mesher produces a 3D plot of the discretized surface. Since symmetry is used in the in-house MoM solver, only one surface is defined and plotted in all cases.

To illustrate the successful implementation of a mesher, some example surfaces which have been discretized are shown in Figure 5.10.

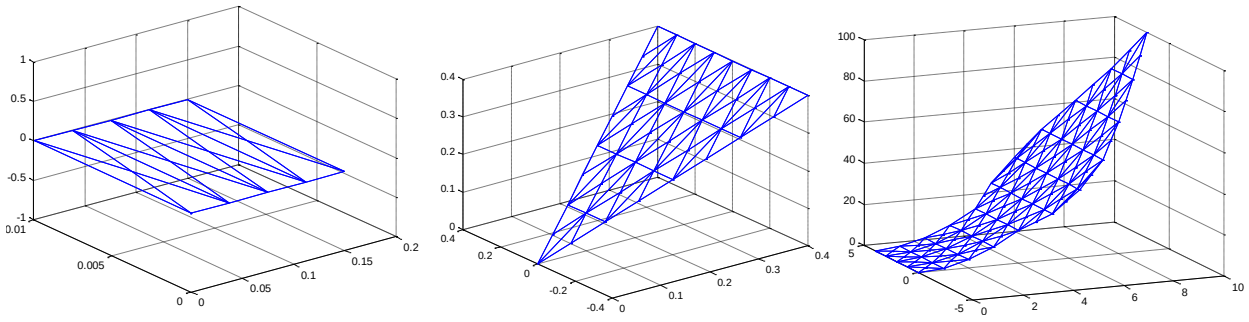

Figure 5.10: Examples of meshed structures

The following sections further illustrate the successful implementation of the mesher, by showing that accurate results are achieved with the in-house MoM solver, which uses the data calculated by the mesher.

5.3 Results

This section illustrates the successful implementation of the in-house MoM solver for typical TEM horn antennas and their basic constituents. The code was gradually developed and debugged by testing the current and field characteristics of the following antennas:

1. A single flat plate, half a wavelength long at 1 [GHz] (0.15 [m]) with a width of 0.01 [m] is fed at its centre. The current on the plate calculated using the in-house code is compared to the current obtained when the structure is analysed in FEKO. This is done to determine whether the triangle current coefficients (I_n) are calculated correctly.

2. The second type of antenna analysed is a parallel plate waveguide. This tests the implementation of the differential feed method as well as image theory. The electric farfield of the parallel plate waveguide is calculated from the current coefficients as discussed in Section 5.1.4. All results are compared to those obtained using FEKO.

3. After testing the parallel plate waveguide, the code is tested with a ribbon antenna which consists of two thin, flat plates which are flared away from each other.

4. Finally, the in-house solver is tested with a basic TEM horn antenna, to show that it is implemented successfully for flared plates which have varying width.

It is important to note that all antennas are assumed to consist of plates which are modelled as perfect electrical conductors (PEC).

5.3.1 Flat Plates

Single Plate

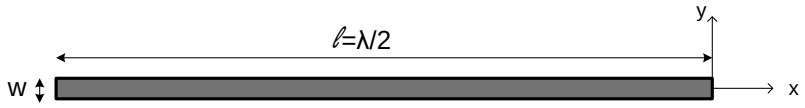

Figure 5.11: Dimensions of thin flat plate

The first structure used to test the in-house solver is a thin, flat plate which is fed at its centre like a dipole. The dimensions and orientation of the plate are shown in Figure 5.11. The plate is lying along the x axis with a length of 0.15 [m] ($\frac{\lambda}{2}$ at 1 [GHz]) and has a width of $w = 0.01$ [m]. Since the structure does not vary in the z direction, there will be no z-component of surface current. Therefore, the arbitrarily chosen height of the plate above the xy-plane ($z = z_0$) is irrelevant at this stage.

Figure 5.12 shows the mesh created by FEKO to determine the current on the plate. The mesh is asymmetrical and uses a different algorithm to the in-house code. The mesh created by the in-house code is symmetrical as can be seen from Figure 5.13.

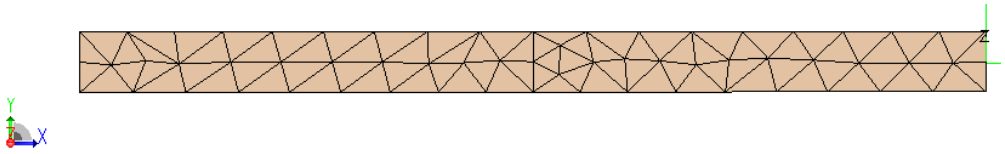

Figure 5.12: Flat plate mesh and fed at centre - FEKO

The structure is fed with a voltage source at the red ($n = 80$) and green ($n = 86$) non-boundary edges indicated in Figure 5.13, by setting $V_{80} = V_{86} \neq 0$ in Equation 5.12. The values of E_m chosen for the source edges may have any magnitude, as the current density magnitude of both solvers is normalised for the comparison. The FEKO source voltage, as well as the in-house solver excitation, are given a phase of 0 [^{o}].

Since the plate is fed at its centre, has a relatively small width and is half a wavelength long it will have a similar current distribution to a half-wavelength dipole antenna. The current is expected to have a half-wave sinusoidal distribution along the length of the plate. Since the width of the plate is relatively small compared to the length, the y-component of the current will be almost negligible and is not calculated. Therefore, only the magnitude and phase of J_x (x-component of the surface current density) is calculated for comparison with FEKO.

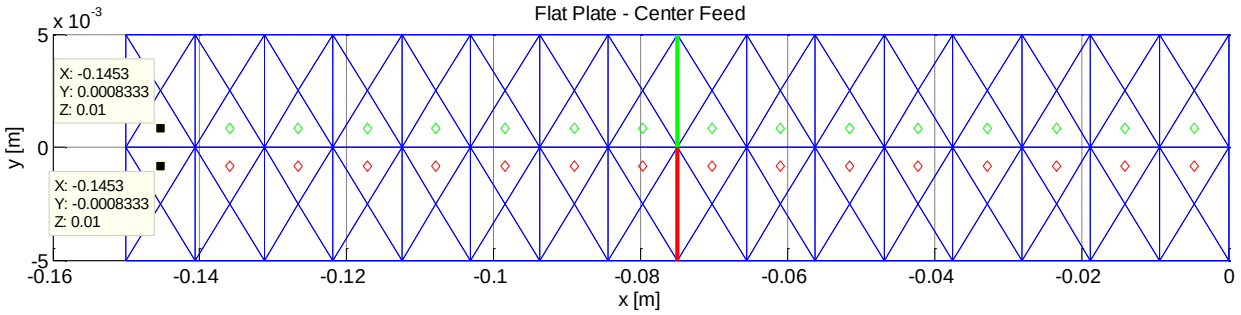

Figure 5.13: Flat plate fed at the highlighted edges. Current sample points are indicated by diamonds

Due to the different meshing algorithms used by the in-house solver and FEKO, the triangles, edges, triangle centroids and current coefficients are defined differently. It is relatively easy to calculate the current density at the triangle centroids, since the basis functions are previously defined for the calculation of the current coefficients. However, it is a lot of effort to calculate the current density anywhere else in a triangle. Therefore, FEKO only provides the current density values at the centroids of the triangles in Figure 5.12. This poses a problem since the centroids of the triangles obtained with the in-house code do not coincide with those of FEKO.

However, FEKO is able to calculate the magnetic near field anywhere, except on the surface of the conductor at $z = z_0$. The magnetic near field is calculated at the (x,y) coordinates of the centroids of the in-house triangles, but at a slight offset above the conductor at $z = z_{near} = z_0 + 10^{-4}$ [m]. This is useful because the current density is related to the magnetic field at the boundary of a conductor by [15],

$$\mathbf{J} = \hat{n} \times \mathbf{H} \tag{5.43}$$

The y-component of the current density is negligible for a very thin plate. Therefore, only J_x is calculated with the in-house solver and compared to H_y at $z = z_{near}$. The offset of 10^{-4} is much less than λ at 1 [GHz] and considered sufficiently small so that $H_y(z = z_o) \approx H_y(z = z_{near})$.

The centroids of the triangles in Figure 5.13 fall on the lines $y = 0.00083$ [m] and $y = -0.00083$ [m] and are indicated by the green and red diamonds, respectively. J_x is calculated along both lines to check the symmetry of the solution. The current density distributions calculated with FEKO at $y = 0.00083$ [m] as well as those calculated with the in-house code at $y = 0.00083$ and

$y = -0.00083$ [m] are shown in Figure 5.14. The normalised magnitude of J_x is shown in Figure 5.14 (a) and the phase of J_x in Figure 5.14 (b). No distinction is made for H_y as from this point onwards it is assumed to be equivalent to J_x calculated by FEKO.

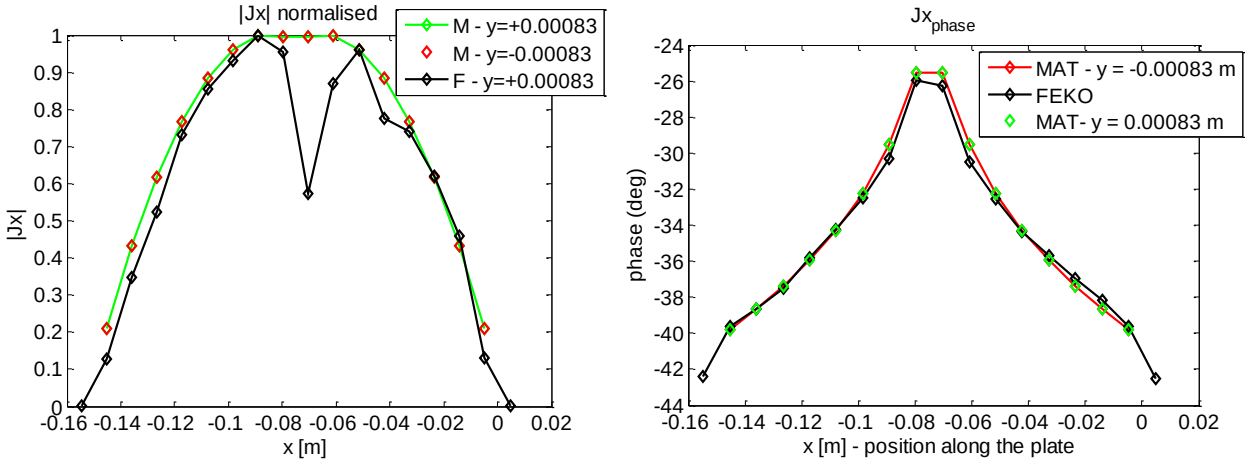

Figure 5.14: Current density distribution at 1 [GHz] on a $\lambda/2$ flat plat: (a) normalised $|J_x|$ (b) Phase J_x

The legend entries (M or MAT) and (F or FEK) refer to MATLAB and FEKO, respectively. The magnitude plots compare fairly well apart from the sharp dip in the FEKO plot, whereas the phase distributions obtained with the two solvers are almost identical. The differences are attributed to calculating H_y at an offset above the plate instead of on the plate. However, the results compare sufficiently well to assume that the triangular patch MoM has been implemented successfully. Further proof is visible from the symmetry of the current density around the x-axis.

From the results in this section, it is concluded that the MoM is successfully implemented for the analysis of a single flat plate.

Parallel Plate Waveguide

A parallel plate waveguide is used to test the implementation of symmetry as well as the differential feed method described in Section 5.1.5. The parallel plate antenna is formed by placing two flat plates (identical to the one in Figure 5.12) at heights $z = +d/2 = l/32$ and $z = -d/2$, respectively. The dimensions of the plates are exactly the same as those for the single plate but are repeated in Table 5.1. Instead of applying a centre feed at non-boundary edges in the middle of the plate, a differential feed is applied between the plates at $x = -l$ as discussed in Section 5.1.5. The boundary edges used for this purpose are highlighted in red and green in Figure 5.15. The in-house solver makes use of symmetry to analyse typical 2-plate TEM antenna structures. Therefore, only one plate is defined and drawn as previously discussed. Symmetry is not used in FEKO as the solver is very fast, especially for such small problems.

l [λ]	d_o	w_o [m]	y_{c1} [m]	y_{c2} [m]	y_{c3} [m]	y_{c4} [m]	y_{c5} [m]	y_{c6} [m]
$\lambda/2$	$l/16$	0.01	0.00083	-0.00083	0.00167	-0.00167	0.00416	-0.00416

Table 5.1: Parameter values and y-coordinates of triangle centroids of the plate in Figure 5.15

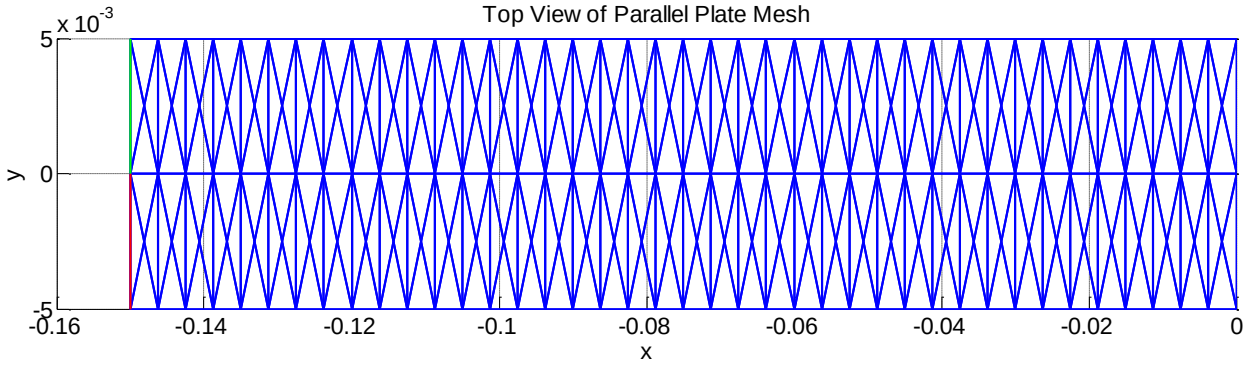

Figure 5.15: Top view of mesh created with MATLAB for the half-wavelength parallel plate

Figure 5.16 shows the geometry of a parallel plate waveguide (both plates) as well as the chosen wire feed, in FEKO.

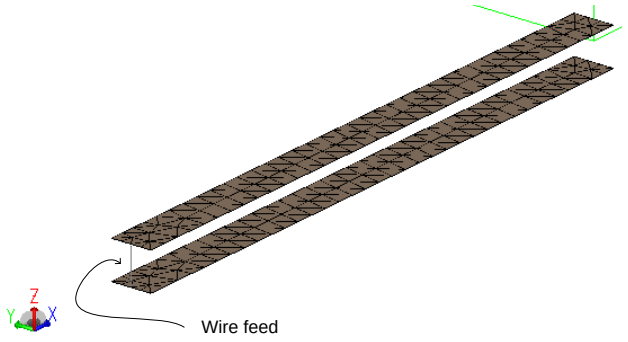

Figure 5.16: Parallel plate with wire feed as discretized by FEKO

The value of d_o is chosen small so as to minimise the radiation effect of the wire which adds a radiating element of length $d_o = l/16$. The current density distribution on the top plate is calculated with the in-house solver for $y = y_{c1}$ and compared to the distribution $H_{y=y_{c1}}$ calculated by FEKO. Figure 5.17 shows the normalised magnitude of the current density distribution J_x and its phase along the plate. The magnitude distributions compare very well. The phase values also compare well, with the slight offset between the two results attributed to the fact that H_y is not calculated on the plate, but at $z = z_{near}$, as previously discussed.

The code of the in-house solver is extended to calculate the electric farfield of an antenna from the surface current densities, as discussed in Section 5.1.4. Figure 5.18 shows the magnitude of the total field and its components. The results are very similar the FEKO results shown in Figure 5.19.

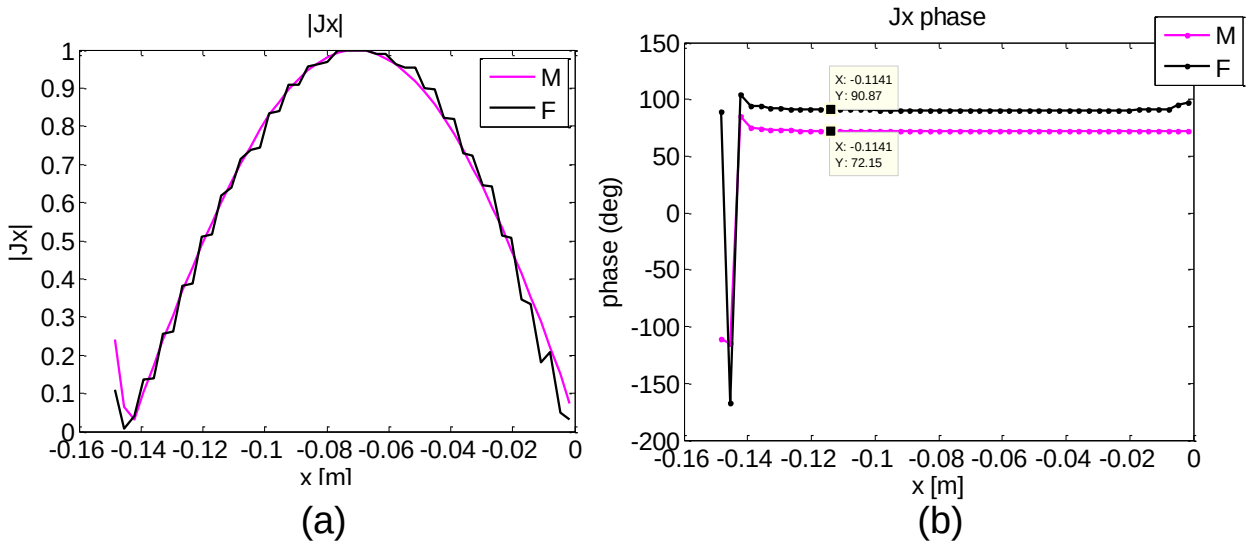

Figure 5.17: Current density distribution at 1 [GHz] for a $\lambda/2$ parallel plate waveguide at $y_{c1} = 0.00833$ [m] (a) normalised $|Jx|$ (b) Phase of J_x. (M - MATLAB) (F - FEKO)

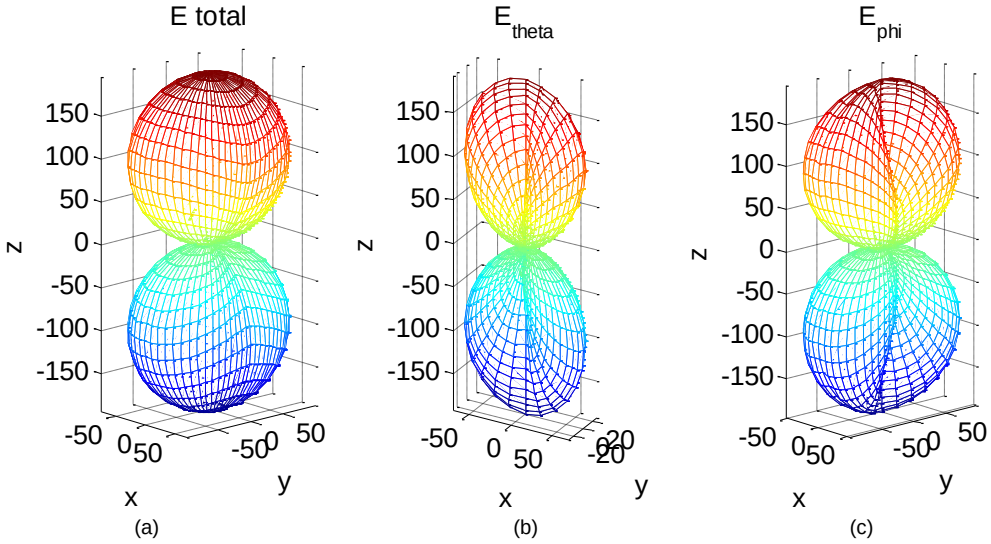

Figure 5.18: Electric farfield and its components for parallel plates calculated with in-house code: (a) $|E_{total}|$ (b) $|E_\theta|$ (c) $|E_\phi|$

Two-dimensional plots of $|E_{total}|$ are used to make a better comparison of the results. Figure 5.20 shows the 2D plots of a normalised $|E_{total}|$ for the two solvers for three values of ϕ. The results compare well with differences attributed to various aspects such as different mesh definitions, degree of quadrature integration used in the solvers etc.

The results of this section illustrate the successful implementation of symmetry for an antenna with a differential feed. A ribbon antenna will be used as the next intermediate test subject to determine if the code works for plates which are flared away from each other.

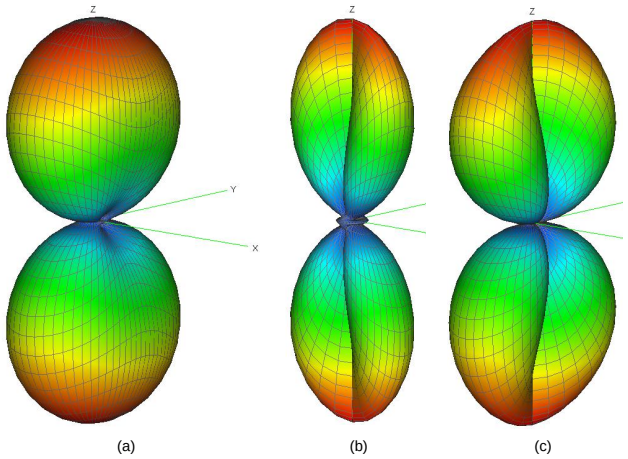

Figure 5.19: Electric farfield and its components for parallel plates calculated with FEKO: (a) $|E_{total}|$ (b) $|E_\theta|$ (c) $|E_\phi|$

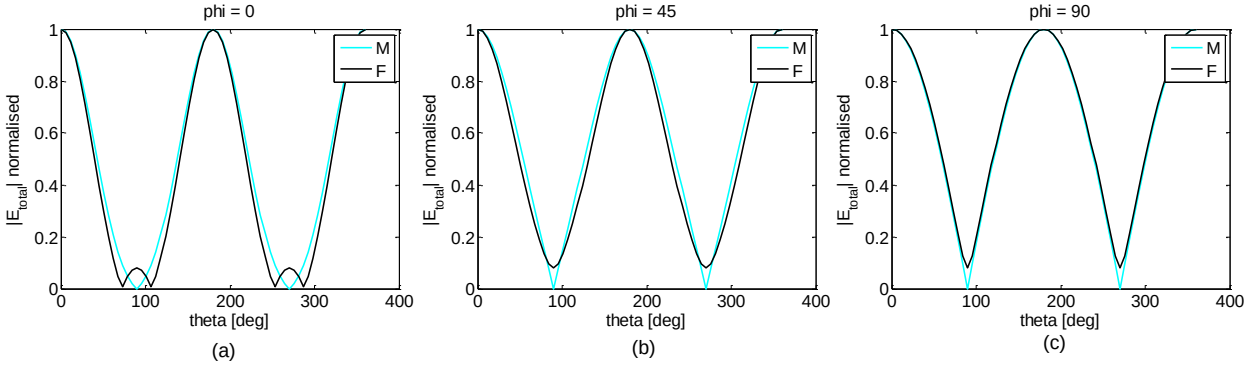

Figure 5.20: 2D plots of $|E_{total}|$ versus θ for parallel plates: (a) $\phi = 0$ [^{o}] (b) $\phi = 45$ [^{o}] (c) $\phi = 90$ [^{o}]

5.3.2 Basic TEM Horns

Ribbon Horn

Figure 5.21 (a) and (b) show the side and top views of a ribbon antenna. The antenna consists of two thin flat plates, which are separated by a distance d and flared away from each other by an angle of θ. It is important to note that the antenna is positioned on the coordinate system so that it will radiate in the z-direction. This is done so that the E- and H-planes can be plotted according to the following convention:

- E-plane - plot $|E_{total}|$ vs θ for $\phi = 90$ [^{o}]
- H-plane - plot $|E_{total}|$ vs θ for $\phi = 0$ [^{o}]

The mesh created for the ribbon by the in-house code is shown in Figure 5.22. Once again, only one plate is required for the calculations because the solver makes use of symmetry. The red and green boundary edges in Figure 5.22 are used for the differential feed method.

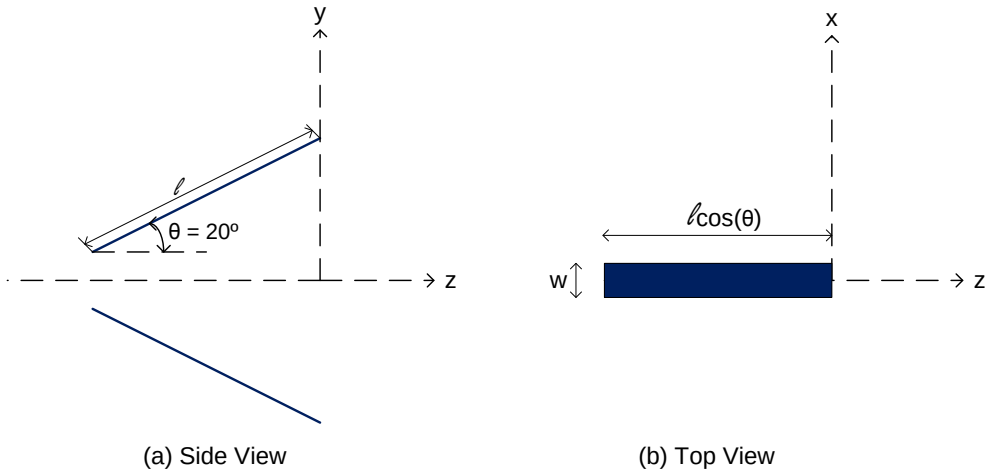

Figure 5.21: (a) Side view and (b) top view of a typical ribbon antenna

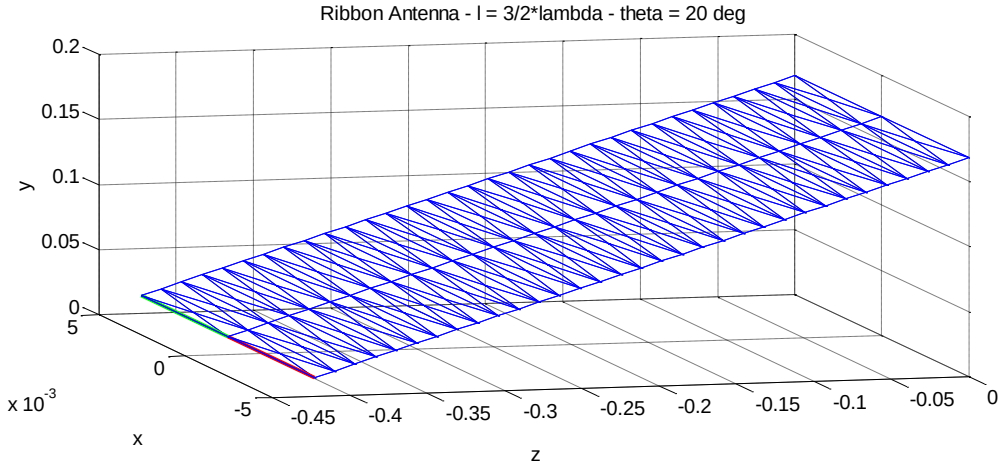

Figure 5.22: Top plate and mesh of ribbon antenna

As with the parallel plate waveguide, a wire feed is used in the FEKO simulation. The plate length l is chosen as 0.45 [m] ($\frac{3}{2}\lambda$ at 1 [GHz]), θ is 20 [^{o}] and d is chosen as $\frac{\lambda}{16}$ to minimise radiation of the wire feed used in FEKO.

Figure 5.23 and Figure 5.24 show the magnitude of the total electric farfield and its components as calculated with the in-house solver and FEKO, respectively. The 3D patterns obtained with the two solvers are very similar, but the accuracy is better compared with the 2D $E-$ and $H-$ plane patterns as well as an intermediate plane pattern at $\phi = 45$ [^{o}] shown in Figure 5.25. Note that the data is first normalised and then converted to [dB] for better interpretation.

Th differences between the FEKO and MATLAB results are more visible in the 2D plots and are attributed to the reasons discussed in Section 5.3.1. However, the results are very similar and again illustrate the success of the in-house solver.

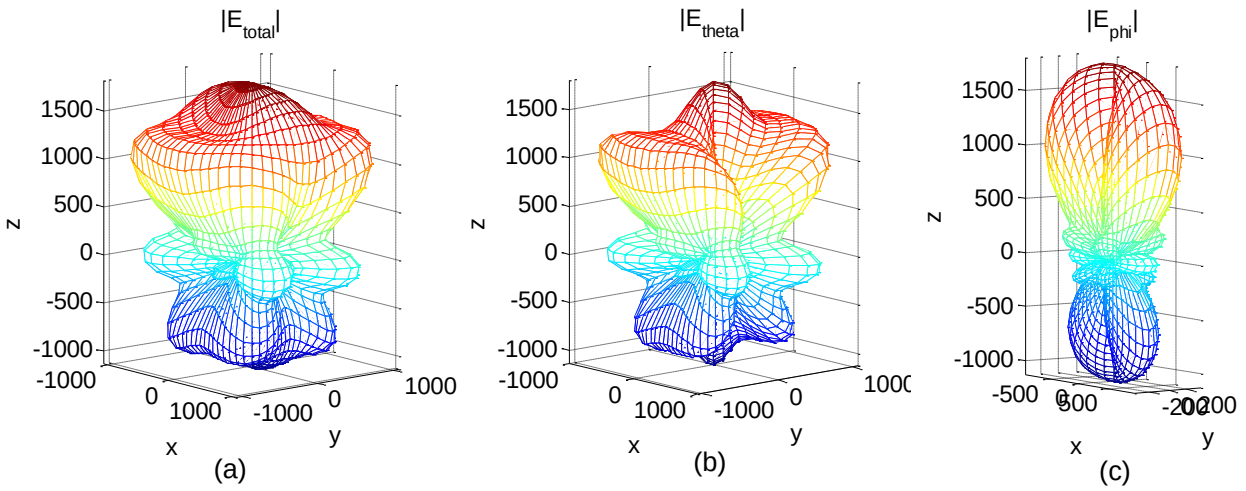

Figure 5.23: Electric farfield pattern for ribbon antenna as calculated by MATLAB: (a)$|E_{total}|$ (b)$|E_\theta|$ (c) $|E_\phi|$

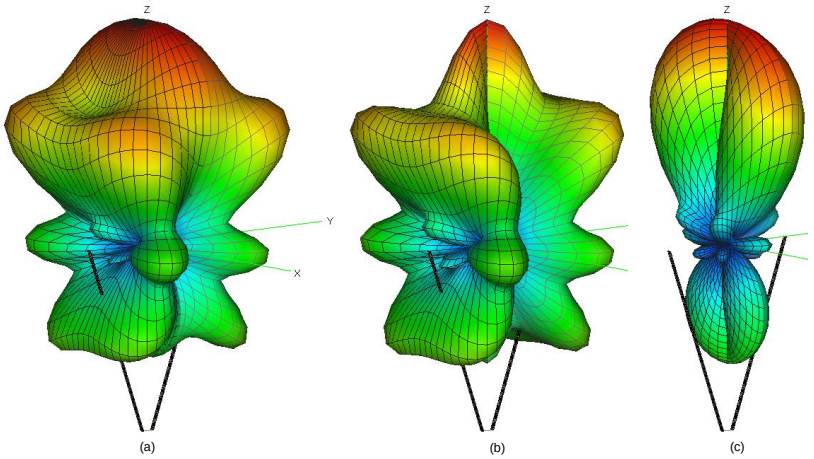

Figure 5.24: Electric farfield pattern for ribbon antenna as calculated by FEKO: (a)$|E_{total}|$ (b)$|E_\theta|$ (c) $|E_\phi|$

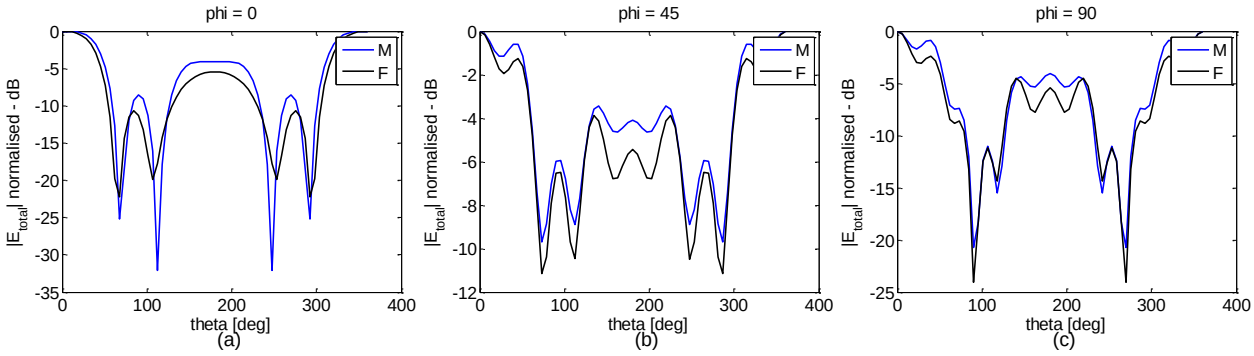

Figure 5.25: 2D plots of $|E_{total}|$ versus θ for ribbon antenna: (a) $\phi = 0$ [^{o}] (b) $\phi = 45$ [^{o}] (c) $\phi = 90$ [^{o}]

Linear Tapered Horn

A basic linear tapered TEM horn is used as the final test subject to determine whether implementation the in-house MoM solver is a success.

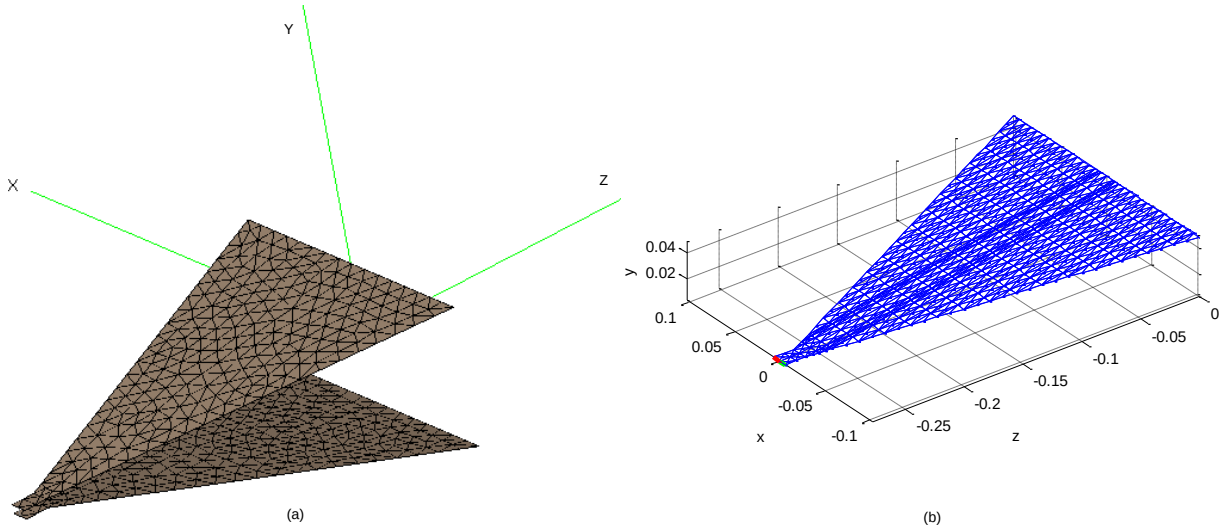

Figure 5.26: Linear Tapered TEM horn with mesh as represented by (a) FEKO (b) MATLAB

Figure 5.26 (a) and (b) show the basic TEM horn with the meshes created by FEKO and MATLAB respectively. Since symmetry is used in the in-house code, the MATLAB figure shows only the top half of the structure. The dimensions of the horn are defined as shown in Figure 3.5 and have the nominal values in Table 5.2.

Parameter	s [mm]	α [^{o}]	β [^{o}]	h [mm]
Value	300	40	20	$\frac{bsin(\beta/2)}{16}$

Table 5.2: The set of nominal parameter values chosen for the basic TEM horn in Figure 5.26

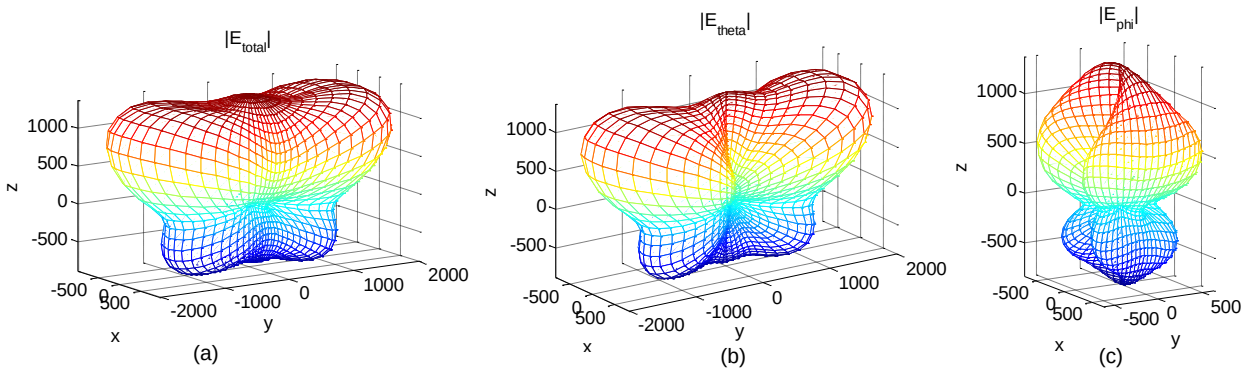

Figure 5.27: 3D electric farfield patterns of linear TEM horn as calculated by the in-house solver (a)$|E_{total}|$ (b) $|E_\theta|$ (c) $|E_\Phi|$

Figure 5.27 shows the total 3D electric farfield pattern as well as its θ and ϕ components. The FEKO results are plotted in Figure 5.28 and correspond closely to those of the in-house solver. The

2D plots in Figure 5.29 of $|E_{total}|$ in [dB] after normalisation also clearly show that the results of the in-house solver compare very well to the FEKO results.

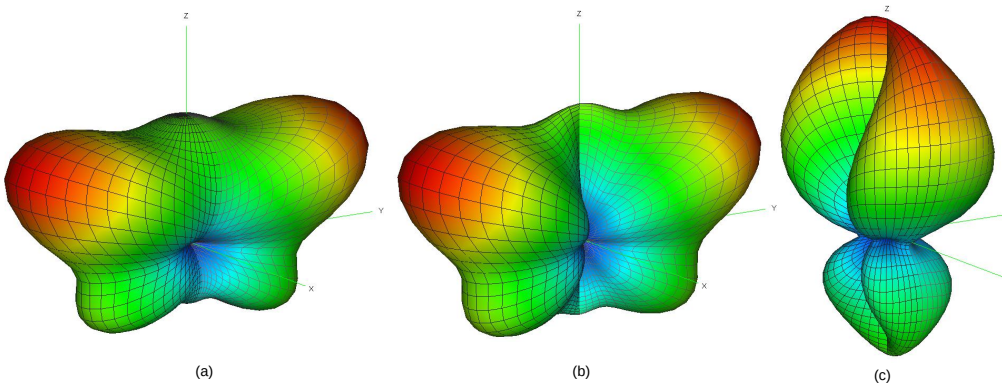

Figure 5.28: 3D electric farfield patterns of linear TEM horn as calculated by FEKO (a)$|E_{total}|$ (b) $|E_\theta|$ (c) $|E_\Phi|$

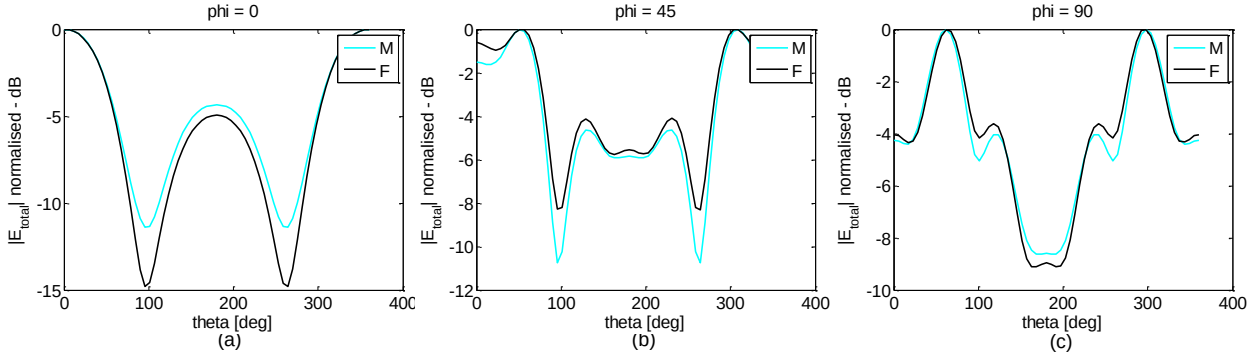

Figure 5.29: 2D plots of $|E_{total}|$ in [dB] after normalisation: (a)$\phi = 0$ [^{o}] (b)$\phi = 45$ [^{o}] (c)$\phi = 90$ [^{o}]

5.3.3 Conclusion

From the results in this chapter, it can be concluded that the implementation of a Method of Moments solver for tapered TEM horn antennas is a success. There is, however, an order of magnitude difference between the execution time of the in-house code and FEKO, due to the optimized nature of the FEKO code. Therefore, FEKO (or CST) is used for the remainder of work in this thesis.

Chapter 6

Modified Exponentially Tapered TEM Horns

This chapter discusses the achievement of a rounder radiation pattern over a wide bandwidth using exponential TEM horns which have been modified to end with a convex arc. In Chapter 3 it is explained that the E- and H-plane patterns generally show divergent behaviour as the angular separation between the plates of a TEM horn (β) and the width of the plates (α) increases. By modifying the width profile of the horn towards the mouth of the antenna, the difference between the E- and H-plane directivity is reduced.

Mallahzadeh et al [8] discuss the influence of a concave arc segment on the radiation pattern. The antenna discussed in [8] is similar to the one in Figure 6.4 (a) and the article claims that modifying a TEM horn by cutting away a concave arc at the mouth of the antenna, prevents break up of the main lobes of the E- and H-plane electric farfield patterns at higher frequencies. Since the results in [8] are only for a single antenna, it is further investigated. In addition, it is proposed to investigate the influence of *convex* arcs on the radiation. In this chapter, an exponential TEM horn with a convex parabolic or convex triangular arc is proposed and found to yield a round radiation pattern over a wide bandwidth.

6.1 Standard Exponential TEM Horn

A standard exponential TEM horn antenna is shown in Figure 6.1. The analytical procedure used to design an exponentially tapered TEM horn is obtained from [8] and discussed below.

Figure 6.2 provides a top and side profile of the standard exponential TEM horn, as well as the dimension parameters which are of interest. The parameters indicated in Figure 6.2 are defined as follows:

- L - total length of the antenna

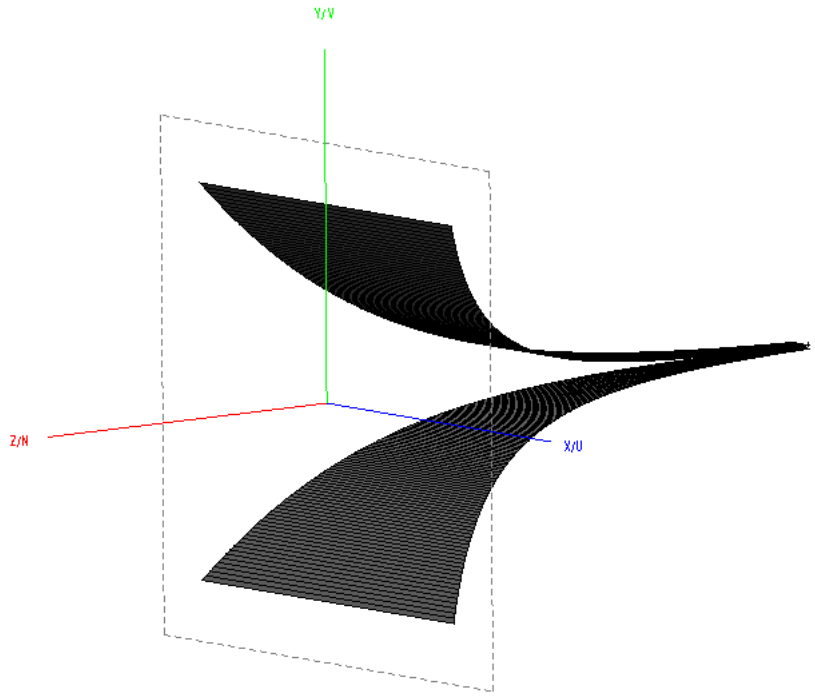

Figure 6.1: Standard Exponential TEM Horn Antenna

- d_o - initial plate separation at the position $z = 0$
- d_L - plate separation at the mouth of the antenna at $z = L$
- w_o - initial plate width at $z = 0$
- w_L - plate width at the mouth of the antenna at $z = L$
- $d(z)$ - plate separation at a position z along the antenna
- $w(z)$ - width of the plates at a position z along the antenna

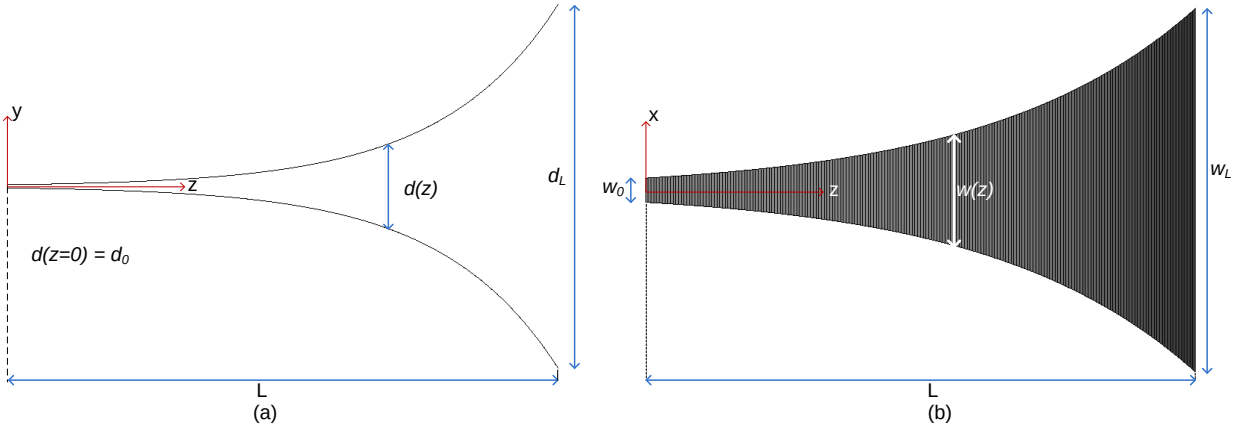

Figure 6.2: Standard Exponential TEM Horn Antenna: (a) side view (b) top view

According to [8], the parameters are chosen so that the impedance of the antenna gradually increases from Z_o at $z = 0$ to the intrinsic impedance of free space $\eta_o = 377$ [Ω] at $z = L$. This is done by assuming that the impedance at any position z along the antenna can be approximated by the characteristic impedance equation for a parallel plate waveguide [8]:

$$Z(z) = \eta_o \frac{d(z)}{w(z)} \tag{6.1}$$

The impedance along the antenna is chosen as [8],

$$Z_z = Z_o e^{\alpha z} \tag{6.2}$$

where,

$$\alpha = \frac{1}{L} \ln(\frac{\eta_o}{Z_o}) \tag{6.3}$$

If the plate separation is chosen as,

$$d(z) = d_o e^{bz} \tag{6.4}$$

where,

$$b = \frac{1}{L} ln(\frac{d_L}{d_o}) \tag{6.5}$$

the function which defines the width of the plates ($w(z)$) can be calculated from Equation 6.1.

The procedure discussed in this section is used as the basis to design all the exponential horns discussed in this chapter.

6.2 Arced Horns

This section investigates the influence of a concave or a convex arc at the mouth of an exponentially tapered TEM horn, on the E- and H-plane electric farfield radiation patterns. Figure 6.3 illustrates the way in which the standard exponential TEM horn is modified to have either a concave or convex arc.

6.2.1 Concave vs Convex Arc

Figure 6.4 (a) and (b) show the top view and side view of the exponential horn with a concave or convex arc, respectively. The dotted lines represent the top view profile of the standard exponential horn which has been modified to obtain the arced horns. The following antennas which will be compared in this section:

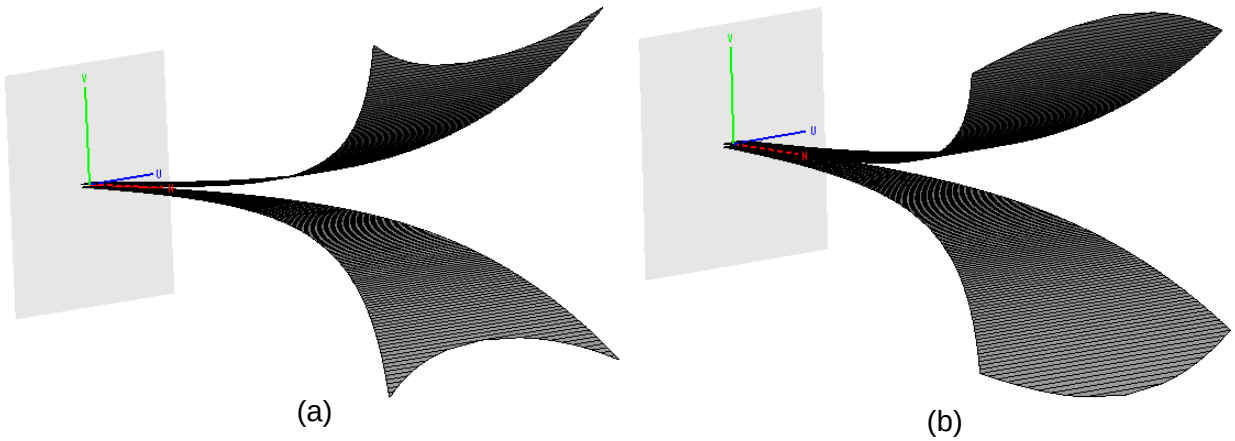

Figure 6.3: Top view of modified exponential TEM horn: (a) concave arc (b) convex arc

1. Standard exponential TEM horn
2. Exponential horn with a concave parabolic arc
3. Exponential horn with a convex parabolic arc

It is important to note that the three antennas will have the same maximum length L as well as the same plate separation profile $d(z)$ as indicated by Figure 6.2 and 6.4. Once the arc depth d_{arc} is chosen (as a fraction of L), the width profile $w(z)$ is recalculated from the position $z = L - d_{arc}$ for the modified horns, using the equations for a concave or convex **parabolic** arc. This type of curve is used since it varies smoothly and is easy to implement.

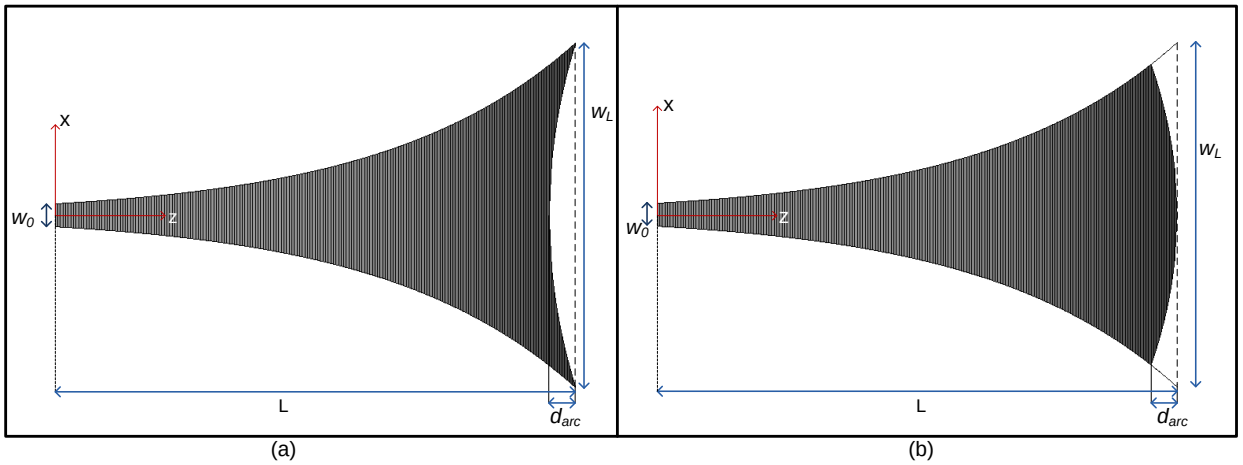

Figure 6.4: Top view of modified exponential TEM horn: (a) concave arc (b) convex arc

The influence of the arcs on the electric farfield pattern is investigated by analysing the three antennas in FEKO and comparing the E- and H-plane directivity at a 1, 4 and 7 [GHz]. For simulation purposes, all the antennas are defined to propagate in the z-direction, with the aperture

at the antenna mouth centred at the origin. A parallel plate feed section of length $feed_l$, width w_o and plate separation d_o is added to the back of each antenna as shown in Figure 6.5. A thin wire is inserted between the plates to allow the use of a wire port in FEKO.

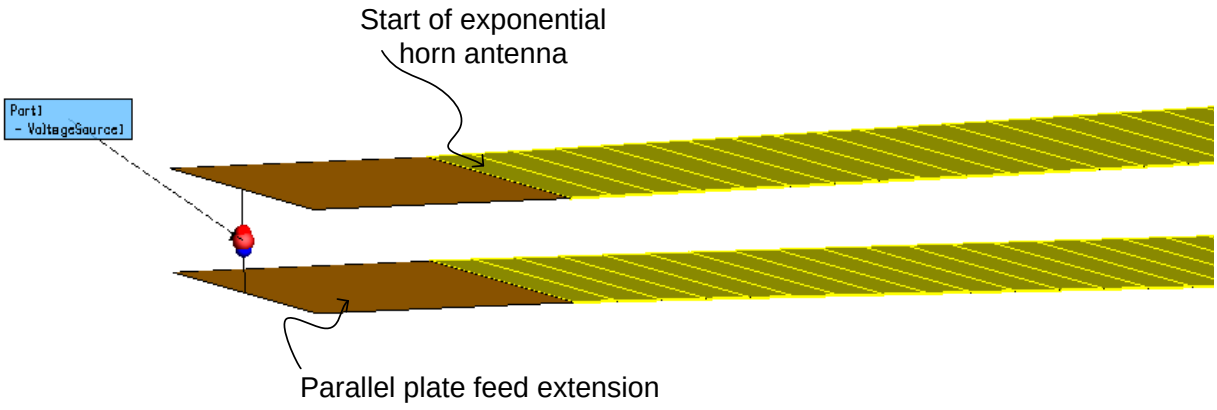

Figure 6.5: Parallel plate feed extension and wire port used to feed the exponential TEM horns in FEKO

L [λ]	d_o [mm]	w_o [mm]	d_L [λ]	w_L [λ]	$feed_l$ [mm]	d_{arc}
2.3	3.98	30	1.5	d_L	10	$L/20$

Table 6.1: Nominal parameter values for the standard exponential horn, an exponential horn with a concave arc and an exponential horn with a convex arc in Section 6.2.1

The nominal parameter values chosen for the three exponential TEM horns are indicated in Table 6.1. The projected length of the antenna (L) and aperture height d_L are chosen so that the antenna is large enough for the lower frequencies to propagate and calculated from Equation 6.6 so that $|s_{11}|$ is below a chosen design value. The shorter the length over which the impedance is increased from 50 [Ω] to the characteristic impedance of free space η_o, the larger $|s_{11}|$ becomes. Chapter 5 in [11] gives the magnitude of the reflection coefficient for an exponential taper such as in Figure 6.2 (a) with a characteristic impedance $Z_o e^{\alpha z}$, increasing from Z_o at $z = 0$ to Z_L at $z = L$ as,

$$|\Gamma| = |ln(\frac{Z_L}{Z_o})\frac{sin(\beta L)}{\beta L}| \tag{6.6}$$

The magnitude of the reflection coefficient in [dB] is plotted in Figure 6.6 versus L/λ. A length of $L = 2.3\lambda$ is chosen so that the reflection coefficient will be below -22 [dB] at the lowest frequency (1 [GHz]) in the bandwidth.

The initial plate width w_o is chosen and d_o is calculated using Equation 6.1 so that $Z_o = 50$ [Ω]. The aperture height is chosen as 1.5λ and since the design requires $Z_L = \eta_o$, $w_L = d_L$ according to Equation 6.1. As discussed a short parallel plate section with a length of 10 [mm] is added

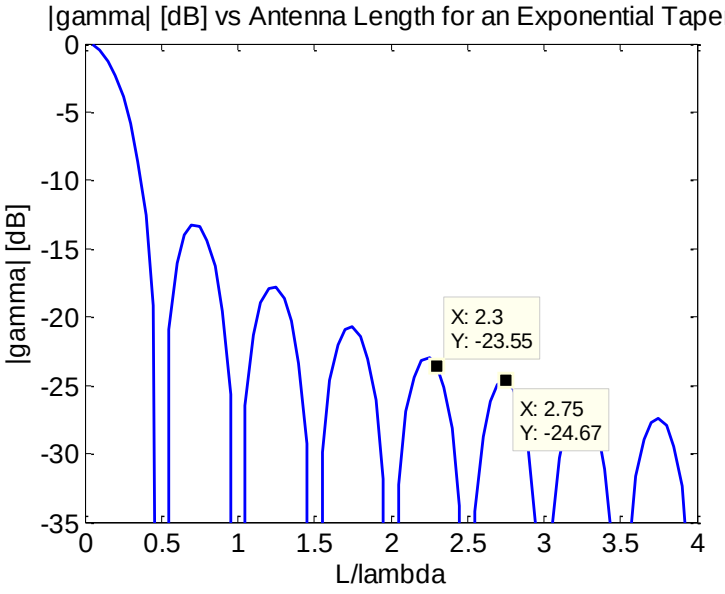

Figure 6.6: $|\Gamma|$ in [dB] vs L/λ for an exponential taper

for the feed. A nominal value of $L/20$ (5% of L) is chosen for the arc depth of the two modified exponential horns.

The E- and H-plane directivity of each of the three exponential TEM horns is calculated with FEKO using approximately the same mesh accuracy for each antenna. The results are shown for 1, 4 and 7 [GHz] in Figures 6.7-6.9.

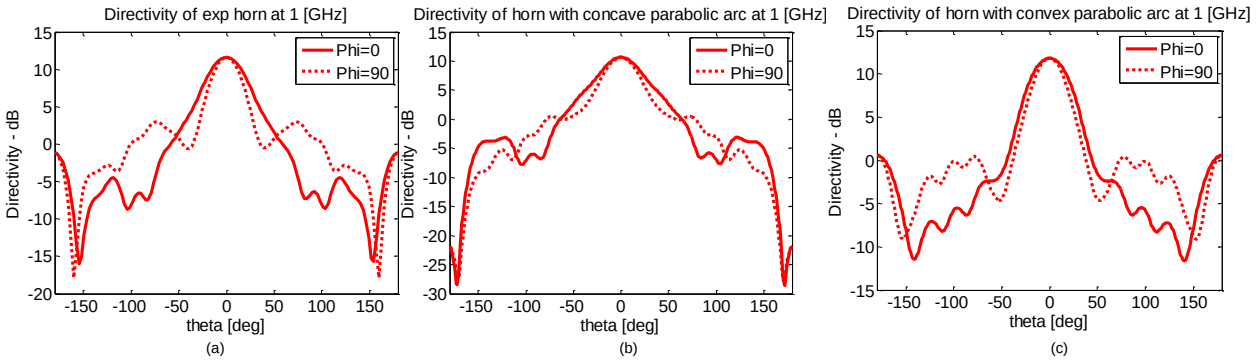

Figure 6.7: Directivity at 1 [GHz] of (a) standard exponential TEM horn, (b) exponential TEM horn with concave parabolic arc ($L/20$) (c) exponential TEM horn with convex parabolic arc ($L/20$)

The most striking result is the close correlation between the E- and H-plane patterns in Figure 6.7 (c), obtained at 1 [GHz] with the antenna with the convex arc. The result warrants further investigation into whether a round radiation pattern can be achieved (according to the criteria in Chapter 1) over a wide bandwidth using a convex arc.

The concave arced horn also offers some improvement in terms of roundness by widening the E-plane pattern so that the difference between the E- and H-planes decreases. However, the

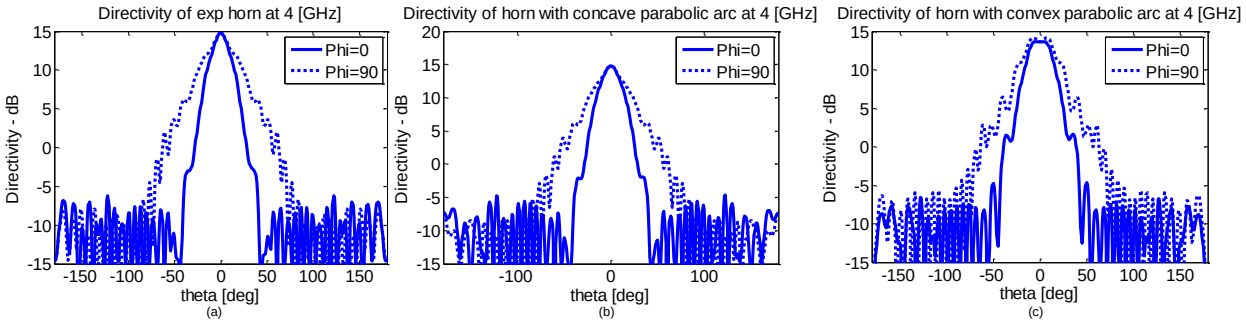

Figure 6.8: Directivity at 4 [GHz] of (a) standard exponential TEM horn, (b) exponential TEM horn with concave parabolic arc ($L/20$) (c) exponential TEM horn with convex parabolic arc ($L/20$)

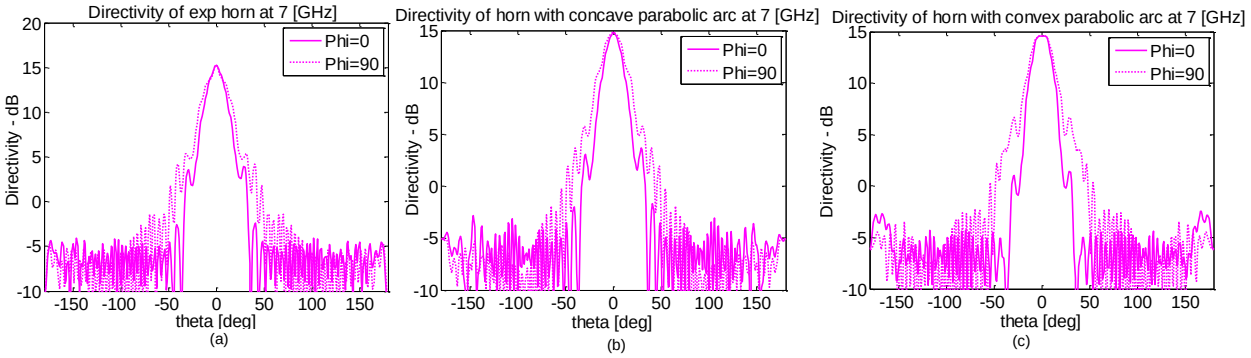

Figure 6.9: Directivity at 7 [GHz] of (a) standard exponential TEM horn, (b) exponential TEM horn with concave parabolic arc ($L/20$) (c) exponential TEM horn with convex parabolic arc ($L/20$)

improvement is not as significant as with the convex arc.

Neither of the arced horns offer a notable improvement with regards to the roundness of the pattern at the higher frequencies. This is most likely since the higher frequencies break away from the antenna before the start of the arced segments. It is expected that if the arc depth is increased, a similar improvement in the roundness of the radiation pattern will be achieved at the higher frequencies.

In terms of gain and side lobe levels, all three of the exponential horns perform fairly well. As the horn with the convex arc shows the most potential to achieve a round radiation pattern, it is decided to proceed by investigating the influence of the (convex) arc depth on the radiation characteristics. The analysis is done for an exponential horn with a parabolic arc and is repeated as for one with a triangular arc.

6.2.2 Convex Parabolic Arc

This section discusses the influence of arc depth on the roundness of the radiation pattern of an exponential TEM horn with a convex parabolic arc, such as the one in Figure 6.3 (b). The results are compared to those for the standard exponential horn in each case using the definition of a round

radiation pattern in terms of the relevant parameters defined in Chapter 1.

To extend the effect of the arc on the radiation pattern to the higher frequencies, the length of the antenna (and that of the standard exponential horn used for comparison) is reduced while keeping the aperture height and initial height d_o the same as before. This increases the rate at which the characteristic impedance and antenna dimensions change, especially towards the mouth of the antenna allowing the frequencies to break away closer together and thereby extending the influence of the arc to a wider frequency range. A length $L = 1.8\lambda$ is chosen so that $|s_{11}|_{dB}$ predicted by Equation 6.6 is below -20 [dB].

The nominal parameter values for the shortened exponential horn with a convex parabolic arc is shown in Table 6.2.

L [λ]	d_o [mm]	w_o [mm]	d_L [λ]	w_L [λ]	$feed_l$ [mm]	d_{arc}
1.8	3.98	30	1.5	d_L	10	$L/20$

Table 6.2: Nominal parameter values for the shortened exponential horn with a convex parabolic arc

The arc depth of the modified horn is varied between $\frac{L}{20}$ and $\frac{L}{4}$ to determine its influence on roundness of the radiation pattern. Instead of using E- and H-plane plots such as those in Figure 6.7, better visual interpretation is achieved by plotting the **difference** between the E- and H-plane patterns (in [dB]) at a number of sample frequencies.

The **difference** function is a positive value defined as,

$$difference(\theta)\ [\text{dB}] = |D_{\phi=90}(\theta) - D_{\phi=0}(\theta)|\ [\text{dB}] \tag{6.7}$$

Figures 6.10 - 6.12 show the difference functions for the modified horn with various arc depths, as well as for the standard exponential horn. The frequency range is adjusted to 1-6 [GHz] to decrease mesh sizes and simulation time. As discussed in Chapter 1, the E- and H-plane patterns can be considered equal if the difference between them is less than 1 [dB]. Therefore, we are not interested in huge deviations and can restrict the range of the difference functions to a maximum of 5 [dB] in Figures 6.10 - 6.12. In a similar manner, the angular range is restricted to -45 [^{o}]$\leq \theta \leq$ 45 [^{o}] to focus on the difference between the main beams of the E- and H-plane directivity.

The characteristics of the difference functions in Figures 6.10 to 6.12 which are important to take note of are:

- The difference functions have some amplitude oscillations around $\theta = 0$ up to some value of θ after which the E- and H-plane patterns start to deviate more drastically.
- The amplitude of the oscillations and the angular range over which they occur are important for consideration.

At 1 and 2 [GHz] it is easy to see a relationship between the difference functions and arc depth, but it becomes more difficult to define the relationship as the frequency increases. Figure 6.10 (a) shows the difference functions for the modified horn at 1 [GHz] for different arc depths. As the arc depth is increased, the amplitude of the oscillations as well as the angular range over which the oscillations occur decreases. However, if the arc depth becomes to large ($L/4$) the antenna dimensions may not be large enough to allow the lower frequencies to radiated.

To compare the roundness of the radiation patterns using the criteria in Chapter 1, the 1 [dB] angular range values (θ_{1dB}) and **Equal Levels** (EL's) are calculated from the data of the difference functions and are summarised in Tables 6.3 and 6.4, respectively.

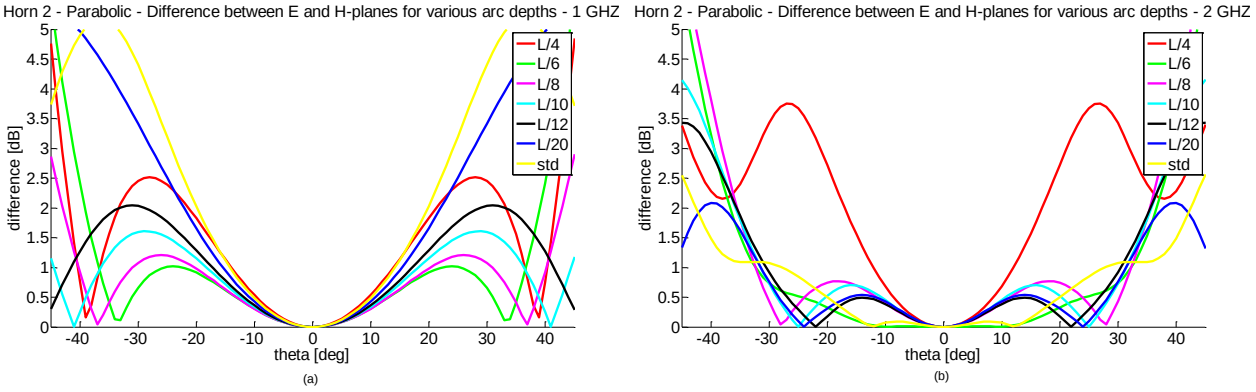

Figure 6.10: Difference between the E- and H-plane directivity for various arc depths for an exponential TEM horn with a parabolic arc: (a) 1 [GHz] (b) 2 [GHz]

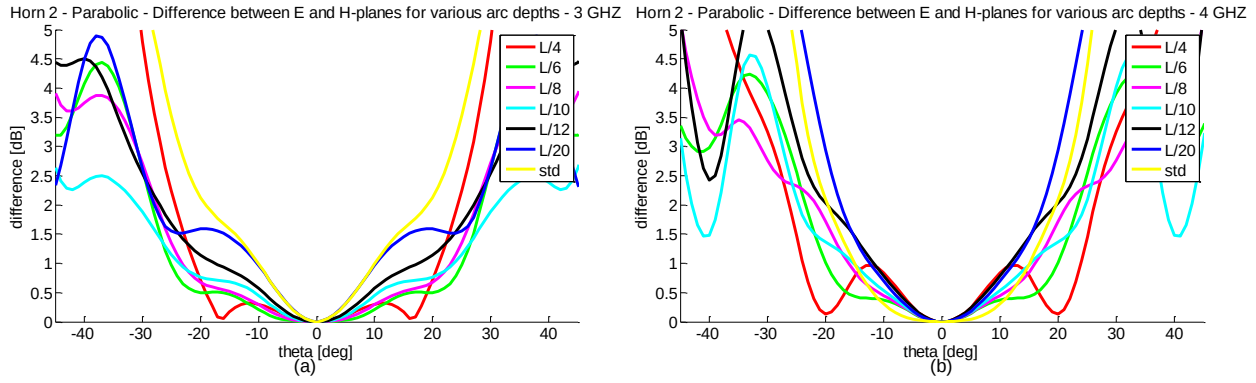

Figure 6.11: Difference between the E- and H-plane directivity for various arc depths for exponential TEM horn with a parabolic arc: (a) 3 [GHz] (b) 4 [GHz]

The values in Tables 6.3 and 6.4 which are an improvement on (or at least equal to) those of the standard exponential horn are highlighted in blue. Overall, the behaviour in Table 6.4 is similar to that in Table 6.3, with an improvement in θ_{1dB} usually coinciding with an improvement in the EL. The deviations indicate the need to look at both θ_{1dB} as well as the EL's, since a larger angular width

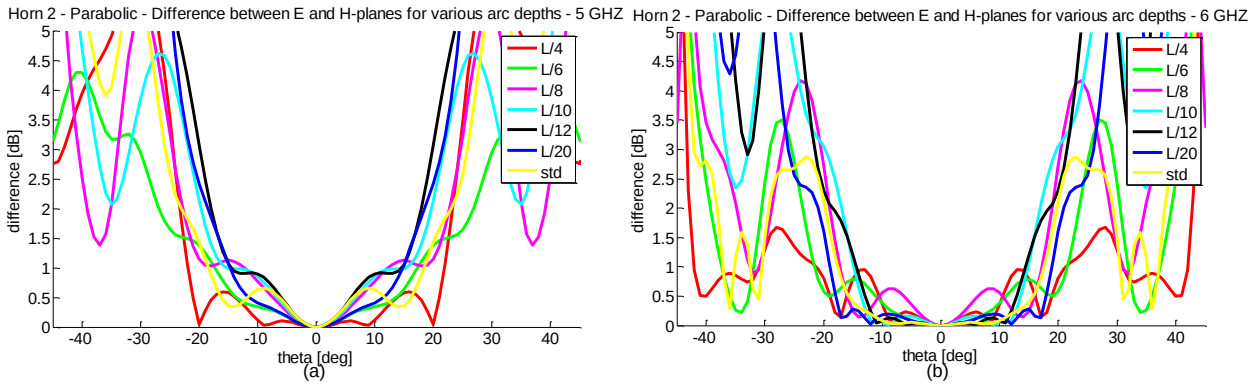

Figure 6.12: Difference between the E- and H-plane directivity for various arc depths for exponential TEM horn with a parabolic arc: (a) 5 [GHz] (b) 6 [GHz]

f [GHz]	θ_{std} [^{o}]	$\theta_{L/20}$ [^{o}]	$\theta_{L/12}$ [^{o}]	$\theta_{L/10}$ [^{o}]	$\theta_{L/8}$ [^{o}]	$\theta_{L/6}$ [^{o}]	$\theta_{L/4}$ [^{o}]
1	-14.2	-15.3	-17.2	-18.2	-20.3	-22.5	-13.95
2	-27.8	-31.4	-30.5	-31.5	-32.3	-32.3	-12.1
3	-10.1	-10.3	-17.4	-23.6	-23.1	-25.1	-21.1
4	-15	-12.3	-11.7	-15.2	-16.1	-19.9	-23.9
5	-18.4	-14.7	-14.4	-15.3	-12.3	-17.35	-21.9
6	-17.5	-18.8	-14.4	-14.8	-17.2	-21.5	-21.3

Table 6.3: $-\theta_{1dB}$ for the exponential TEM horn with a parabolic arc at various arc depths and frequencies compared to those of the standard exponential horn

does not necessarily imply a lower EL. The following observations and conclusions are made from the results in Tables 6.3 and 6.4:

- The arc depth influences the frequencies at which an improvement in the roundness of the pattern is seen, both in terms of angular range and EL's.
- The smaller arcs offer an improvement at the lower frequencies.
- As the arc depth increases, so does the frequency range over which an improvement in the roundness of the radiation pattern is seen.
- If the arc depth becomes very large, the dimensions of the antenna are changed to such an extent that the lower frequencies do not radiate and the positive effect at the low frequencies disappears. This can be seen from the last columns in Table 6.3 and Table 6.4 for an arc depth of $L/4$.
- An arc depth of $L/6$ offered the best overall improvement over the frequency range, both in terms of angular range and EL's. Although there is a slight decrease in performance at 5

[GHz], the positive effect is retained at the lower frequencies (1-3 [GHz]) and is extended to 4 and 6 [GHz].

- The EL's obtained at 1-4 [GHz] and 6 [GHz] with the exponential horn with a parabolic arc of depth $L/6$ are all below -3 [dB] or the HPBW.

In Chapter 1 it is stated that the EL should be at least -3 [dB] for the pattern to be considered round. Therefore, the radiation pattern is round from 1-4 [GHz] and at 6 [GHz] for the horn with an arc depth of $L/6$, whereas the radiation patten of the standard horn can only be considered round at 6 [GHz].

The illustrate extent of the improvement offered by the arced horns, the difference between the EL's of the standard exponential horn and those of the modified exponential horns is shown in Table 6.5. A negative value indicates an improvement, or how much lower the EL obtained with the arced horn is compared to that of the standard exponential horn. The extent of the improvement in the EL's using arc depths of $L/4$ and $L/6$ are noteworthy.

Therefore the proposed modification is successful at improving the roundness of the radiation pattern over a wide bandwidth. This indicates that modifying the exponential TEM horn to have an optimum sized convex parabolic arc is successful at achieving a round radiation pattern over a wide bandwidth.

f [GHz]	*std* [dB]	$L/20$ [dB]	$L/12$ [dB]	$L/10$ [dB]	$L/8$ [dB]	$L/6$ [dB]	$L/4$ [dB]
1	-2.3	-2.3	-2.5	-2.5	-2.8	-3.2	-1.7
2	-2.5	-4.4	-5.4	-6.6	-7.5	-7.0	-0.8
3	-0.5	-0.06	-0.4	-2.3	-3.6	-5.7	-5.2
4	-2.2	-1.9	-0.3	-0.7	-0.8	-3.0	-7.0
5	-2.9	-2.8	-3.0	-2.4	-0.7	-1.8	-6.1
6	-3.0	-3.6	-2.9	-3.3	-3.0	-3.8	-4.6

Table 6.4: Equal Levels for the exponential TEM horn with a parabolic arc at various arc depths and frequencies compared to those of the standard exponential horn

From the results in this section, it is concluded that the arc depth of an exponential TEM horn with a convex parabolic arc has an influence on the roundness of the radiation pattern and can be optimised to yield a rounder pattern over a wider bandwidth than the standard exponential TEM horn.

6.2.3 Triangular Arc

This section repeats the analysis done in Section 6.2.2 for an exponential TEM horn with a convex *triangular* arc. The width profile (top view) of the antenna is shown in Figure 6.13 and it has the

f [GHz]	$L/20$ [dB]	$L/12$ [dB]	$L/10$ [dB]	$L/8$ [dB]	$L/6$ [dB]	$L/4$ [dB]
1	0	-0.2	-0.2	-0.5	-0.9	0.6
2	-0.9	-2.9	-4.1	-5.0	-4.5	1.7
3	0.44	0.1	-1.8	-3.1	-5.2	-4.7
4	0.3	1.9	1.5	1.4	-0.8	-4.8
5	0.1	-0.1	0.5	2.2	1.1	-3.2
6	-0.6	0.1	-0.3	0	-0.8	-1.6

Table 6.5: Difference between the **Equal Levels** of the standard exponential TEM horn and the exponential TEM horn with the parabolic arcs. A negative value indicates an improvement.

same length ($L = 1.8\lambda$) as the standard exponential horn and exponential horn with the convex parabolic arc. As before, a parallel plate section is added for the feed and is also shown in Figure 6.13. The triangular arc is investigated to determine if other types of convex arcs can be used to improve the roundness of the radiation pattern even more than with the parabolic arc.

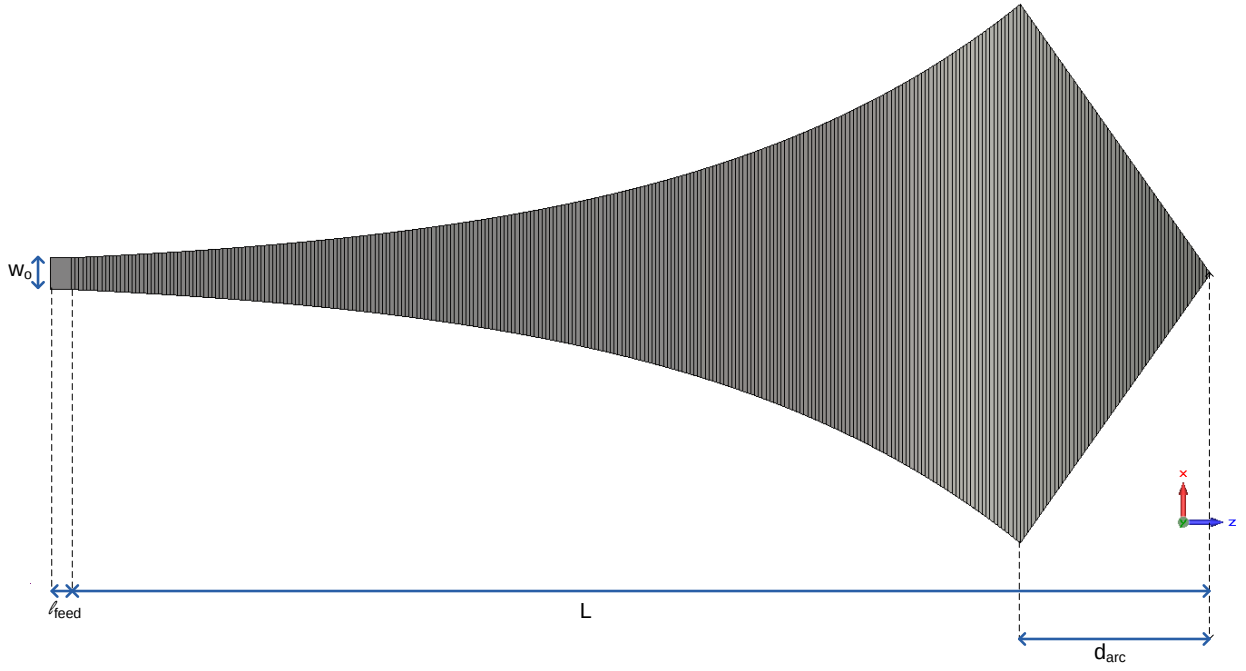

Figure 6.13: Top view of an exponential TEM horn with a convex triangular arc and parallel plate feed section

The nominal parameter values for the exponential horn with convex triangular arc are shown in Figure 6.6. As before, the arc depth is varied from $L/20$ to $L/4$ and the **difference** between the E- and H-plane electric farfield patterns is calculated for each antenna as shown in Figures 6.14-6.16. The results are very similar to those achieved with the convex parabolic arc, with the improvement in the difference functions extending to the higher frequencies as the arc depth is increased.

L [λ]	d_o [mm]	w_o [mm]	d_L [λ]	w_L [λ]	$feed_l$ [mm]	d_{arc}
1.8	3.98	30	1.5	d_L	10	$L/20$

Table 6.6: Nominal parameter values for the shortened exponential horn with a convex triangular arc

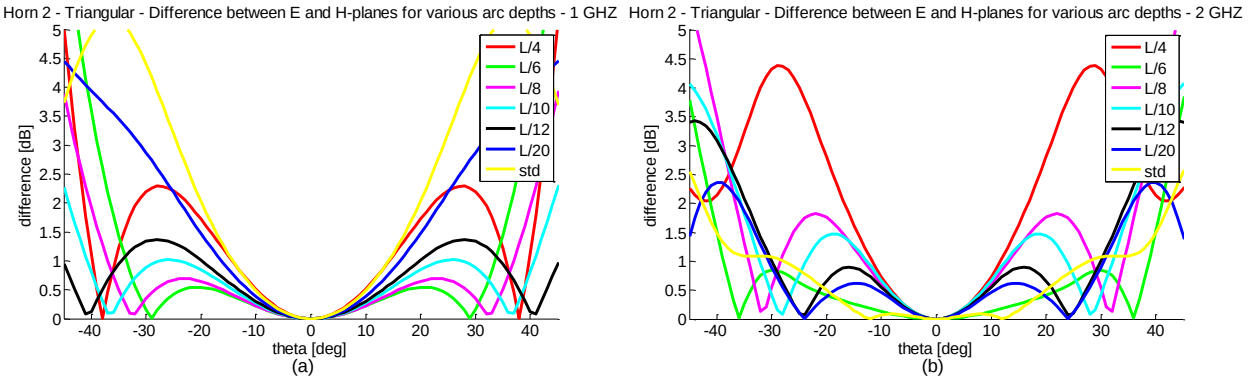

Figure 6.14: Difference between the E- and H-plane directivity for various arc depths for exponential TEM horn with a convex triangular arc: (a) 1 [GHz] (b) 2 [GHz]

Figures 6.14-6.16 show the difference between the E- an H-plane electric farfield patterns for an exponential TEM horn with a triangular arc for different arc depths from 1 to 6 [GHz].

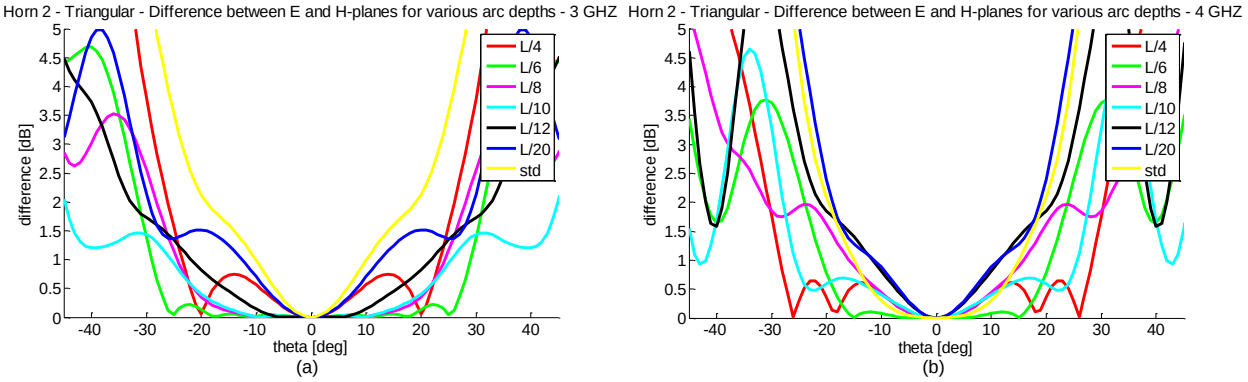

Figure 6.15: Difference between the E- and H-plane directivity for various arc depths for exponential TEM horn with a convex triangular arc: (a) 3 [GHz] (b) 4 [GHz]

As in the previous section, the one-sided angular ranges (θ_{1dB}) and EL's are calculated for each arc depth and provided in Tables 6.7 and 6.8, respectively. The difference between the EL's of the arced horns and standard horn are also shown in Table 6.9, with a negative value indicating an improvement. All values that are highlighted in blue indicate values that are equal to, or an improvement on those of the standard exponential TEM horn.

The outcomes of the investigation are similar to those for the convex parabolic arc and are summarised as follows:

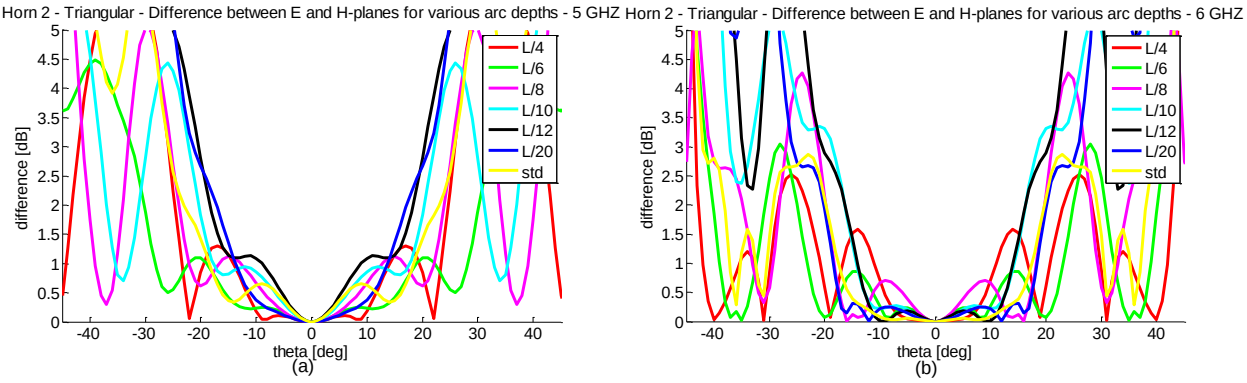

Figure 6.16: Difference between the E- and H-plane directivity for various arc depths for exponential TEM horn with a convex triangular arc: (a) 5 [GHz] (b) 6 [GHz]

f [GHz]	θ_{std} [°]	$\theta_{L/20}$ [°]	$\theta_{L/12}$ [°]	$\theta_{L/10}$ [°]	$\theta_{L/8}$ [°]	$\theta_{L/6}$ [°]	$\theta_{L/4}$ [°]
1	-14.2	-16.3	-19.8	-40.8	-37	-33.6	-14.3
2	-27.8	-30.5	-30	-12.7	-13.2	-38.8	-11.7
3	-10.1	-12.6	-21.8	-25.5	-24.3	-29	-23.4
4	-15	-11.3	-11.6	-25.6	-15.9	-20.8	-28.4
5	-18.4	-13.7	-8.9	-17.6	-12.8	-19	-14.1
6	-17.5	-18.4	-14.1	-14.3	-18.3	-23.2	-11

Table 6.7: $-\theta_{1dB}$ for the exponential TEM horn with a convex triangular arc at various arc depths and frequencies compared to those of the standard exponential TEM horn

f [GHz]	*std* [dB]	$L/20$ [dB]	$L/12$ [dB]	$L/10$ [dB]	$L/8$ [dB]	$L/6$ [dB]	$L/4$ [dB]
1	-2.3	-2.5	-2.8	-7.0	-4.7	-4.3	-1.7
2	-2.5	-4.1	-6.0	-3.3	-3.2	-9.3	-0.5
3	-0.5	-0.02	-1.4	-3.5	-4.3	-7.1	-6.5
4	-2.2	-1.1	-0.1	-4.4	-0.6	-3.6	-9.4
5	-2.9	-2.7	-1.4	-2.6	-0.5	-2	-5.1
6	-3.0	-3.6	-2.8	-3.4	-2.9	-4.7	-3.2

Table 6.8: Equal Levels for the exponential TEM horn with a convex triangular arc at various arc depths and frequencies compared to those of the standard exponential TEM horn

- The arc depth has an influence on the frequency at which an improvement in the roundness of the pattern is seen, both in terms of angular range and EL's.
- The smaller arcs offer an improvement at the lower end of the frequency range.
- As the arc depth increases, an improvement in the roundness of the directivity is extended to

the higher frequencies and over a wider bandwidth.

- If the arc depth becomes too large, the improvement at the lower frequencies disappears as the dimensions of the antenna are changed to such an extent that the lower frequencies do not break away from the antenna. This is seen from the results in the last columns of Tables 6.7 and 6.8 for an arc depth of $L/4$.
- Although there is no improvement in the angular range at 5 and 6 [GHz] with an arc depth of $L/4$, there is an improvement in the EL at 6 [GHz] as for the parabolic arc.
- Once again, an arc depth of $L/6$ offered the best overall improvement at the largest number of frequencies, improving the EL by -6.8 [dB] at 2 [GHz] and -6.6 [dB] at 3 [GHz].
- The EL's obtained with the exponential horn with a triangular arc of depth $L/6$ are all below -3 [dB] at 1-4 [GHz] and 6 [GHz] and are even lower than those achieved with the equivalent parabolic arc.

f [GHz]	$L/20$ [dB]	$L/12$ [dB]	$L/10$ [dB]	$L/8$ [dB]	$L/6$ [dB]	$L/4$ [dB]
1	-0.2	-0.5	-4.7	-2.4	-2.0	0.6
2	-1.6	-3.5	-0.8	-0.7	-6.8	2.0
3	0.48	-0.9	-3.0	-3.8	-6.6	-6.0
4	1.1	2.1	-2.2	1.6	-1.4	-7.2
5	0.2	1.5	0.3	2.4	0.9	-2.2
6	-0.6	0.12	-0.4	0.1	-1.7	-0.2

Table 6.9: Difference between the **Equal Levels** of the standard exponential TEM horn and the exponential TEM horn with the convex triangular arcs. A negative value indicates an improvement.

6.2.4 Conclusion

The results discussed in this section show than an improvement in the roundness of the electric farfield pattern can be achieved by optimising the arc depth of a modified exponential TEM horn which has a convex triangular or convex parabolic arc. For both types of arcs, an arc depth of $L/6$ offered some of the lowest EL's and widest angular ranges, improving the EL at 5 out of the 6 sample frequencies. The triangular arc was found improve the roundness of the radiation pattern even more than the parabolic arc, specifically when comparing the antennas with arc depths of $L/6$. Based on the results of the investigation it is decided to construct the exponential TEM horn with a convex triangular arc, with a total antenna length of $L = 1.8\lambda$ with an arc depth of $d_{arc} = L/6$.

.

6.2.5 Antenna to be Constructed

The antenna chosen for construction and for measurement is the exponential TEM horn with a convex parabolic arc, with dimensions:

- $L = 1.8\lambda$ at 1 [GHz]
- $d_{arc} = L/6$
- $d_o = 3.98$ [mm]
- $w_o = 30$ [mm]
- $feed_l = 10$ [mm]

To determine how much of the input signal is reflected back to Port 1, the magnitude of s_{11} is calculated (in [dB]) using CST and is shown in Figure 6.17. An ideal waveguide port is used in the simulation to excite the antenna.

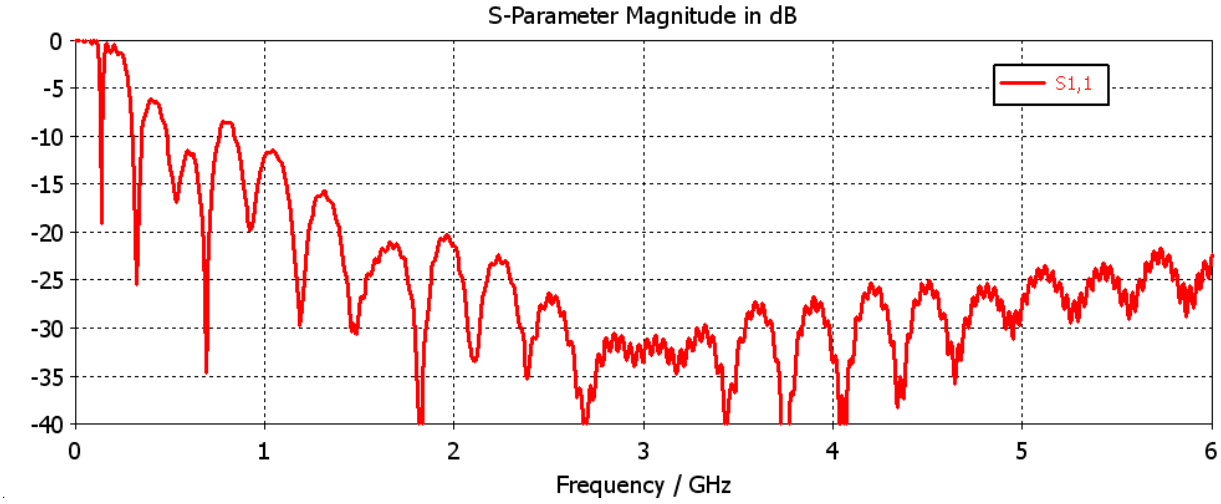

Figure 6.17: $|s_{11}|$ in [dB] for the exponential TEM horn with triangular arc. $L = 1.8\lambda$, $d_{arc} = L/6$, $d_o = 4$ [mm] and $w_o = 30[mm]$

Ideally $|s_{11}|_{dB} \rightarrow -\infty$ if all input power is transmitted. However, this is impossible to achieve in practice and $|s_{11}| \leq -10[dB]$ over the bandwidth is sufficiently low for the purposes of this thesis. Figure 6.17 shows that the -10 [dB] bandwidth of the exponential TEM horn with $L/6$ triangular arc is from 0.8-6 [GHz]. As is expected of TEM horns, the bandwidth achieved with the antenna is very good.

6.3 Wideband Feed

The antenna is to be fed using a 50 [Ω] SMA connector (coaxial cable) which is mounted on the structure so that the center conductor (or pin) of the SMA transfers the input energy from the coaxial cable to the TEM waveguide antenna.

The SMA connector is modelled in CST by a center conductor or pin with a radius $r_{pin} = 0.64$ [mm] and an insulating layer of Teflon with $\epsilon_r = 2.2$ outer radius $r_{teflon} = 2.05$ [mm] such as shown in Figure 6.18. The outside of the dielectric is coated with a thin layer of PEC for simulation purposes which is given an outer radius $r_{oo} = 2.55$ [mm].

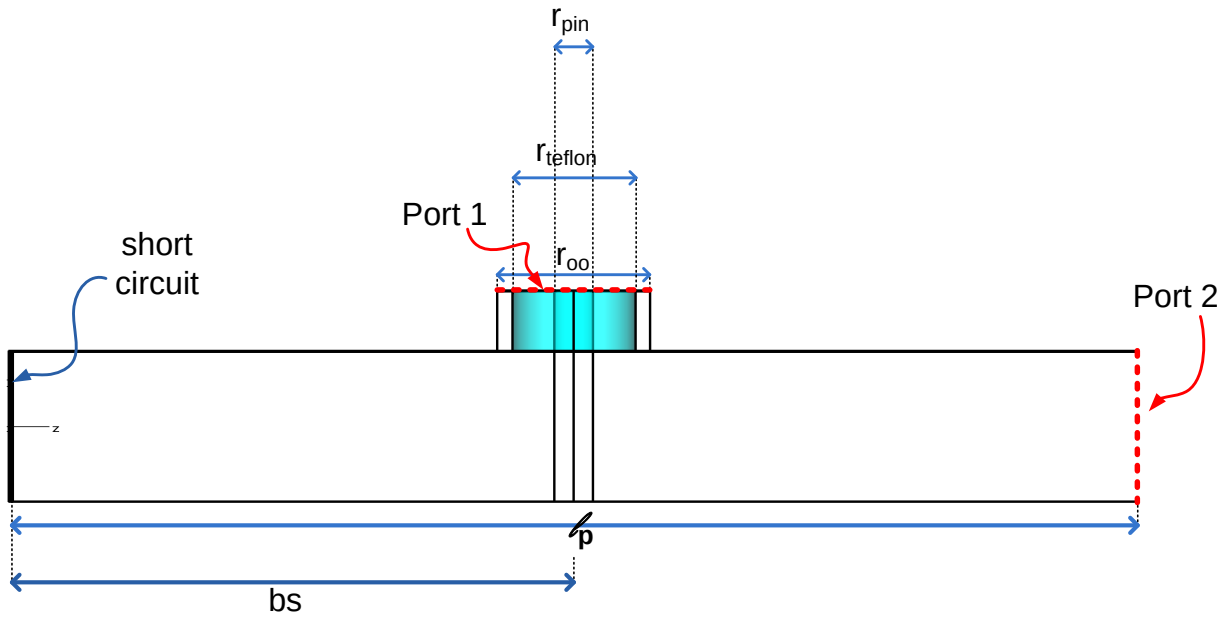

Figure 6.18: Side view of parallel plate feed configuration

The most basic configuration used to transfer the energy from the SMA connector to the antenna is shown in Figure 6.18. The feed in Figure 6.18 consists a parallel plate section, a short circuit and an SMA input with nominal parameter values indicated in Table 6.10. The center conductor or pin of the SMA connector is placed parallel to the vertically orientated electric fields in the waveguide, allowing the azimuthal fields produced by the center conductor to couple with the TEM H-fields. The parallel plate is terminated in a short-circuit at $z = l_p$ and the pin of the SMA connector is positioned a distance b_s from the short. Port 1 indicates the SMA input port and Port 2 is where the feed will be connected to the antenna. Ideally, no power should be reflected back into Port 1 and $|s_{11}|$ should be less than -15 [dB] over the entire bandwidth so that the feed does not decrease the performance of the antenna.

For maximum power transfer, the input reflection coefficient must be equal to 1 when looking towards the short-circuit from Port 1. This implies that the short-circuit is transformed to an open-

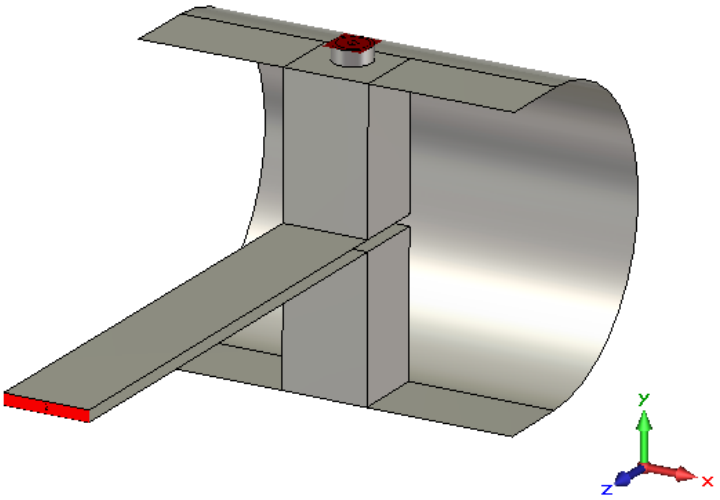

Figure 6.19: Wideband feed configuration [8]

circuit over the distance b_s.

d_o [mm]	w_o [mm]	l_p [mm]	bs [mm]	r_{pin} [mm]	r_{teflon} [mm]	r_{oo} [mm]
1.5	11.3	75	37.5	0.64	2.05	2.55

Table 6.10: Nominal parameter values of the parallel plate feed configuration

As discussed in [2], b_s can be optimised to transform the short-circuit to an open-circuit over a distance of $\lambda/4$. However, the short-circuit will only be transformed to an open-circuit at a single frequency resulting in a narrow-band structure. Figure 6.20 shows that varying b_s simply shifts the local minima of $|s_{11}|$, with the -15 [dB] bandwidth never exceeding 1.5 [GHz]. This illustrates that this configuration cannot yield a wideband feed and an alternative must be found.

Therefore, it is decided to make use the feed structure in [8] which has the configuration shown in Figure 6.19. A wideband open-circuit is achieved by adding a circular cavity at the back of the plates. The front view of the feed configuration is shown in Figure 6.21 and its side and top views are shown in Figure 6.22. The SMA connector/coaxial cable input is modelled in CST in the same way as in Figure 6.18 and its dimensions and materials are those of a typical 50 [Ω] SMA connector:

- r_{pin} = 0.64 [mm] - PEC
- r_{teflon} = 2.05 [mm] with ϵ_r = 2.2

Parameter values such as the cavity radius and SMA pin position are optimised to achieve a wideband feed. The plate separation (d_o) and width (w_o) are also varied (whilst keeping Z_o = 50 [Ω] using Equation 6.1) to determine their influence on s_{11}. The nominal values of the parameters

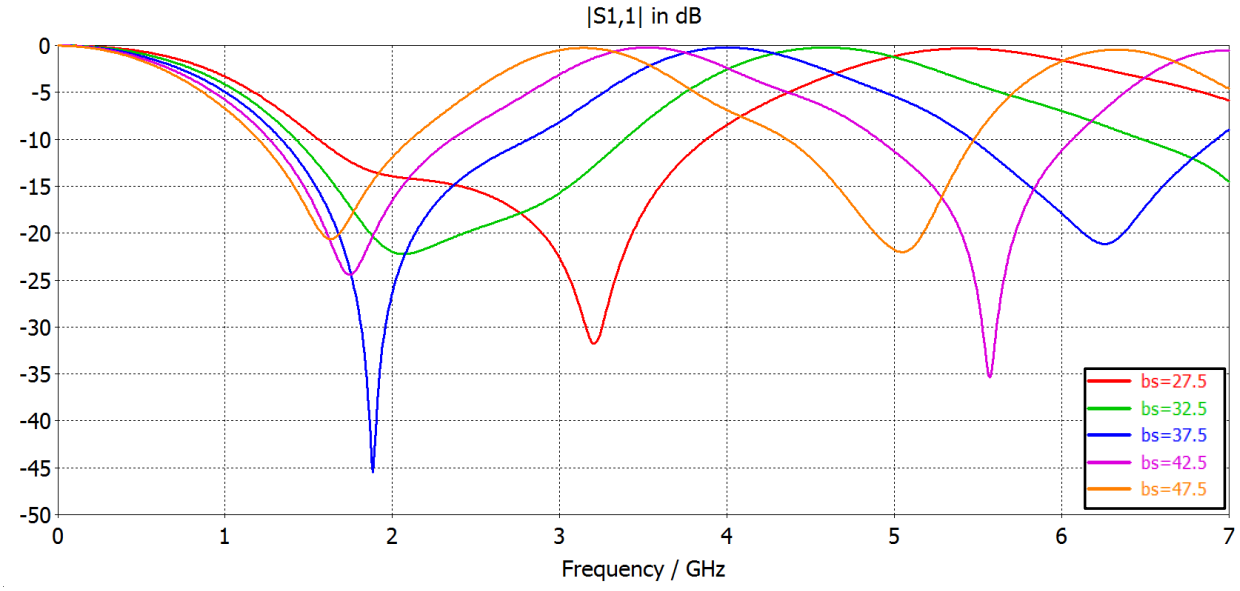

Figure 6.20: $|s_{11}|$ achieved with the parallel plate feed for various values of b_s

indicated in Figures 6.21-6.22 are supplied in Table 6.11. The length of the parallel plate is chosen as $\lambda/4 = 75$ [mm] at 1 [GHz]. The radius of the short circuit arc section (r_s) is chosen to be 30 [mm] so that the maximum distance from the short to the pin is close to a quarter wavelength at 2 [GHz]. This is done so that the center frequency is still closer to the lower frequency range where it is the most difficult to achieve a low $|s_{11}|$.

Figure 6.23 shows $|s_{11}|$ in [dB] for three sets of parallel plate dimensions (in [mm]) yielding $Z_o = 50$ [Ω]. The -10 [dB] bandwidth increases as d_o is decreased, with a 4 [GHz] bandwidth achieved for $d_o = 1.5, w_o = 11.3$ [mm]. This is a 2.5 [GHz] increase in the bandwidth offered by the simple parallel plate configuration. Therefore, the values of $d_o = 1.5$ [mm] and $w_o = 11.3$ [mm] are chosen for the wideband feed.

The other dimensions which are chosen for optimisation are, the radius of the short circuit arc r_s and the distance *del* which affects the distance between the SMA pin and the end of the parallel plate section and obviously the distance d_{SMA}.

l	l_r	r_s	w_o	d_o	r_{pin}	r_{teflon}	r_{oo}	del	d_p	w_f	d_{SMA}
75	10	30	11.3	1.5	0.64	2.05	2.55	1.5	4.05	50	0.5+*del*

Table 6.11: Nominal parameter values of the wideband feed shown in Figures 6.19-6.22. All dimensions are in [mm].

Influence of Short Radius (r_s) on $|s_{11}|$ Figure 6.24 shows how the magnitude of the radius of the short circuit arc influences $|s_{11}|$. The smaller the arc is, the better the performance at the higher

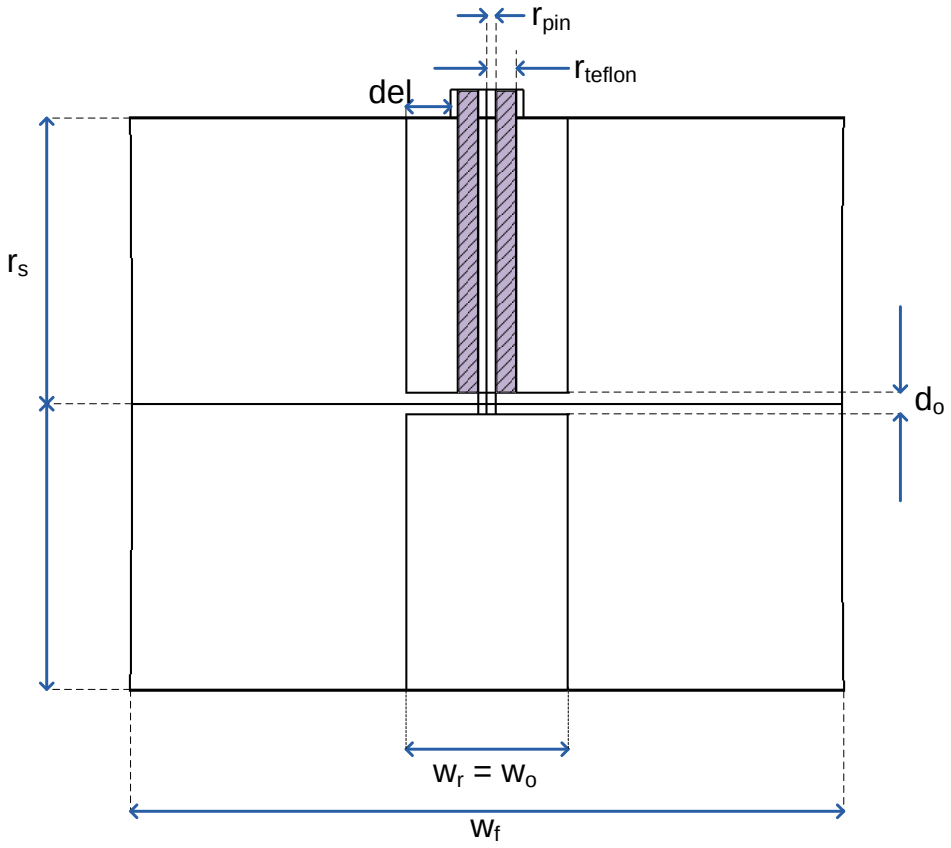

Figure 6.21: Front view of the wideband feed

frequencies, with s_{11} falling below -20 [dB] from about 2.6 to 6 [GHz]. However a value of 20 [mm] is chosen for r_s since $|s_{11}|$ for this value falls below -15 [dB] at a slightly lower frequency than when r_s is 15 [mm]. This is desired since the lower frequency range is important for the SKA.

Influence of Pin Position on $|s_{11}|$ The value of r_s is adjusted to be 20 [mm] whilst keeping the other dimensions in Table 6.11 the same.

The pin should be as close as possible to the end of the parallel plate section at $z = -l$. However, due to manufacturing limitations the value of *del* cannot be less than 1.15 [mm]. Therefore, *del* from 1.75 [mm] to a minimum value of 1.15 [mm] as shown in Figure 6.25. There is little change at the lower frequencies, but decreasing *del* to 1.15 [mm] lowers $|s_{11}|$ by a couple of [dB] between 5 and 6 [GHz]. Therefore, the value of *del* is changed to 1.15 [mm], making $d_{SMA} = 1.65$ [mm] and $d_{pin} = 3.7$ [mm].

Optimisation A final optimisation is done by varying *rs* from 19 to 21 [mm] as shown in Figure 6.26. A final value of 19 [mm] is chosen for r_s as it further decreases $|s_{11}|$ at the higher frequencies without decreasing the low frequency performance. The final -15 [dB] bandwidth of the feed is 5.2 [GHz] from 0.8-6 [GHz].

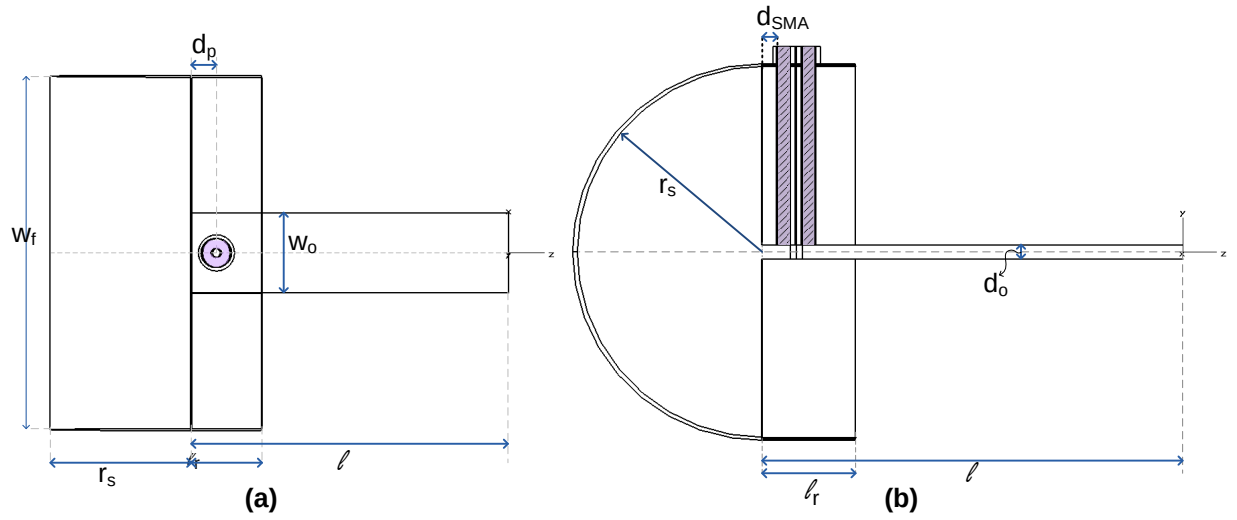

Figure 6.22: (a) Top and (b) side view of the wideband feed.

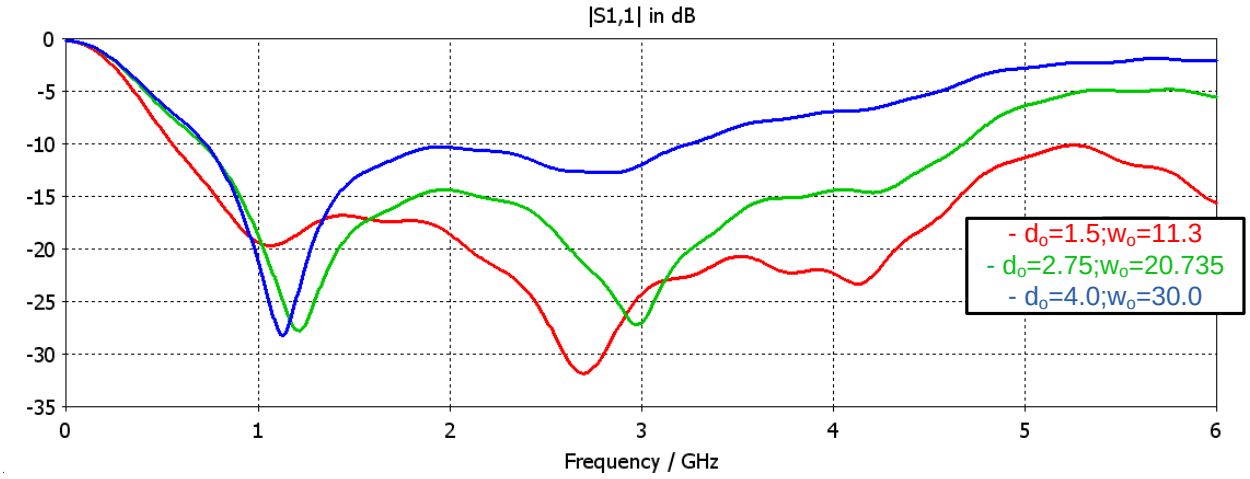

Figure 6.23: $|s_{11}|$ in [dB] for various sets of parallel plate dimensions which yield $Z_o = 50$ [Ω].

To avoid designing a stepped matching network for the wideband feed and antenna, the plate separation and width of the antenna are adjusted to $d_o = 1.5$ [mm] and $w_o = 11.3$ [mm]. As before, the s-parameters of the antenna are calculated using a waveguide port and shown in Figure 6.27.

Although there is a slight decrease in the performance of the antenna in terms of s_{11}, the -10 [dB] bandwidth is virtually unchanged. The antenna and its wideband feed are analysed as a system in the next section.

6.3.1 Finalised Antenna Simulations

Figure 6.28 shows the exponential TEM horn with triangular arc together with its wideband feed which is to be constructed and measured. The final parameter values of the antenna and those its feed (as defined in previous sections) are shown in Tables 6.12.

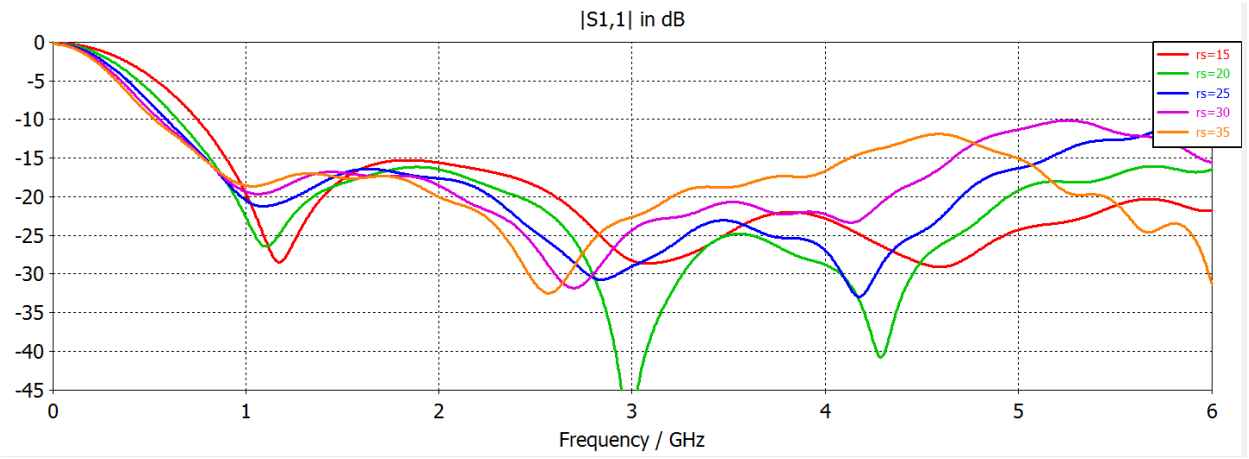

Figure 6.24: $|s_{11}|$ of wideband feed for various values of r_s

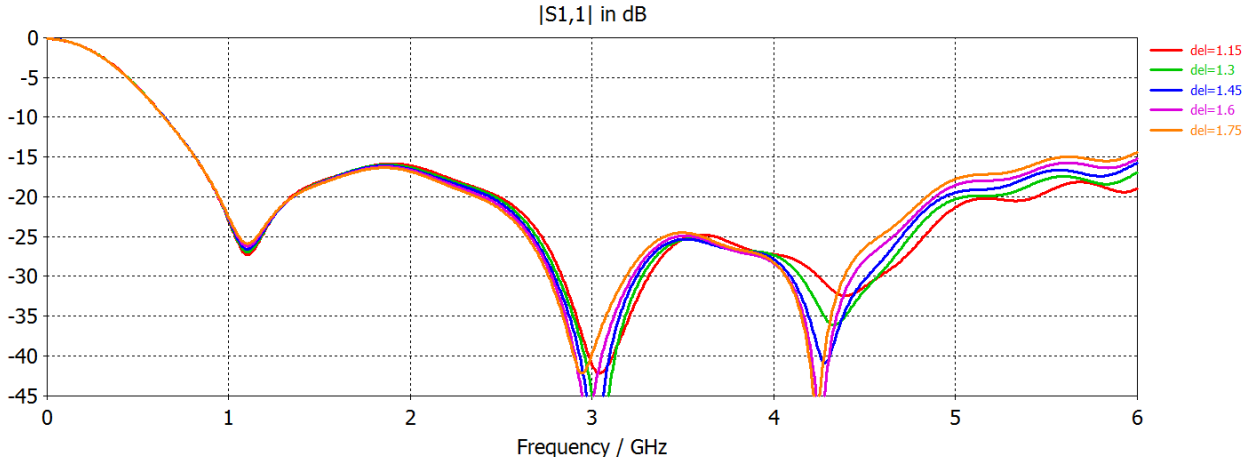

Figure 6.25: $|s_{11}|$ in [dB] for various values of *del*.

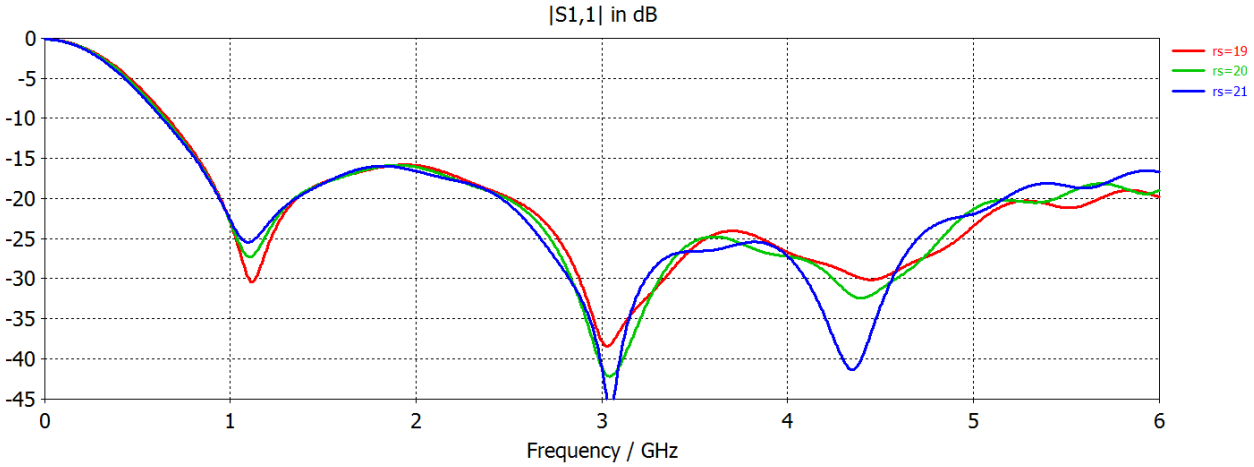

Figure 6.26: Final optimisation of radius of short circuit cavity

A CST simulation is done to obtain $|s_{11}|$ in [dB] for the antenna together with its feed as well

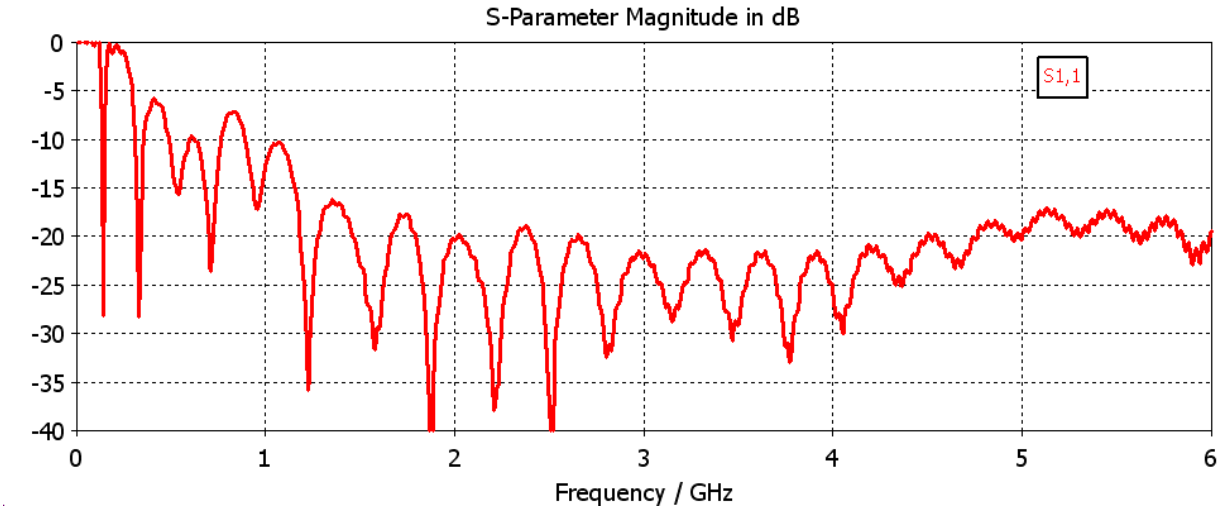

Figure 6.27: $|s_{11}|$ in [dB] for the exponential TEM horn antenna with triangular arc. $L = 1.8\lambda$, $d_{arc} = L/6$, $d_o = 1.5$ [mm] and $w_o = 11.3$ [mm]

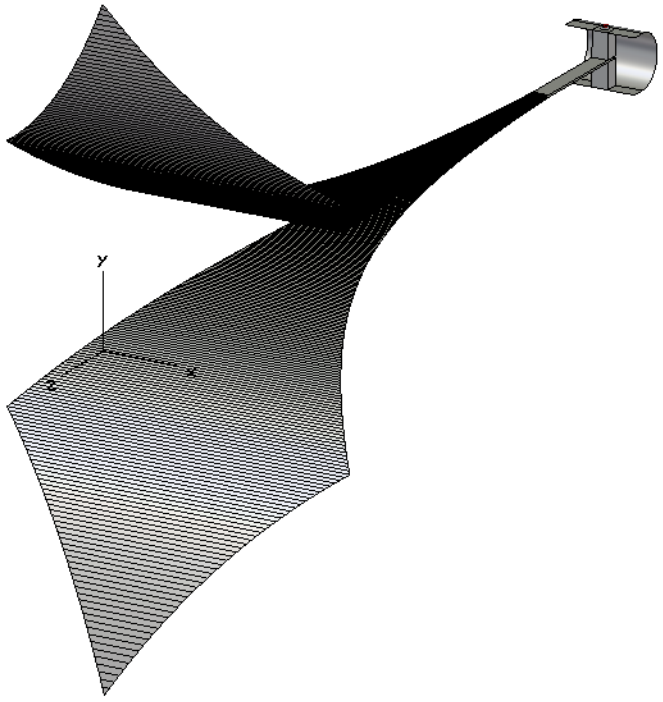

Figure 6.28: Finalised exponential TEM horn antenna with triangular arc and wideband feed section

as the simulated E- and H-plane farfield patterns from 1 to 6 [GHz]. Figure 6.29 shows $|s_{11}|$ over the frequency range for the final antenna and feed, indicating at which frequencies $|s_{11}|$ falls below -10 [dB] or -15 [dB] up to 6 [GHz].

The bandwidth of the antenna, or the range for which $|s_{11}| \leq -10$ [dB], is from 1 - 6 [GHz].

Figures 6.30-6.32 show the E- plane directivity vs the H-plane directivity of the final antenna from 1 to 6 [GHz]. The 1 [dB] angular ranges and equal levels obtained are shown in Table 6.14.

L [λ]	d_o [mm]	w_o [mm]	d_L [λ]	w_L [λ]	$feed_l$ [mm]	d_{arc}
1.8	1.5	11.3	1.5	d_L	10	$L/6$

Table 6.12: Final parameter values for the shortened exponential horn with a convex triangular arc

l	l_r	r_s	w_o	d_o	r_{pin}	r_{teflon}	r_{oo}	del	d_{pin}	w_f	d_{SMA}
75	10	19	11.3	1.5	0.64	2.05	2.55	1.15	4.05	50	0.5+del

Table 6.13: Final parameter values of the wideband feed shown in Figures 6.19-6.22. All dimensions are in [mm].

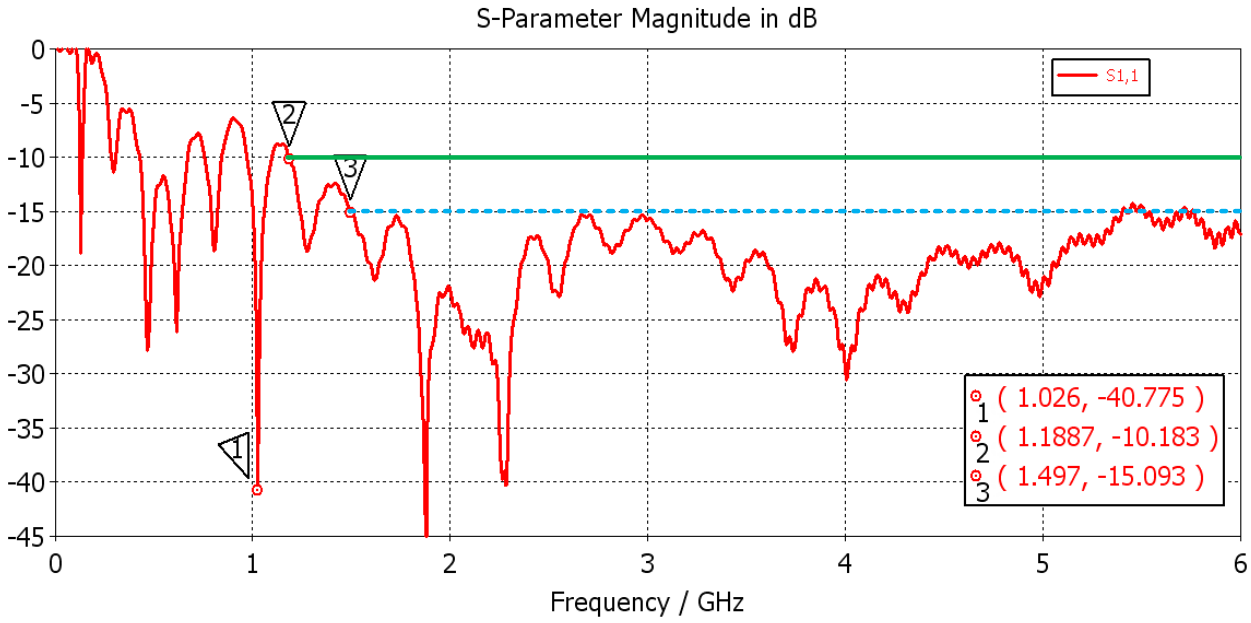

Figure 6.29: $|s_{11}|$ in [dB] for the exponential TEM horn with triangular arc and wideband feed with the dimensions in Tables 6.12 and 6.13

The EL's at 1, 2, 3 and 4 [GHz] are all below the half power (-3 [dB]) level by at least 2.6 [dB]. The most notable result is the EL of -10.4 [dB] at 3 [GHz]. Although the patterns are not considered round at 5 and 6 [GHz], they are still very similar.

The simulated results are compared to the physical antenna measurements in the next section.

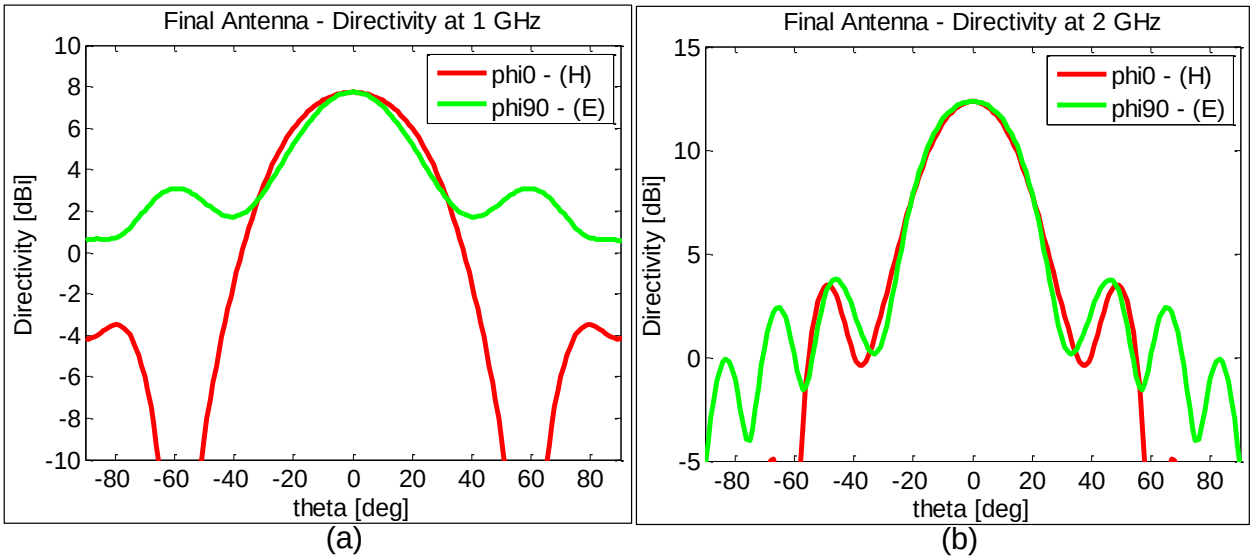

Figure 6.30: E- and H-plane directivity of the final antenna with wideband feed: (a) 1 [GHz] (b) 2 [GHz]

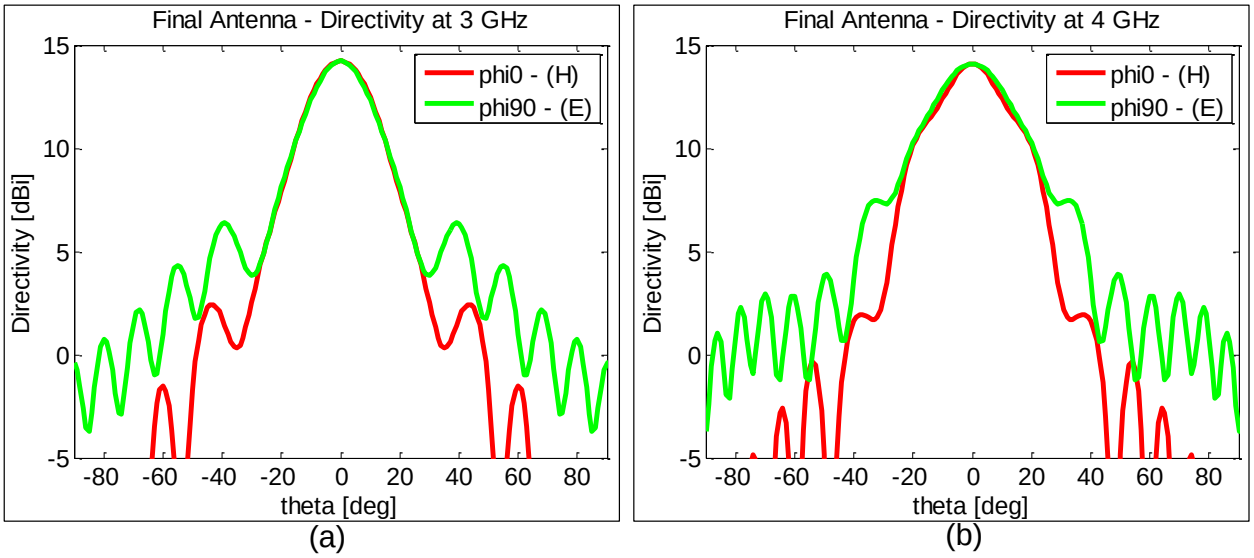

Figure 6.31: E- and H-plane directivity of the final antenna with wideband feed: (a) 3 [GHz] (b) 4 [GHz]

6.4 Construction

The constructed antenna is shown in Figure 6.33. The most cost effective method of construction is chosen and does not provide sufficient structural support for the antenna to maintain symmetry. This negatively influenced the performance of the antenna. Instead of cutting out the antenna and feed system from one solid block of aluminium, it is broken up into the following parts which consist of various materials:

- The antenna plates (including parallel plates of feed) consist of sheet steel.
- The structural support used to ensure plate separation is most clear in Figure 6.33:

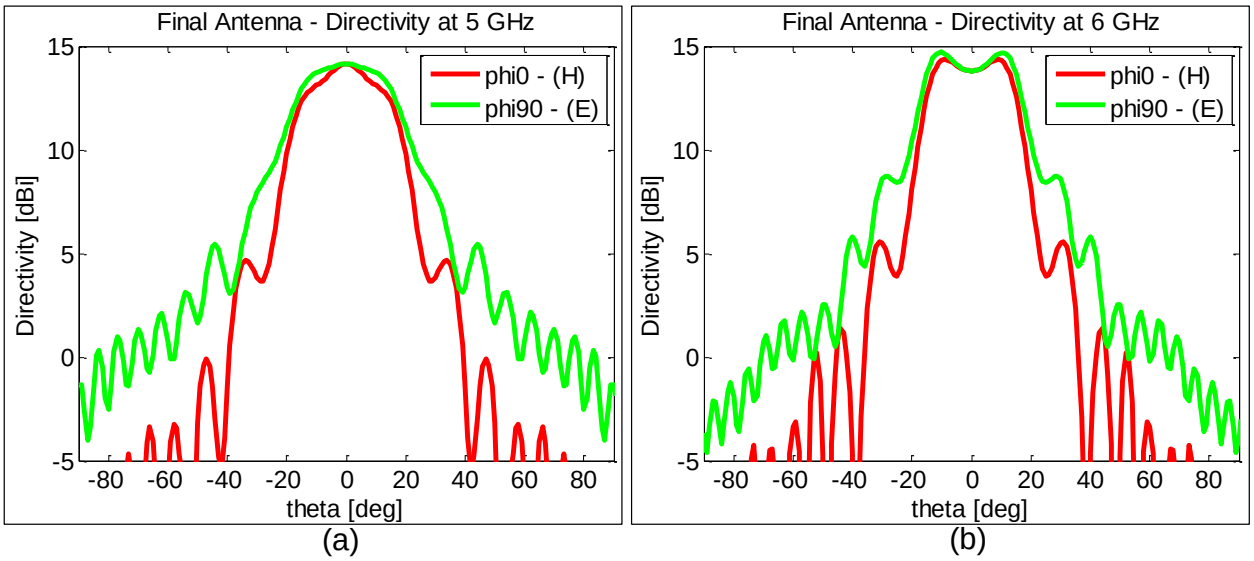

Figure 6.32: E- and H-plane directivity of the final antenna with wideband feed: (a) 5 [GHz] (b) 6 [GHz]

f [GHz]	$-\theta_{1dB}$ [°]	EL [dB]
1	-35.2	-5.6
2	-25.9	-8.6
3	-29.5	-10.4
4	-24.9	-5.84
5	-19	-2.7
6	-14.6	-0.8

Table 6.14: One-sided angular range and EL's achieved with the exponential TEM horn antenna with convex triangular arc and wideband feed with the dimensions in Tables 6.12 and 6.13

Figure 6.33: (a) 3D and (b) side view of the constructed antenna.

– Styrofoam is used in between the antenna plates as well as for standing support below

the bottom plate. Although the structure is relatively well supported when upright, the bottom plate bends away from the foam when it is turned on its side for the measurements. This has a negative influence on the measurement results as discussed in Section 6.5.

  - A flange which consists of sheet steel is used for support for the top antenna plate.

- The feed ridges are made from copper and as shown in Figure 6.35, the top ridge has been modified to form a T-junction so as to mount the SMA connector. The modification is done because the initial size of the ridge is too small to mount the SMA connector.

- Although a female SMA connector is usually used for such purposes, a male SMA connector is used.

- The half-circle short-circuit is constructed from aluminium.

- Initially, a piece of fr_4 is used to ensure the plate separation at the SMA connector end of the feed. However, this decreases the antenna performance, as discussed in Section 6.5, and is removed. The result is that the top plate bends downward (since it was not soldered to the ridge) as shown in Figure 6.35 (c). The effect of this on the measurements is discussed further in Section 6.5

The antenna measurements are discussed in detail in the next section.

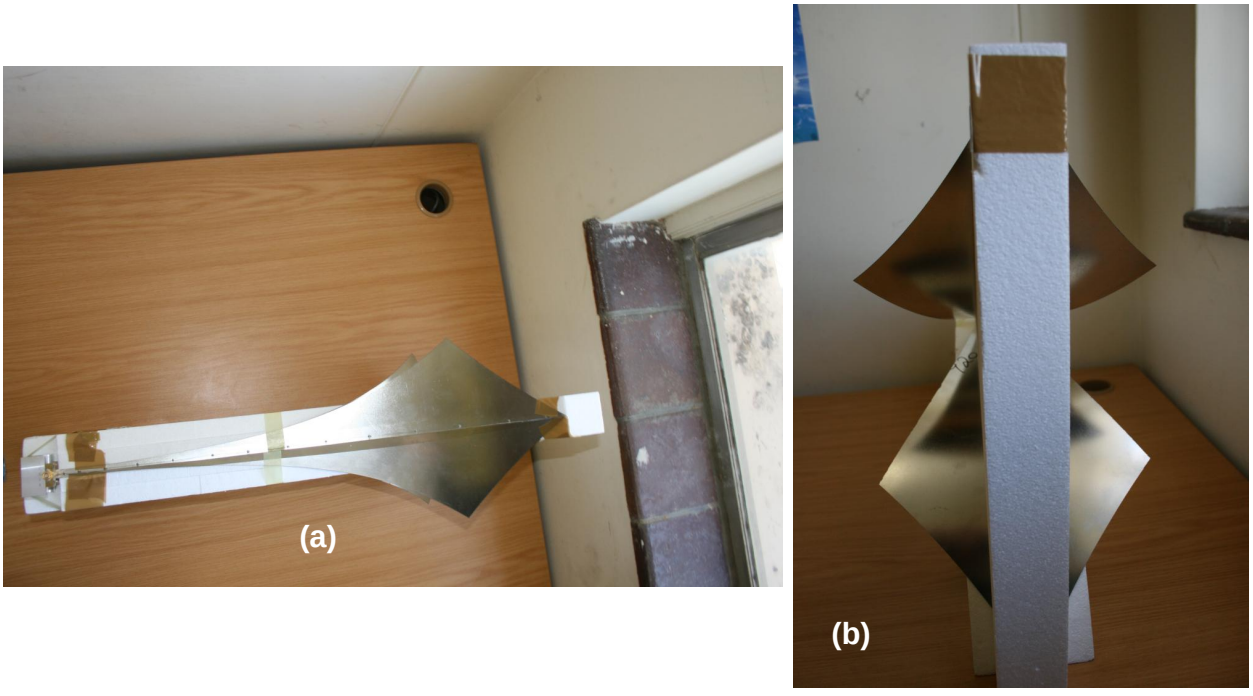

Figure 6.34: (a) Top and (b) front view of the constructed antenna.

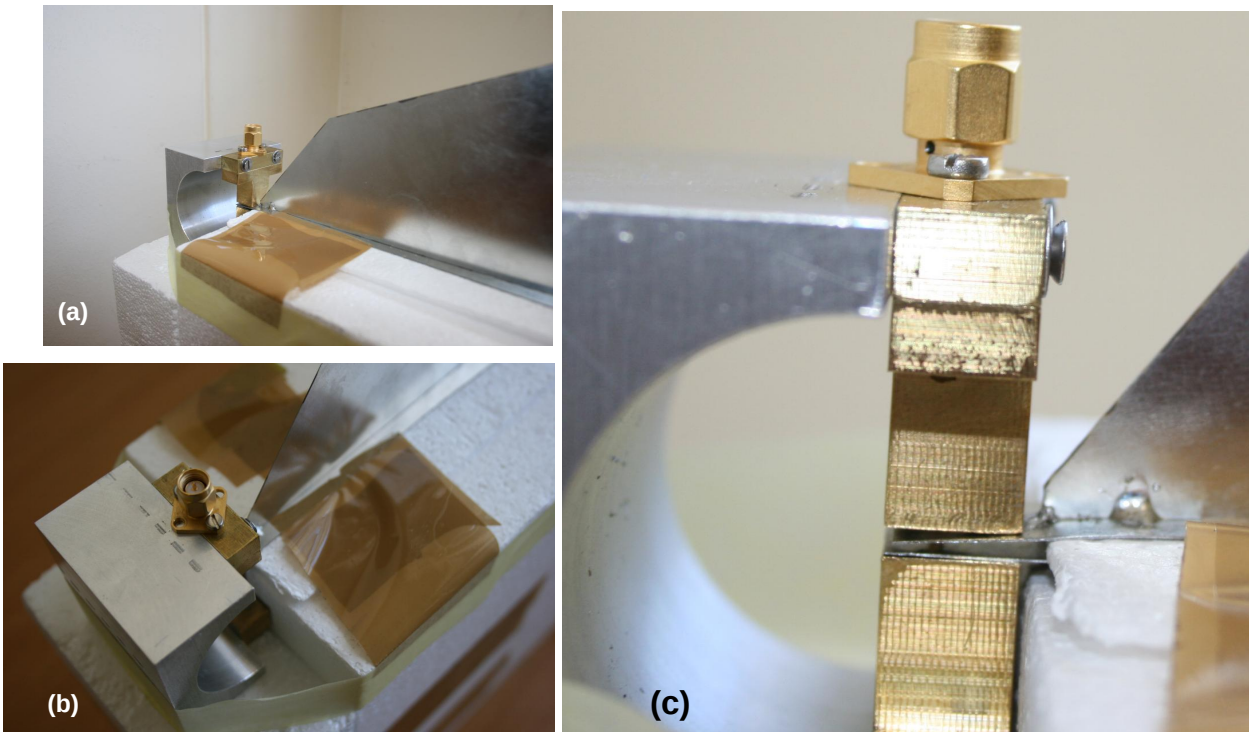

Figure 6.35: 3D (a) front, (b) top and (c) side view of the wideband feed.

6.5 Measurements

The antenna measurements were conducted in the department's anechoic test chamber. The maximum dimension of the antenna aperture (D) is used to calculate the minimum farfield distance (R) required for measurement of the farfield radiation pattern, where [7]

$$R = \frac{2D^2}{\lambda} \tag{6.8}$$

As previously discussed, the antenna is designed to have an aperture height of 1.5λ. Therefore, the minimum distance between the reference antenna and the antenna to be measured is $R = 4.5\lambda = 1.35$ [m], which falls well within the available distance of 5 [m]. The network analyzer is calibrated by using a 5 [m] cable to connect the source and receiver

The first measurement is of s_{11}, including the piece of fr_4 used for plate separation. A second s_{11} measurement is done without the fr_4. The measurement results as well as the simulation results for s_{11} are shown in Figure 6.36. It is clear that the fr_4 significantly decreased the performance of the antenna at the higher frequencies when compared to the simulation results. This is due to the high relative permittivity $\epsilon_r = 4.8$ of fr_4 and the high loss associated with the material. The characteristic impedance of the segment of the parallel plate with the fr_4 is equal to $Z_{fr4} = \frac{Z_o}{\sqrt{\epsilon_r}}$. This causes a mismatch between the impedance of the SMA connector and the parallel plate waveguide. Additional reflections also result from the sharp impedance step at the end of the short section with fr_4.

Therefore, the dielectric between the plates is removed and s_{11} is measured again, yielding s_{11} [no fr_4] shown in Figure 6.36. Although $|s_{11}|$ [no fr_4] is lower than $|s_{11}|$ [fr_4] it is still much higher than the results predicted by the CST simulation. The measurement results indicate that s_{11} increases as frequency increases, instead of decreasing as predicted by the simulation results. The reason for the poor performance of the physical antenna with regard to s_{11} is due to poor construction. The top parallel plate was not fixed to the top feed ridge through which the SMA connector pin runs. As shown in Figure 6.35, this causes the top plate to bend slightly downward or away from the ridge when the fr_4 is removed. This changes the characteristic impedance of the parallel plate causing a mismatch between the SMA port impedance and parallel plate transmission line. The bending of the top plate also makes the feed asymmetric. Both these factors have an influence on s_{11}, with the higher frequencies the most affected by small dimension inaccuracies.

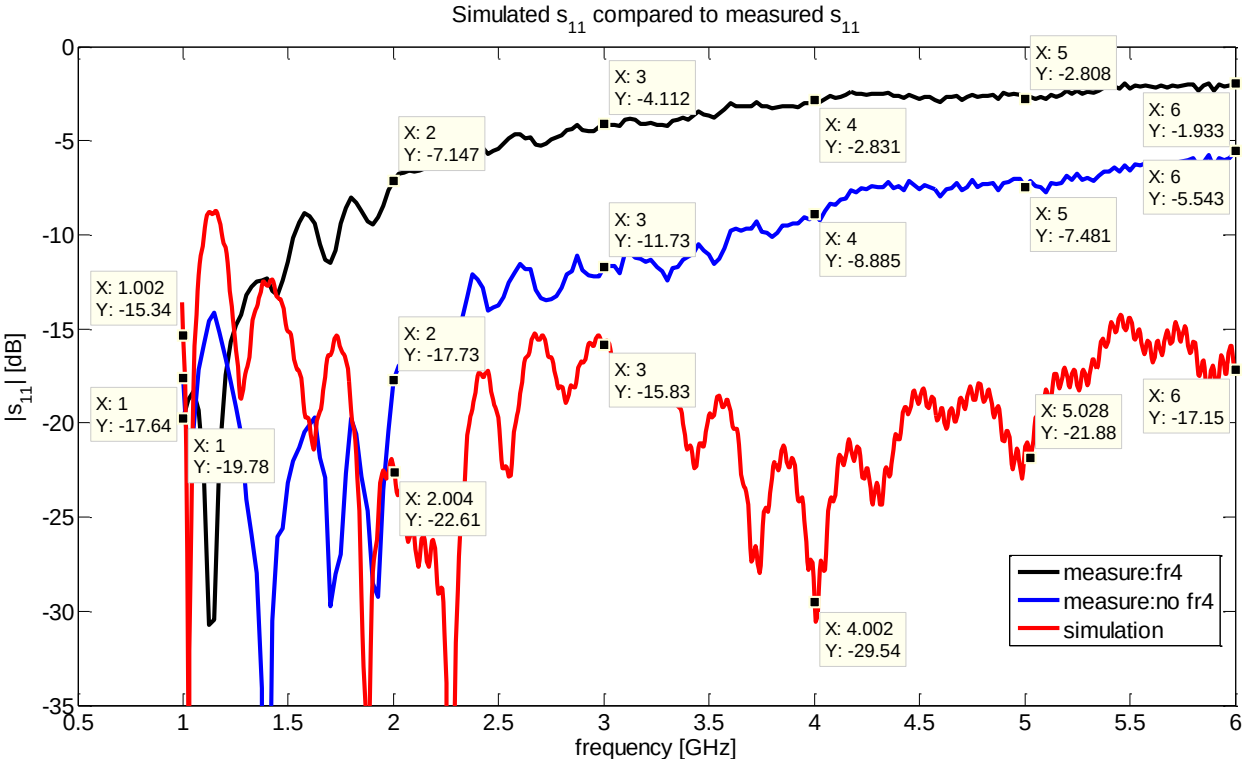

Figure 6.36: s_{11} measurement results compared to simulation results.

The E- and H-plane farfield patterns of the antenna are measured by setting up a transmit and receiver antenna configuration in the anechoic chamber. The system is set up as shown in Figure 6.37, with T_x the transmit antenna (modified exponential TEM horn) and R_x the receive antenna (log periodic dipole antenna - KLPDA4) with known gain. The H-plane is measured by mounting the T_x antenna upright and rotating it horizontally by $+180$ [^{o}] and -180 [^{o}], yielding s_{21H}. The E-plane is measured by placing the antenna on its side with the aperture facing the reference antenna, and rotating it horizontally to yield s_{21E}. The data s_{21H} and s_{21E} provide the shape of the radiation

pattern but do not give the maximum gain or directivity. The maximum directivity is calculated using the Friis Equation [16] defined below:

$$|s_{21}|^2 = \frac{G_{Rx}G_{Tx}\lambda^2}{(4\pi R)^2}(1 - |s_{11Rx}|^2)(1 - |s_{11Tx}|^2) \tag{6.9}$$

The terms, $(1 - |s_{11Rx}|^2)$ and $(1 - |s_{11Tx}|^2)$ account for the input impedance mismatches of the receive and transmit antennas, respectively. The magnitude of s_{11Rx} is considered sufficiently small to be ignored and the term $(1 - |s_{11Rx}|^2)$ is set equal to 1 in Equation 6.9.

Since the reference cable is included for calibration but removed for the measurements, the LHS of Equation 6.9 must be multiplied by $|s_{21cable}|^2$. This is done because removing the cable during measurement (or removing the loss which has been already accounted for) means the calculated gain will be artificially high. Therefore, the cable loss is factored into the Friis Equation so that,

$$|s_{21}|^2|s_{21cable}|^2 = \frac{G_{Rx}G_{Tx}\lambda^2}{(4\pi R)^2}(1 - |s_{11Rx}|^2)(1 - |s_{11Tx}|^2) \tag{6.10}$$

The maximum directivity (equivalent to gain here) is calculated and the measurement results are compared to the simulation results in Figures 6.38-6.43.

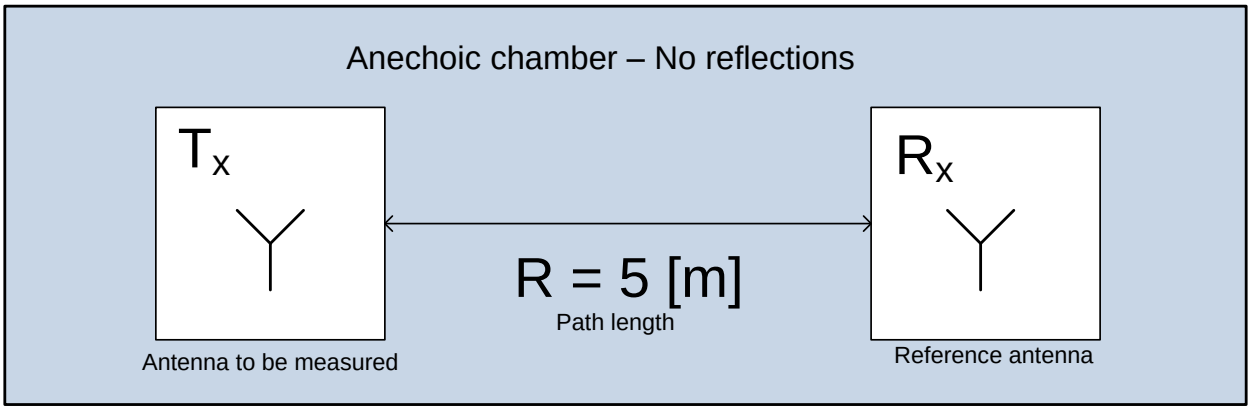

Figure 6.37: Transmit and receive antennas are set up to measure the E- and H-plane farfield patterns of the transmit antenna.

The H-plane measurement and simulation results are compared in Figure 6.38, whereas the E-plane results are compared in Figure 6.39. The H-plane data compares well, with the slight differences attributed to construction flaws. The E-plane measurement results do not compare as well to the simulation data as the H-plane measurements. The E-plane measurement patterns are asymmetrical since the antenna is placed on its side for the measurement of the E-plane, which resulted in the foam separating from the bottom antenna plate. This makes the antenna asymmetrical and results in the asymmetrical E-plane patterns. However, it is clear that apart from the asymmetrical appearance, the measurements and simulation results compare well and that if the antenna

is constructed to maintain symmetry, it would perform as predicted by the simulation results. Although more expensive, it is recommended that the structure must be cut from a solid block of metal as the foam and flange do not provide sufficient support to keep the structure symmetrical for the measurements.

The method of construction used is not ideal for outdoor use as the antenna would be flimsy and fragile to elements such as wind and rain. Even if only the feed section and half the length of the antenna is constructed from solid metal while using thin sheets for the antenna half towards the aperture, the structure would be much better supported and less expensive than when cutting the entire antenna out of metal.

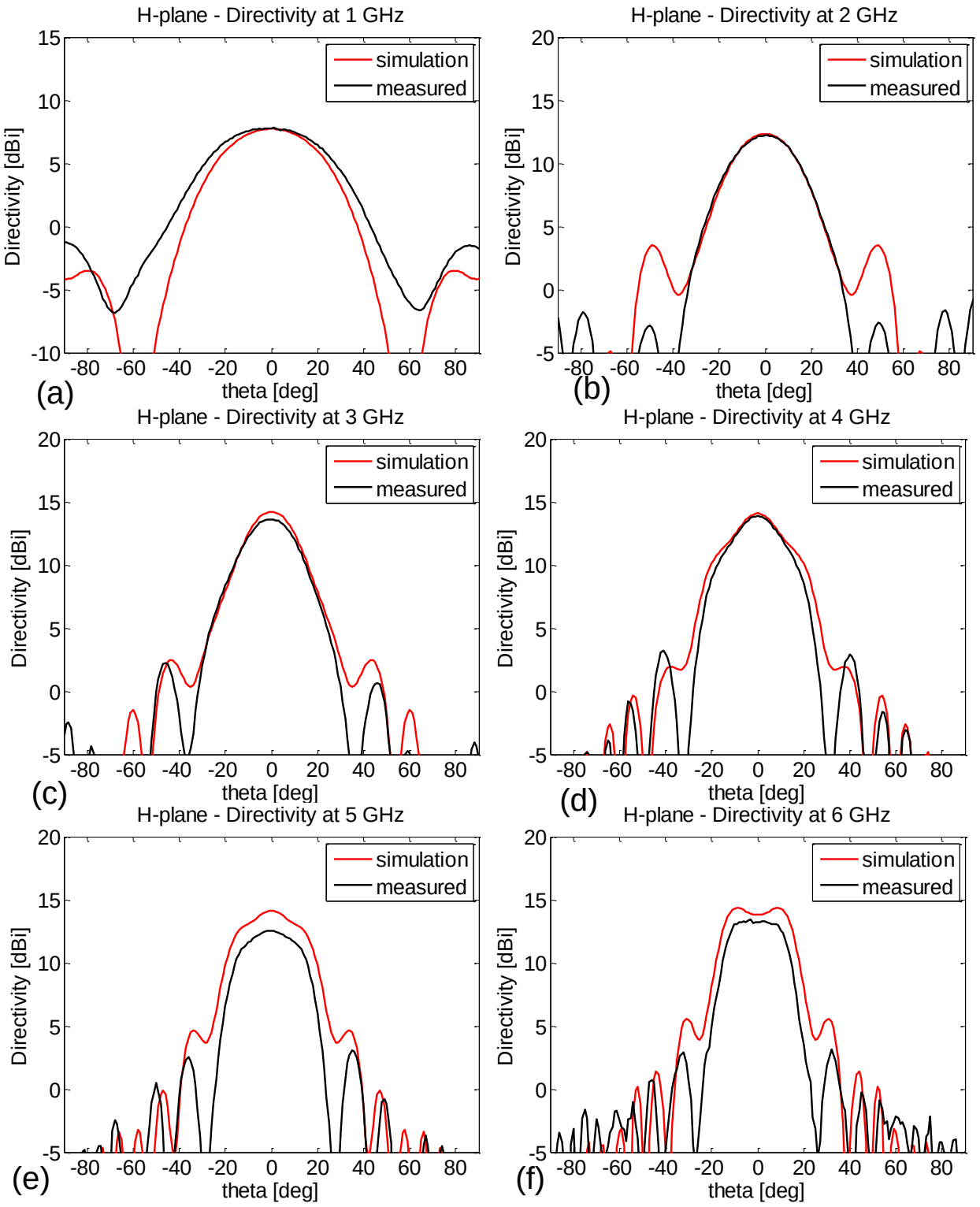

Figure 6.38: Comparison of measured H-plane directivity and simulated H-plane directivity: (a) 1 [GHz] (b) 2 [GHz] (c) 3 [GHz] (d) 4 [GHz] (e) 5 [GHz] (f) 6 [GHz]

Figure 6.40 shows the E- vs H-plane measurement results at each sample frequency. The equivalent simulation results are repeated in Figures 6.41 - 6.43 for easy comparison. Due to the construction flaws and poor structural support discussed in previous paragraphs, the purpose of

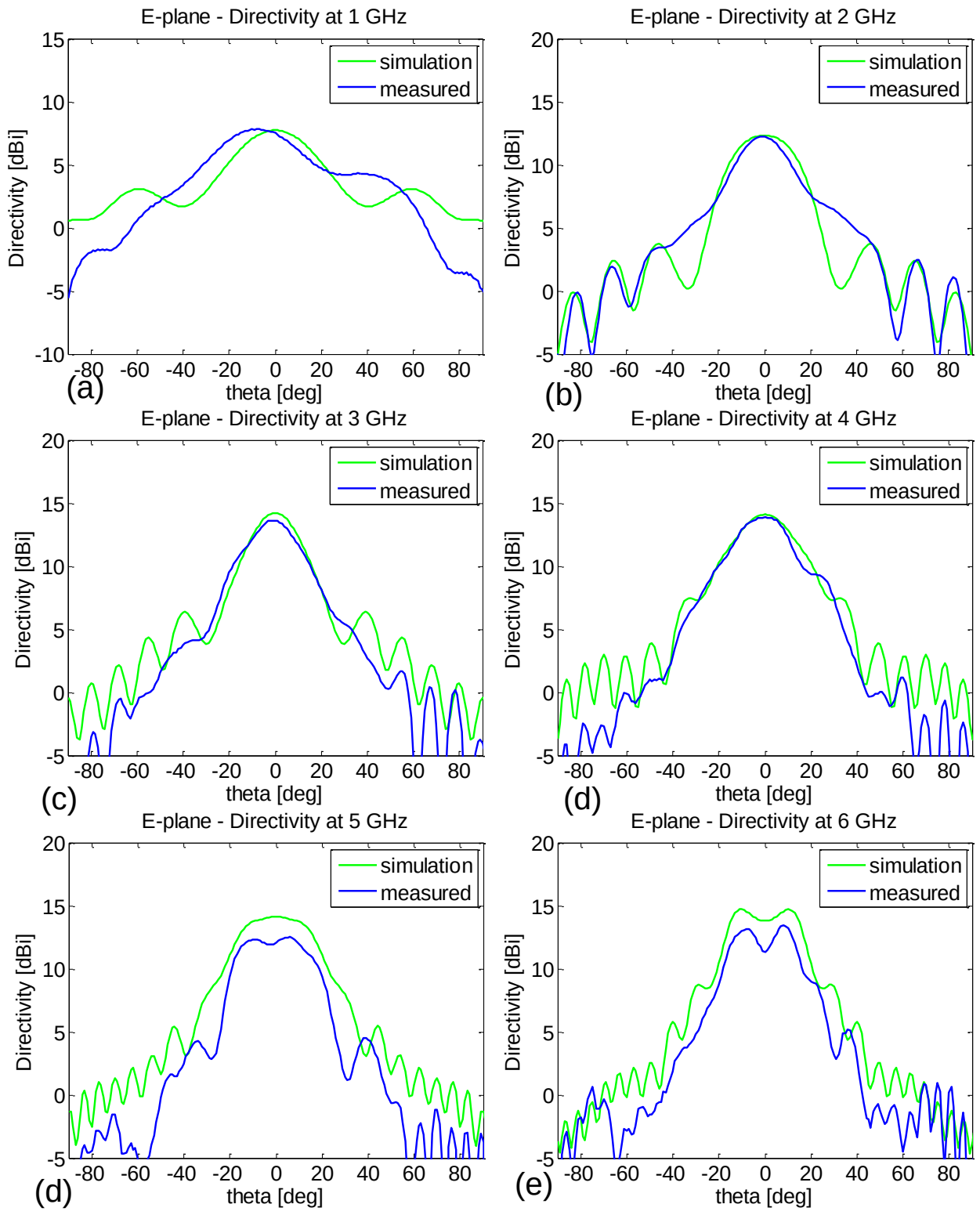

Figure 6.39: Comparison of measured E-plane directivity and simulated E-plane directivity: (a) 1 [GHz] (b) 2 [GHz] (c) 3 [GHz] (d) 4 [GHz] (e) 5 [GHz] (f) 6 [GHz]

illustrating an improvement in the roundness of the radiation pattern over a wide bandwidth is negatively influenced. However, by noting the reasons for the measurement deviations, the results do illustrate that if it were not for the structural or symmetry problems, the measurement and

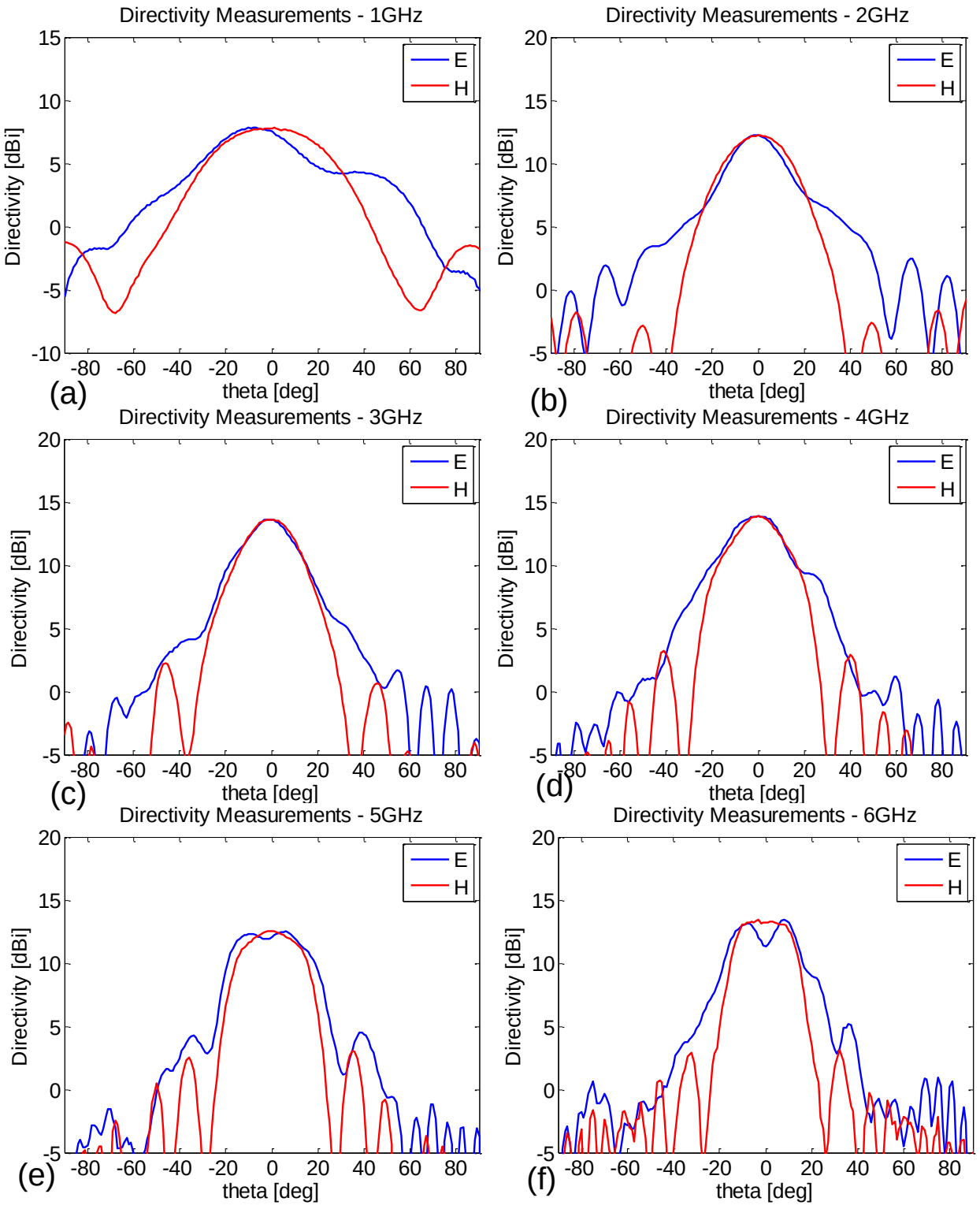

Figure 6.40: Measured H-plane vs E-plane directivity: (a) 1 [GHz] (b) 2 [GHz] (c) 3 [GHz] (d) 4 [GHz] (e) 5 [GHz] (f) 6 [GHz]

simulation results would correspond very well. Figure 6.40 (b) and (c) are the measurement results that best illustrate the performance of the modified horn with regard to yielding a round radiation patten over a wide bandwidth.

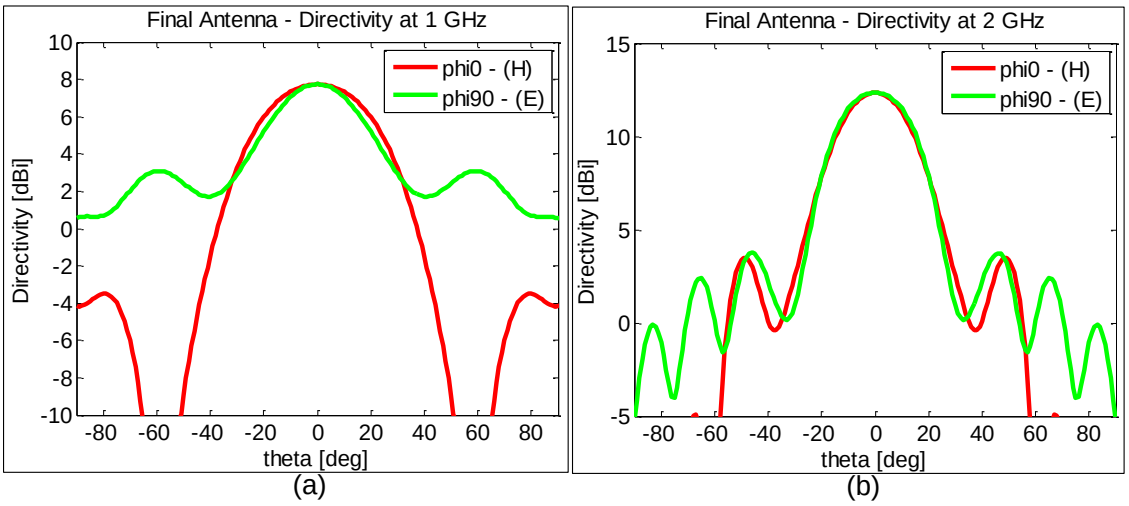

Figure 6.41: E- and H-plane directivity simulation results: (a) 1 [GHz] (b) 2 [GHz]

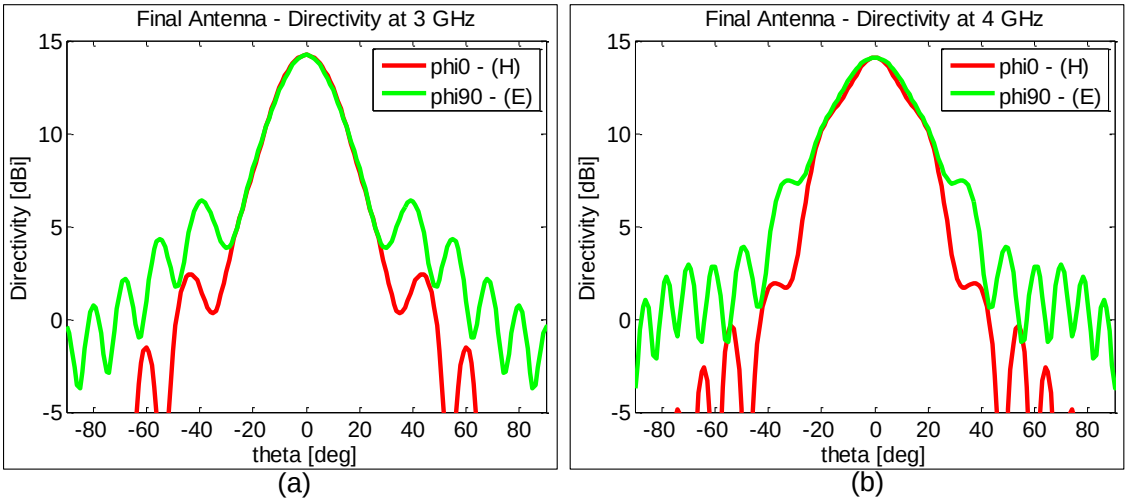

Figure 6.42: E- and H-plane directivity of the final antenna with wideband feed: (a) 3 [GHz] (b) 4 [GHz]

6.6 Conclusion

This section concludes the investigation into achieving a round radiation pattern over a wide bandwidth with a modified exponential TEM horn. In Section 6.2.1 it is found that a TEM horn with a convex parabolic arc offers more potential to achieve a round radiation pattern than a standard exponential TEM horn or an exponential TEM horn with a concave parabolic arc.

In Section 6.2.2, the influence of the arc depth on the roundness of the radiation pattern is investigated for an exponential TEM horn with a convex parabolic arc. The results compared to those of a standard exponential TEM horn and it is shown that the arc depth has an influence on the frequencies at which an improvement in the roundness of the radiation pattern is achieved. A smaller arc depth offers an improvement in the roundness of the radiation pattern in terms of EL's and one-sided angular range at lower frequency end (1-3 [GHz]), whereas the larger arcs

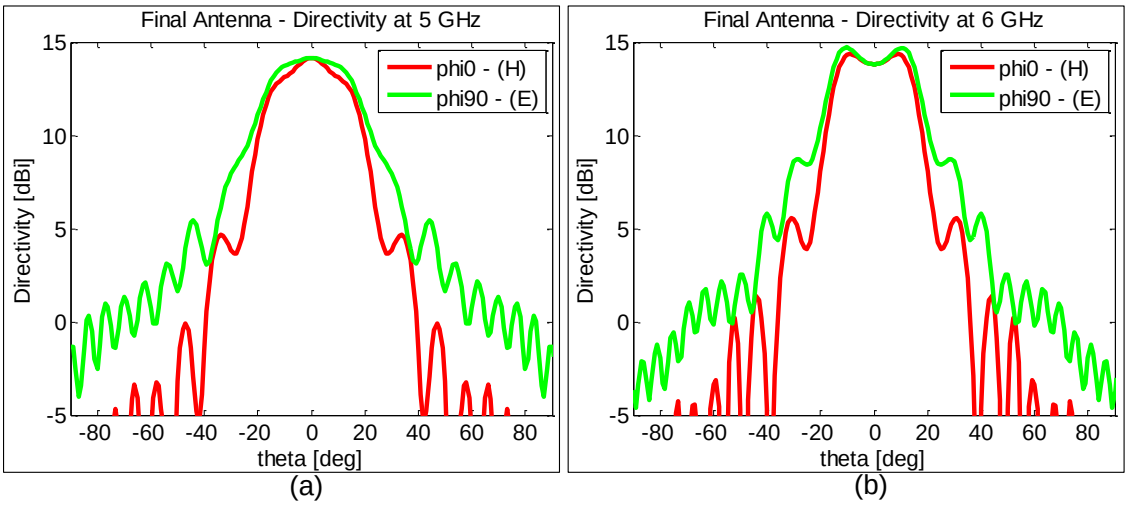

Figure 6.43: E- and H-plane directivity of the final antenna with wideband feed: (a) 5 [GHz] (b) 6 [GHz]

start to offer an improvement at both the lower and upper frequencies. At some point, the arc depth becomes too large and an improvement at the lower frequencies is lost. It is found that for the exponential horn with a convex parabolic arc, a depth of $d_{arc} = L/6$ yielded the best overall improvement in the roundness of the radiation pattern over the bandwidth.

The investigation is repeated for an exponential TEM horn with a convex triangular arc with similar results. The best overall improvement in the roundness of the radiation pattern is observed when the arc depth of the horn with the convex triangular arc is $d_{arc} = L/6$ and the results are found to be even better than with the equivalent parabolic arc. The EL's achieved with the modified horns offer a significant improvement on those of the standard exponential horn, as discussed in Section 6.2.2 and 6.2.3.

It is decided to construct the exponential TEM horn with the $L/6$ triangular arc, and a wideband feed is designed for the antenna so that the final system has a bandwidth of 1-6 [GHz]. The final simulation results are presented in Section 6.3.1 and summarised in Table 6.14. The results show that a round radiation pattern has been successfully achieved according to the specifications in Chapter 1 at frequencies of 1, 2, 3 and 4 [GHz]. The most notable results are the achievement of an EL of -10.4 [dB] at 3 [GHz] and that the EL's are all well below the -3 [dB] HPBW from 1-4 [GHz], with a maximum EL of -5.6 [dB] at 1 [GHz].

The antenna and wideband feed system is constructed and measured as discussed in Sections 6.4 and 6.5, respectively. The least expensive method was chosen for construction and resulted in loss of symmetry during measurements. In addition, a piece of fr_4 was inserted at the feed pin to ensure a plate separation of 1.5 [mm]. As shown in Figure 6.36, s_{11} with fr_4 is very poor. Therefore, the piece of fr_4 is removed and s_{11} measured again. Although a better result is achieved, the top parallel plate is not soldered to the ridges as required and bent downward. This influences the port impedance and symmetry. Therefore, the measurement results for s_{11} are far worse than

the simulation results. The measured E-plane pattern is asymmetrical since the top antenna plate bent away from the foam between the two antenna plates when the structure was placed on its side for the measurements. This defeats the purpose of accurately comparing the correlation between the E- and H-plane patterns. Therefore, it is recommended that the structure and similar structures should rather be constructed from a solid block of metal. Apart from the symmetry, the radiation patterns do compare well to the simulation results with the patterns at 2 and 3 [GHz] in Figure 6.40 illustrating that the modification of a convex triangular arc will improve the roundness of the radiation pattern. From the reputation of the simulation software to produce accurate results, it is expected that the measurement results would have compared extremely well to simulation results. From this it is concluded that modifying an exponential TEM horn to have an $L/6$ convex triangular arc successfully yields a round radiation pattern over a wide bandwidth.

Chapter 7

Conclusion and Recommendations

The purpose of this thesis was to investigate the potential of TEM horn antennas for use as SKA feed antennas. Emphasis is placed on the criteria of a round radiation pattern over a wide bandwidth, as discussed in Chapter 1. In Chapter 3 it is shown that pre-existing TEM horn designs, such as the linear tapered TEM horn and the elliptical/Hecken TEM horn, do not yield a round radiation pattern over a wide bandwidth. Therefore, an alternative design is required.

The Method of Moments (MoM) is a very efficient numerical technique for the analysis of TEM horns. An in-house MoM solver is successfully developed in MATLAB, to calculate the current density on the surfaces of conductors as well as their farfield radiation patterns. The basic concept of the MoM is illustrated for the case of thin wires in Chapter 4. The principles are extended in Chapter 5 to develop an in-house MoM solver using the triangular patch MoM. A mesher is also developed to triangulate the surfaces of conductors as required for the MoM. Although the results of the in-house solver compare well to those of the simulation software FEKO, there is an order of magnitude difference in the execution time of the two solvers. Therefore, FEKO or CST is used throughout the rest of the thesis. It is suggested that the code should be developed using C or C++, instead of the vector language in MATLAB. Although the vector and matrix operations available in MATLAB would then have to be self-implemented, the execution time of the in-house solver would be significantly reduced.

In Chapter 6, a modification to an exponential TEM horn is proposed, which successfully yields a round radiation pattern over a wide bandwidth. An exponential TEM horn with a convex parabolic arc, as well as an exponential TEM horn with a convex triangular arc are analysed for various arc depths and their radiation patterns compared to those of a standard exponential TEM horn. As discussed in Chapter 6, the arc depth is found to influence the frequencies at which an improvement in the roundness of the radiation pattern is observed. The final antenna is an exponential TEM horn with a **convex** triangular arc with $d_{arc} = L/6$. A wideband feed, which makes use of a 50 [Ω] SMA connector, is designed for the antenna as discussed in Section 6.3.

The final antenna and its wideband feed are constructed and measured at Stellenbosch Univer-

sity's anechoic chamber. The method of construction does not provide sufficient structural support to ensure the symmetry of the design. Therefore, the measured radiation patterns deviate slightly from the simulated results as discussed in Section 6.5. The results do, however, illustrate the potential of the design to achieve a round radiation pattern over a wide bandwidth. The measurement results indicate that if the antenna is better constructed, the measurements would correspond very well to the simulation results. From the measurement results and the reputation of the simulation software to produce accurate results, it is concluded that the proposed modification is successful in yielding a round radiation pattern over a wide bandwidth. Although more expensive, it is recommended that the antenna and its wideband feed should be constructed from a solid block of aluminium. This is a very strong method of construction which would ensure the symmetry of the antenna.

Overall, it is shown that the plates of an exponential TEM horn can be modified to end in a convex type of arc (with optimised depth) to improve the roundness of the radiation pattern when compared to a standard exponential TEM horn. Various analytical arc types can be investigated to determine if further improvement in the roundness of the radiation pattern can be achieved. It is proposed that the potential of achieving dual-polarisation with the modified horn.

References

[1] South Africa Website, S.: Square Kilometre Array (SKA) South Africa. 2010. Available at: www.ska.ac.za

[2] Schoeman, K.: Waveguide Antenna Feed for the Square Kilometer Array, 2008. Final Year Project.

[3] Malherbe, J.A.G.: TEM Horn Antenna with an Elliptical Profile. *Microwave and Optical Technology Letters*, vol. 49, pp. 1548–1551, 2006.

[4] Rao, S.M., Wilton, D.R. and Glisson, A.W.: Electromagnetic Scattering by Surfaces of Arbitrary Shape. *IEEE Transactions on Antennas and Propagation*, vol. AP-30, pp. 409–418, May 1982.

[5] Savage, J.S. and Peterson, A.F.: Quadature Rules for Numerical Integration over Triangles and Teterahedra. *IEEE Transactions on Antennas and Propagation*, vol. 38, no. 3, pp. 100–102, 1996.

[6] Dunavant, D.A.: High Degree Efficient Symmetrical Gaussian Quadrature Rules for the Triangle. *International Journal for Numerical Methods in Engineering*, vol. 21, pp. 1129–1148, 1985.

[7] Balanis, C.A.: *Antenna Theory Analysis and Design*. John Wiley & Sons, 2005.

[8] Mallahzadeh, A. and Karshenas, F.: Modified TEM Horn Antenna for Broadband Applications. *Progress In Electromagnetic Research*, vol. PIER 90, pp. 105–119, 2009.

[9] Lee, R.T. and Smith, G.: A Design Study for the Basic TEM Horn Antenna. *IEEE Antennas and Propagation Magazine*, vol. 46, pp. 86–92, 2004.

[10] Malherbe, J.A.G.: Extreme Performance TEM Horn. *Microwave and Optical Technology Letters*, vol. 50, pp. 2121–2125, 2007.

[11] Pozar, D.M.: *Microwave Engineering*. John Wiley & Sons, Inc, 2005.

[12] Davidson, D.B.: *Computational Electromagnetics for RF and Microwave Engineering*. Cambridge University Press, 2005.

[13] Gibson, W.C.: *The Method of Moments in Electromagnetics*. Chapman & Hall/CRC, 2008.

[14] Schoeman, M.: *Interpolation-Based Modelling of Microwave Ring Resonators*. Ph.D. thesis, University of Stellenbosch, 2006.

[15] Guru, B. and Hiziroglu, H.: *Electromagnetic Field Theory Fundamentals*. Cambridge University Press, 2004.

[16] Pozar, D.M.: *Microwave and RF Design of Wireless Systems*. John Wiley & Sons, 2001.